STRUCTURAL STUDIES OF BIOPOLYMERS USING COMPUTER SIMULATIONS, OPTICAL AND MAGNETIC SPECTROSCOPY

by

SUBHASISH CHATTERJEE

A dissertation submitted to the Graduate Faculty in Chemistry in partial fulfillment of the requirements for the degree of Doctor of Philosophy, The City University of New York

2009

This manuscript has been read and accepted for the
Graduate Faculty in Chemistry in satisfaction of the
dissertation requirement for the degree of Doctor of Philosophy.

8/6/2009	Ruth E. Stark
Date	Chair of Examining Committee
8/12/2009	Mahesh Lakshman
Date	Executive Officer

Harry D. Gafney

Vinod M. Menon

Bonnie L. Gersten

Supervision Committee

THE CITY UNIVERSITY OF NEW YORK

Abstract

STRUCTURAL STUDIES OF BIOPOLYMERS USING COMPUTER SIMULATIONS, OPTICAL AND MAGNETIC SPECTROSCOPY

by

Subhasish Chatterjee

Adviser: Professor Ruth E. Stark

Biopolymers are essential components of numerous natural and synthetic macromolecular assemblies. In the present study, the structural properties of biopolymers ranging from fungal melanins to synthetic nucleic acids were investigated using spectroscopic methods and theoretical modeling. (1) Computational modeling and molecular dynamics simulations were used to study the structural properties of a short single-stranded (ss) DNA. The dependence of the conformational stability and flexibility of the ssDNA on the thermodynamic conditions of the system was demonstrated. (2) Time-resolved fluorescence spectroscopy involving an organic donor-quencher pair was utilized to study the conformational properties of Y-shaped DNA. Results highlighted the different distances between the arms of the Y-DNA and indicated the overall structural stability of the Y-DNA system. Time-resolved fluorescence techniques were applied to investigate the distance dependence of the non-radiative energy transfer process between an organic donor (fluorescein) and a gold nanoparticle quencher connected by double stranded (ds) DNA. (3) Synthesis of phospholipid-conjugated gold nanoparticles and their self-assembly onto an aqueous subphase were tested. The resulting lipid-capped nanoparticles were characterized by optical methods such as

UV-Vis absorption spectroscopy and dynamic light scattering. The effects of bio-functionalization on the size of biotin-capped gold nanoparticles were investigated using optical techniques. (4) Solid-state nuclear magnetic resonance (NMR) spectroscopy was utilized to elucidate the structural characteristics of fungal melanins. Various spinning speeds, temperatures, magnetic field strengths, and isotopic labels were utilized with 1D and 2D ^{13}C MAS NMR, revealing distinctive structural fingerprints of the fungal melanins generated biosynthetically with L-dopa, methyldopa, epinephrine, and norepinephrine. These pigments exhibited differences in their aromatic and aliphatic structures and probable biosynthetic pathways, and it was possible to delineate proximities between particular melanin and membrane-related molecular groups.

Acknowledgements

I remain ever grateful to my mentor, Professor Ruth Stark, for her kind support, encouragement, and guidance throughout my doctoral study. I would like to express my heartfelt gratitude to my thesis committee advisers, Professors Bonnie Gersten, Vinod Menon and Harry Gafney, for their munificent advice and the opportunities to work with them.

I gratefully acknowledge the cordial help of Dr. Baohe Chang, Dr. Nikesh Valappil, Dr. Hsin Wang, Dr. Boris Itin, Ms. Miriam Ginzberg, and Ms. Markrete Krikorian, whom I worked with at various stages of my doctoral study. I remain very thankful to my all colleagues and friends at Queens College and City College for their help and assistance.

I would like to thank Prof. Arturo Casadevall's group for the collaboration on the structural investigation of fungal melanins and Prof. Dan Luo's group for the collaboration on the time-resolved spectroscopic study on nucleic acid systems.

I gratefully acknowledge the Irving Hochberg Dissertation Fellowship in the Sciences (2007-2008) from the Graduate Center of City University of New York.

Table of Contents

Tables

List of Figures

1.1. An Overview of Melanin Structure

Melanin, a ubiquitous natural pigment, is associated with various biological functions such as microbial virulence, drug resistance, energy transduction, radical scavenging, and protection against sunlight [1-6]. In various opportunistic pathogenic fungi, including *Cryptococcus neoformans*, melanin formation is connected with virulence, thus posing problems for immunocompromised individuals [7]. Because melanins are associated with enhanced virulence [7, 8] and also reduced fungal cell susceptibility to azole-type drugs, they are a natural target for drug discovery [3, 7, 11]. Melanin is also thought to be responsible for the resistance of human melanoma cells to therapeutic radiation and chemotherapy [11]. The similarities between fungal (*Cryptococcal*) and mammalian melanin have been utilized to develop monoclonal antibodies for the treatment of melanoma [12].

Although melanins are present in a wide range of biological kingdoms, the structures of these amorphous pigments are poorly understood because of their heterogeneous, insoluble, hydrophobic and charged polymeric physiochemical characteristics [3-6]. Based on chemical degradation studies, these pigments have been deduced to be phenol or indole-based polymers [5]. However, investigating the structure of the intact pigment remains an extraordinarily challenging task [5, 6, 9]. Melanins are broadly categorized into two groups depending on their chemical composition [3]: eumelanins are dark brown to black pigments containing 6-7% nitrogen and 0-1% sulfur; whereas pheomelanins are reddish-brown pigments with 8-11% nitrogen and 9-12% sulfur [3]. The pigments in the human skin, in melanomas, in melanized neurons *(Substantia nigra*) and in melanized *Cryptococcus neoformans* are all eumelanins [6, 10, 11]. In contrast, red hair pigment is

a pheomelanin. Molecular-level structural investigations of melanin with solution-state spectroscopic and optical techniques are precluded by the insolubility of brown or black melanins [5, 6]. Similarly, the amorphous physical characteristics of melanin do not allow the use of current crystallographic methods for elucidating their molecular structures. Solid-state NMR offers an exclusive means for atomic level structural investigation in light of melanin's amorphous and insoluble physical properties [5, 6, 10].

A common functional feature of natural melanins is the entrapment of free radicals, which yields paramagnetic characteristics of the biopolymer, evidenced by various electron paramagnetic resonance (EPR) experiments [3, 13, 14, 15]. It has been proposed that several redox forms of the indolic monomers are responsible for the paramagnetic characteristics of melanin [16, 17]. Although several EPR reports attributed the paramagnetic activity of melanin to the presence of free radicals generated in the pigment, no structural correlation between the redox forms and overall molecular architecture of the pigment has been established. Neither the mechanism of formation of the redox intermediates nor their role in eumelanin's paramagnetic activity is clearly understood. Moreover, synthetic melanin systems may not be a valid model, since they might not duplicate the intrinsic structural details of the natural biopolymer. Although several theoretical and experimental studies have proposed that eumelanin is composed of indolic monomers such as 5,6 dihydroxyindole (DHI) and 5,6 dihydroxyindole-2-carboxylic acid (DHICA) [16,17] (**Figure 1**), it is not clearly understood how these monomeric units are conjugated together to form a polymer.

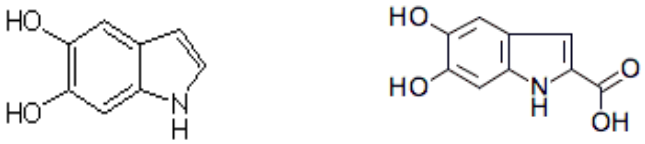

DHI DHICA

Figure 1: Possible intermediates for melanin synthesis.

The covalent structures related to the possible binding of melanin with neighboring biopolymers such as proteins, lipids, and carbohydrates also remain unsettled [3,5, 6].

Natural melanins are capable of binding and storing various types of metal ions, and their affinity regulates the role of melanin as a reservoir for metal ions and as an antioxidant controlling oxidative stress [19]. The presence of metals in neuromelanin has drawn considerable attention due to their possible connections with the selective degradation of pigmented neurons in the *Substantia nigra* (SN) of the brains of patients suffering from Parkinson's disease [19]. The ability to bind metal ions was demonstrated by several structural and functional analyses of melanin using chemical degradation and numerous spectroscopic techniques such as IR, Raman, XPS, and ssNMR [19]. Furthermore, the chemical nature of the functional groups present in indolic monomers controls the pH-dependent metal binding capacity of the pigment. Commonly, the binding affinity of melanin to metal ions follows this incremental order, alkali metal < alkaline earth metal < Zn (II) <Cu (II), Fe (II), and Mn (II) [17]. The chemical properties of the functional groups affect the metal binding affinity of the pigment by controlling the proportion of binding sites in the polymer and their local environment [17]. Since metal ion binding centers of the pigment are expected to be electron-rich sites of the polymer, the

paramagnetic characteristics of melanin can be altered due to binding to metal ions. Hence, an investigation of the paramagnetic properties of melanin can provide details on the structural integration of molecular sites that play a crucial role in its metal ion binding capacity.

Various structural models have suggested that synthetic eumelanin is an extended heteropolymer with extensive cross-linking [20, 22]. Conversely, recent structural studies have proposed that eumelanin is mainly a stack of oligomers consisting of four to seven monomers [20, 21]. In general, eumelanins show strong broadband absorption and relatively weak emissions; the positions of excitation peaks and emission wavelengths are largely dependent on the source of the eumelanin. The appearance of a specific excitation peak at 365 nm, exhibiting its position irrespective of emission wavelengths, is attributed to singly linked monomers in the stacked polymeric structure [20]. Some structural investigations of synthetic melanin using X-ray diffraction [23, 24] and atomic force microscopy support the stacked polymer model [20, 21]. However, no structural framework of natural eumelanin has been firmly established.

1.2. Deducing the Molecular Structure of Fungal Melanins

The pathogenic fungus *Cryptococcus neoformans* (CN) produces melanin pigments only in the presence of exogenous substrates and thereby offers unique opportunities for probing melanin structure at the molecular level [3]. *C. neoformans* exhibits differences in the melanin synthesis process from other melanotic pathogenic fungi such as *Wangiella dermatitidis* or *Aspergillus spp.* that synthesize melanin-like pigments from endogenous substrates (25, 26). Laccases (Lac), which are copper-containing oxidase enzymes, catalyze melanin synthesis in *C. neoformans* [27]. There are two laccases in *C. neoformans*, encoded by genes LAC1 and LAC2 [27]. Although these enzymes are highly homologous, they show differences in activity, transcriptional regulation and cellular localization, with Lac1 and Lac2 being found in the cell wall and cytoplasm, respectively [3]. The regulation of melanization in *C. neoformans* is a complex process with numerous genes involved in both pigment production and laccase expression [3,13]. Incubating *C. neoformans* with phenolic substrates leads to melanization with laccase activity that can oxidize both *p*- and *o*-diphenols (**Figure 2**), giving different products [28-30]. The oxidation of *o*-diphenols (phenol rings with hydroxyl groups in the 2,3- or 3,4-positions) results in the deposition of insoluble pigment in the cell wall. Conversely, the oxidation of *p*-diphenols (phenol rings with hydroxyl groups in the 1,4- and 2,5-positions) produces soluble pigment that diffuses into the medium [28-30]. The insoluble cell-wall associated pigment contains a stable free radical and shows EPR activity [3,13].

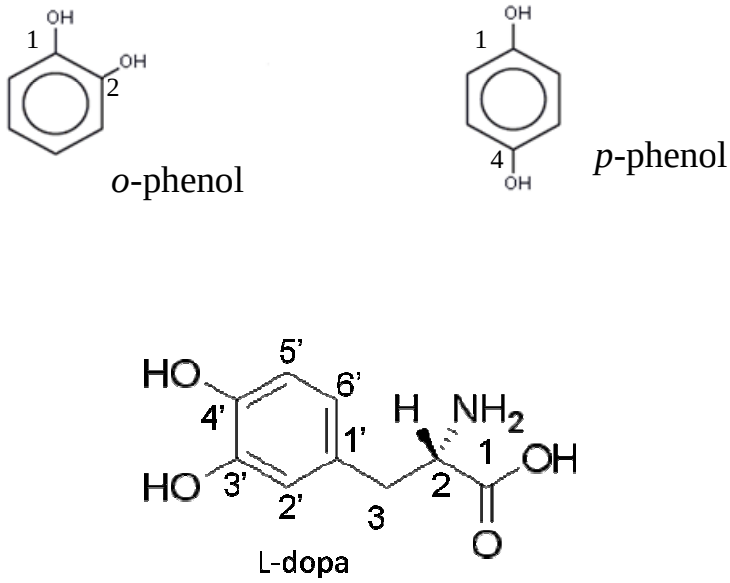

Figure 2: Phenolic substrates for *C. neoformans* melanization.

Melanin pigment deposited in the cell wall of *C. neoformans* is isolated by stepwise treatment of the melanized cells with fungal cell wall digesting enzymes, denaturants, proteinases, chloroform, and boiling hydrochloric acid [3, 8, 13]. The recovered materials (melanin "ghosts") are suitable for biophysical experimentation [3, 8]. Various catecholamines such as L-dopa are reported to be obligatory exogenous precursors of melanin, which are then known as dopa-melanins. Experimental studies have highlighted the compositional differences between synthetic dopa-melanins (prepared enzymatically or chemically from L-dopa) and natural melanins [3, 5, 6]. These striking observations prompted researchers to investigate the structure of the natural pigments using various biophysical approaches. The dependence of *C. neoformans* melanization on exogenous substrates provides a natural platform to produce biosynthetically labeled melanins, which are suitable for structural investigation by solid-state NMR techniques. The

application of high-resolution solid-state NMR techniques and various isotopic labeling schemes offer the potential to surmount melanin's investigative challenges and to develop a comprehensive molecular picture of this complex pigment [5, 6].

Previous solid-state NMR studies by the Stark group have shown that, aside from the aromatic groups, a major part of the molecular composition of *C. neoformans* dopa-melanin ghosts is aliphatic, including uncyclized methylene groups having a high degree of flexibility [5, 6]. Many structural features such as the C_2-C_3 bond in L-dopa are retained when this precursor is incorporated into the biosynthesized pigment [5, 6]. Structural investigation of melanin swelled in solvents showed the presence of various functional groups, including alkanes, alkenes, alcohols, ketones and carboxylic acid esters. The metabolic fate of glucose present in the cell growth media was found to include both polysaccharides and aliphatic chains of the fungal melanin ghosts [6]. Although a preliminary picture of dopa melanin's molecular architecture has been obtained from the previous studies, a comprehensive understanding of the pigment's molecular framework and synthesis pathway is still undetermined and demands an extensive investigation.

Melanins produced with a series of catecholamine substrates such as L-dopa, methyl-dopa, (-)-epinephrine, and (-)-norepinephrine showed considerable differences in terms of the yield, color of soluble and insoluble products, surface charge, stable free radical content, antibody binding ability, and other physical characteristics [3]. In the current study, solid-state NMR techniques were used to investigate the molecular structures of the pigments produced with these different substrates (methyldopa, (-)-epinephrine,

norepinephrine, serotonin), comparing the results with structural fingerprints of the standard L-dopa melanin. These structural investigations of various catecholamine-derived melanin ghosts helped to deduce differences in the aromatic ring structures of the pigments and to analyze the interaction with polysaccharide cell walls and/or membrane constituents. As exogenous precursors (e.g. L-dopa) are required to generate fungal melanins, the investigation of the metabolic transformations of the precursor was pursued by growing the fungal cells in the presence of a group of selectively ^{13}C-enriched L-dopa precursors and sugar sources including ^{13}C-^{13}C pairs (2,3-$^{13}C_2$-L-dopa), ring-$^{13}C_6$-L-dopa, and U-$^{13}C_6$-glucose. The use of ^{13}C labeled L-dopa in the synthesis of fungal melanin has been used to demonstrate the spatial connectivities of key molecular groups in the resulting pigments.

1.3. Biosynthesis of Fungal Melanins

The fungal cells were grown in the presence of an obligatory precursor (1 mM) in chemically defined media (29.4 mM KH_2PO_4, 10 mM $MgSO_4$, 13 mM glycine, 15 mM D-glucose and 3 µM thiamine) for two weeks at 30 ^oC in a rotatory shaker at 150 rpm. The cell pellets were obtained by centrifugation at 2000 rpm. After washing the isolated fungal cells once with sorbitol (1.0 M)/sodium citrate (0.1 M, pH=5.5) solutions, they were resuspended in a phosphate buffered saline (PBS) buffer solution and incubated with Novozyme 234 (10mg/mL) for one day at 30 ^oC to remove cell walls. Afterwards, the resulting solution was centrifuged at 2000 rpm for ten minutes and the supernatant was discarded. The solid product (melanized protoplasts) was washed with 20 ml PBS until the supernatant was relatively clear. A 20 ml aliquot of guanidine thiocyanate (4.0 M) was added and the suspension was incubated for 30 minutes with occasional vortexing at room temperature. The suspension was centrifuged at 2000 rpm for ten mins, and the collected cell debris was washed with ~ 20 ml PBS buffer (2-3 times). Afterwards, the cell debris was subjected to lipid extraction following the Folch method [31], maintaining the proportions of chloroform, methanol and saline solution in the final mixture as 8:4:3. The final product was suspended in 20 ml of 6 M HCl and boiled for one hour to hydrolyze cellular contaminants associated with melanin. The black particles of interest that survived after HCl treatment were dialyzed against distilled water for ten days. The resulting melanin particles, which maintained characteristic elemental compositions (C:N:O = 29:2:6) [6], were lyophilized for further biophysical analyses. These procedures were carried out in the Casadevall Lab (Albert Einstein College of Medicine); S. Chatterjee assisted with the growth and extraction steps.

In selected experiments, 2-3-$^{13}C_2$ (97%), 4-^{18}OH (95%)-L-dopa or ring- ^{13}C L-dopa was used as a melanin precursor. Additionally, U-^{13}C-glucose was used as a sugar source in other experiments. To compare the structural frameworks of various fungal melanins, the cells were grown in the presence of a range of catecholamine precursors, namely methyldopa, epinephrine, and norepinephrine, and serotonin. The resulting pigments were obtained following the abovementioned treatments. In addition, the pigments were biosynthesized with an equimolar mixture of L-dopa and epinephrine (1:1 mol/mol) to investigate competition between the incorporation of the two precursors.

1.4. Introduction to Solid-State Nuclear Magnetic Resonance (NMR) Experiments

The simplest picture of a NMR experiment can be considered as a measurement of the frequency of the signals generated by nuclei having nonzero nuclear spin quantum number, after the molecular system is irradiated with a radiofrequency (RF) pulse in the presence of a static magnetic field (B_o) [32,33]. The NMR active nuclei exhibit resonance frequencies, which are basically equivalent to the energy differences between the excited state and ground state of the nuclei under the influence of the static magnetic field [32]. The signals produced by the nuclei are reported after Fourier transformation involving the conversion of the free induction decay (FID, time domain) to its associated frequency domain [32]. Thus, nuclear magnetic resonance investigates the interaction of microscopic nuclear magnetic moments (such as ^{1}H, ^{13}C, or ^{15}N spins) with a static magnetic field (B_0) and an external radiofrequency field. The value of a resonance frequency typically depends on the type of nucleus and the local molecular environment in which the nucleus is situated. A nucleus is surrounded by electrons, which can be considered as moving electronic charges with associated magnetic fields and thereby function as a source of magnetic shielding or deshielding for the nucleus [32,33]. Depending on the local distribution of neighboring electrons, the shielding effect causes a variation of the static magnetic field strength at the nucleus, resulting in a change in the resonance frequency of the nuclear spins. This variation in the resonance frequency of a nucleus present in a molecular system is quantified as its chemical shift. Thus, the chemical shift reveals the differences in the local environments of various NMR active nuclei, and consequently helps to identify the types of chemical functional groups present

in the molecular system. For structural studies, NMR signals are usually analyzed in terms of two characteristics, frequency and intensity. Absolute frequencies are measured in Hertz (Hz, cycles per second) or MHz. Reporting of the measured signals is simplified by using the ppm unit, representing transition frequencies of nuclei as a fraction of the absolute precessional frequency that is dependent in turn on the strength of the applied magnetic field B_o. The advantage of using ppm is to report the frequency measurement without referring to the magnetic field strength, and thereby to simplify the comparison of spectra acquired on different spectrometers [32]. The splitting of the NMR signal of a nucleus is caused by spin-spin coupling of neighboring nuclei situated in a magnetically different local environment. The spin-spin coupling takes place via bonding electrons, and the effect of this coupling process can be selectively removed by a technique called "decoupling", which masks the effect of a particular group of nuclei (e.g. ^{1}H) by applying a specific sequence of RF pulses [32,33].

High resolution solid-state (ss) NMR is a powerful technique to probe the structural and dynamical properties of macromolecular systems. Solid-state NMR is capable of providing a detailed picture of conformational dynamics, chemical state, local non-bonded interactions and structural architecture of complex molecular systems that are not amenable to other physical techniques such as X-ray crystallography or solution-state NMR [32-38]. The basic difference in the solid-state NMR methods compared to the solution-based techniques lies in the absence of spectral simplification due to rapid Brownian tumbling, which averages out anisotropic interactions present in the latter molecular systems. On application of the magnetic field, solid-state samples show orientation-dependent dipolar couplings of nuclei in functional groups [32-35]. The

heteronuclear dipolar coupling arises from the interaction between the nuclear magnetic moments of two different types of nuclear spins. Typically, nuclear spins are designated as I for "abundant spins" such as ^{1}H, and S for "dilute" spins such as ^{13}C or ^{15}N nuclei.

The extent to which spin I modifies the effective local magnetic field experienced by spin S under the static magnetic field B_0 is governed by the magnitude of the heteronuclear dipolar coupling, expressed by the Hamiltonian in **Eq. 1** [33,35]

$$H_{IS} = -d\left(3\cos^2\theta - 1\right)I_z S_z \qquad [1]$$

The parameter ***d*** is the dipolar coupling constant.

$$d = \left(\frac{\mu_0}{4\pi}\right)\frac{\hbar\gamma_I\gamma_s}{r_{IS}^3} \qquad [2]$$

Here, r_{IS} represents the internuclear distance between two spins I and S, μ_0 = permeability of free space, γ_I and γ_S = gyromagnetic ratios of spins I and S, respectively, and $\mathbf{I_z}$ and $\mathbf{S_z}$= z components of the nuclear spin angular momentum operators **I** and **S**, respectively [32-35].

The magnitude of the heteronuclear dipolar coupling is directly proportional to the product of the gyromagnetic ratios (γ) of spins. Since the magnetic moment of a nucleus is proportional to γ, nuclei with greater magnetic moment enhance the dipolar coupling interactions. Additionally, the heteronuclear dipolar coupling is inversely proportional to the cube of the internuclear distance between two spins (I and S). Thus, the coupling

interactions rapidly go down with increasing distances between nuclei. Moreover, the heteronuclear dipolar coupling interactions between two spins are dependent on their orientation, which contributes an angle dependent term ($3\cos^2\theta$ -1) in the dipolar Hamiltonian ($\mathbf{H_{IS}}$) [32-35].

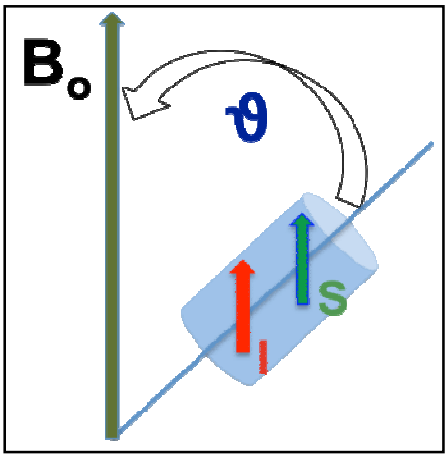

Figure 3: θ is the angle between the external magnetic field (Bo) and the internuclear distance vector.

The dipolar couplings, magnetic through-space interactions between spins, can cause spectral splitting, and the strength of the coupling interactions fundamentally depend on the chemical characteristics of the molecular system.

Chemical shift anisotropy (CSA) plays a critical role in the application of ssNMR techniques [33-34]. The spatial dependence of the nuclear magnetic shielding gives rise to an observed chemical shift, based on molecular orientation with respect to the applied magnetic field. Magic angle spinning (MAS), which is essentially rotating the solid

sample about an axis of approximately 54.74^{o} with respect to the applied magnetic field, leads to averaging of most anisotropic interactions of nuclei with nuclear spin quantum number of ½ [33-35]. The rotation at 54.74^{o} makes the angle dependent term $(3\cos^2\theta - 1)$ in **Eq.1** go to zero. Thus, MAS improves the resolution of NMR spectra by narrowing the spectral lines at the isotropic frequency ("chemical shift") of the molecular groups. The application of MAS averages the chemical shift anisotropy as well as the distance-dependent dipolar interactions that serve as a means to measure the spatial proximity between nuclear pairs in various functional groups and molecular fragments. With recent MAS-based techniques, it is possible to restore the dipolar interactions between nuclei, on a time-averaged basis, by applying appropriate rotor-synchronized radio frequency pulse sequences [32-35]. These methods can introduce homonuclear or heteronuclear dipolar interactions during the magic angle spinning, and thereby make it possible to measure internuclear distances in a functional group and to evaluate spatial correlations between neighboring atoms. The spinning frequency required for complete averaging of the dipolar interactions or CSA must be greater than the static linewidth expressed in Hz. Alternatively, the powder pattern can be broken up into a manifold of well-resolved sidebands by MAS at a frequency slower than the specific spinning frequency needed to average all dipolar interactions [32-35].

The cross-polarization (CP) ssNMR technique involves the transfer of magnetization from one set of spins, typically more abundant nuclei with higher gyromagnetic ratio such as ^{1}H, to another low abundant spin, e.g. ^{13}C or ^{15}N, thereby enhancing the signal of the rare spins. The CP technique is an effective a way to obtain NMR spectra of dilute spins such as ^{13}C or ^{15}N in a solid compound, thus avoiding spectral broadening due to

homonuclear dipolar interactions among protons and overcoming long spin-lattice relaxation times of ^{13}C or ^{15}N [32-35]. Consequently, the application of the CP method improves the signal-to-noise ratio of the spectra by yielding more transients in a limited time during signal averaging. The ^{1}H and ^{13}C nuclei in a molecular system maintain a Boltzmann population distribution under the application of a static magnetic field on a time scale determined by T_1 (spin-lattice relaxation) [33]. This population distribution defines the spin temperature and is markedly different for the less abundant ^{13}C spins compared to the ^{1}H due to the difference in their gyromagnetic ratios. At the spin-lock condition of the magnetization, the spins experience a smaller effective magnetic field and will re-equilibrate to a new distribution defined by the "rotating frame" spin temperature, with an effective field of $\omega_1 = \gamma_1 B_1$ [32,33].

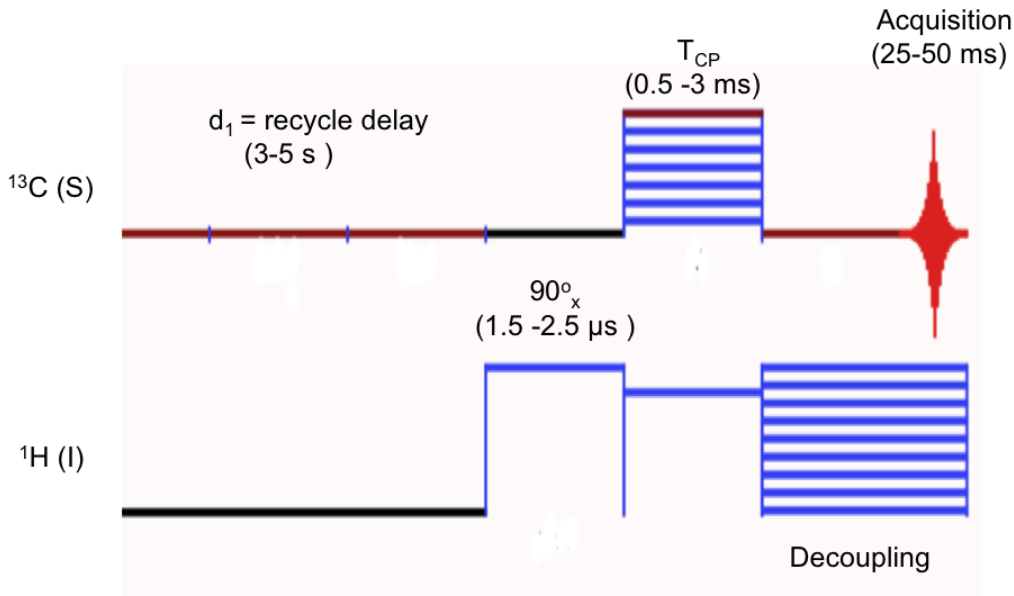

Figure 4: The cross-polarization pulse scheme.

In a CP experiment to detect rare spins (**Figure 4**), a 90^o RF pulse is first applied through the proton channel to achieve the spin-lock condition of ^{1}H magnetization in the rotating frame of reference. Afterwards, the RF field on the ^{13}C is turned on and the amplitude of the magnetic field on ^{13}C is adjusted to fulfill Hartmann-Hahn condition ($\gamma_I B_{1H}=\gamma_s B_{1C}$) [32,33], which ensures that the protons and carbons maintain the same precession frequency in their respective rotating frames, and thus promotes a transfer of magnetization from more abundant protons to carbon-13. Consequently, the Hartmann-Hahn method relies on the simultaneous application of two continuous RF fields, one at the resonance frequency of the ^{1}H spins (I spins), and the other at the resonance frequency of the ^{13}C spins (S spins). As the RF field causes a rotation of the magnetization about the axis of the applied field, both the I and S spins can be rotated independently around a specific axis, maintaining rates estimated by the amplitudes of the two applied RF fields. When the rotation frequencies of the I and S spins are equal, an energy conserving dipolar contact has been established. Alternatively, the creation of dipolar contacts between the two spins can be represented pictorially as equal differences between the excited state and the ground state for the two spins in the doubly rotating frame, so that the polarization is transferred between the I and S spins. The Hartmann-Hahn condition in CP-MAS NMR exhibits a strong mismatch dependence if the spinning frequency is on the order of the dipolar couplings in the sample. Since a molecular system can have different ^{13}C nuclei in varying local environments with significantly different molecular motions, it is imperative to meet the Hartmann-Hahn condition for all ^{13}C nuclei to improve the spectral quality. To fulfill the requirement of exact matching condition, variable-amplitude CP (VACP) and ramped-amplitude CP (RAMP-CP) have

proven to be effective in obtaining flat Hartman-Hahn matching profiles at high spinning speeds [39-40].

To distinguish between protonated and nonprotonated types of carbon, spectral editing techniques can be implemented by modifying a standard CP pulse sequence. The introduction of a time delay (T_d) in the proton decoupling prior to acquisition of the carbon signal, after achieving the spin-lock condition, causes dephasing of singly or doubly protonated carbons (-CH- or $–CH_2$) [41] (**Figure 5**). After this short interruption (10-60 μs), the decoupling proton field is reapplied to remove the heteronuclear dipolar interactions during the acquisition of the carbon free induction decay, which then originates from non-protonated carbons that have not been dephased during the short interruption. Additionally, highly mobile carbons such as long-chain aliphatic groups dephase slowly, retaining their signals in the spectral editing process. By consistently introducing a series of time delays in the proton decoupling period, it is possible to differentiate the protonated carbons by suppressing their signals compared with the non-protonated or highly mobile carbons obtained via the standard CP method [41].

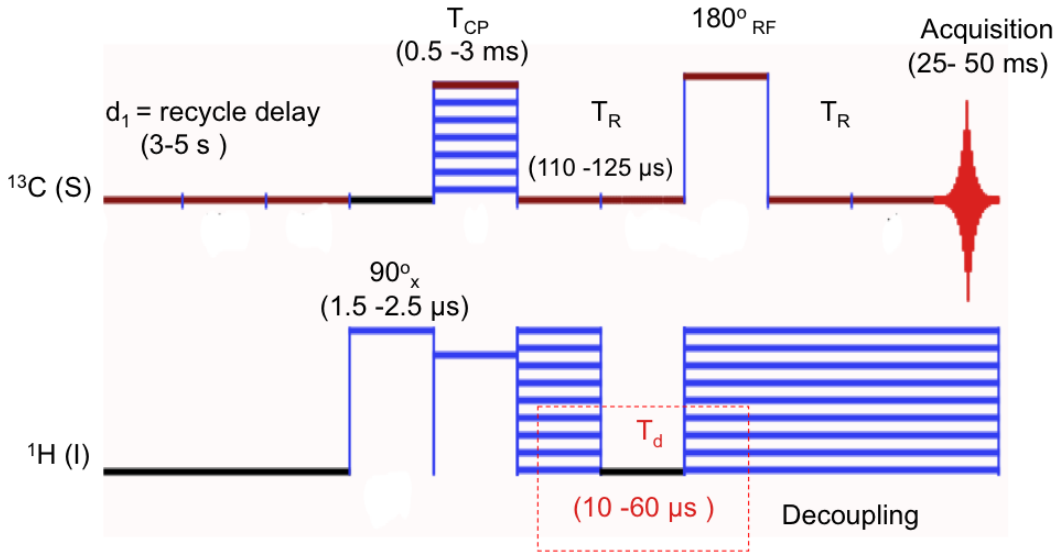

Figure 5: Pulse scheme of cross-polarization (CP) with interrupted decoupling.

The experimental scheme of interrupted decoupling for the suppression of the signals of protonated ^{13}C (S spins) follows constant, linear or tangent-ramped cross-polarization between ^{1}H and ^{13}C with decoupling (**Figure 5**). In addition, a refocusing pulse (180^{o} RF), synchronized with two rotor periods (T_R), is given to avoid a large first order phase correction across the spectrum.

Highly mobile carbon groups in a molecular system can also be identified using the direct polarization MAS technique with the application of varying amounts of proton decoupling power. If the proton decoupling power is high (> 50 kHz) [32,33], both scalar and dipolar heteronuclear interactions can be removed. Conversely, with the use of low decoupling power (~5 kHz), the scalar decoupling can be removed without affecting the dipolar coupling [32,33]. Under these latter conditions, the signals from the rigid carbons will be broadened, leaving only the mobile carbons in the spectrum.

High-resolution NMR experimental conditions can be achieved by the combined application of MAS, RF decoupling schemes and ultrahigh magnetic fields. Two dimensional (2D) spectroscopy allows the spectral separation of isotopically enriched and selectively labeled molecular systems and the detection of coherence transfer between the individual nuclei. This coherence transfer can be due to isotropic *J* (through-bond) or anisotropic dipolar (through-space) couplings [32-38] (**Figure 7**). *J* couplings mainly elucidate the nature of chemical bonding, and dipolar couplings provide a direct estimation for internuclear distances. A required step towards the determination of molecular structure is the measurement of distances between atoms. In ssNMR, this distance measurement can be performed by directly transferring magnetization through the coherent actions of homonuclear and heteronuclear dipolar couplings, as the strength of dipolar coupling between two nuclei is proportional to the inverse cube of the internuclear distance. However, the effects of homonuclear or heteronuclear dipolar coupling are generally removed under magic angle spinning, as the spinning frequency can be greater than the magnitude of the coupling constant, to achieve higher spectral resolution [33, 34]. Therefore, the specific couplings must be selectively reintroduced by applying RF pulses [33, 34]. The spin diffusion measurements have been implemented to compute spatial correlations of key functional groups in a molecular system. This spin-diffusion experimental methodology has been carried out either with passive spin diffusion (in the absence of proton irradiation), or with proton-driven spin diffusion (PDSD) and the introduction of recoupling of the ^{13}C nuclei through proton irradiation at a rotary resonance condition ($\omega_1 = \omega_r$), known as dipolar assisted rotational resonance (DARR) (**Figure 6**) [33, 34, 42-44].

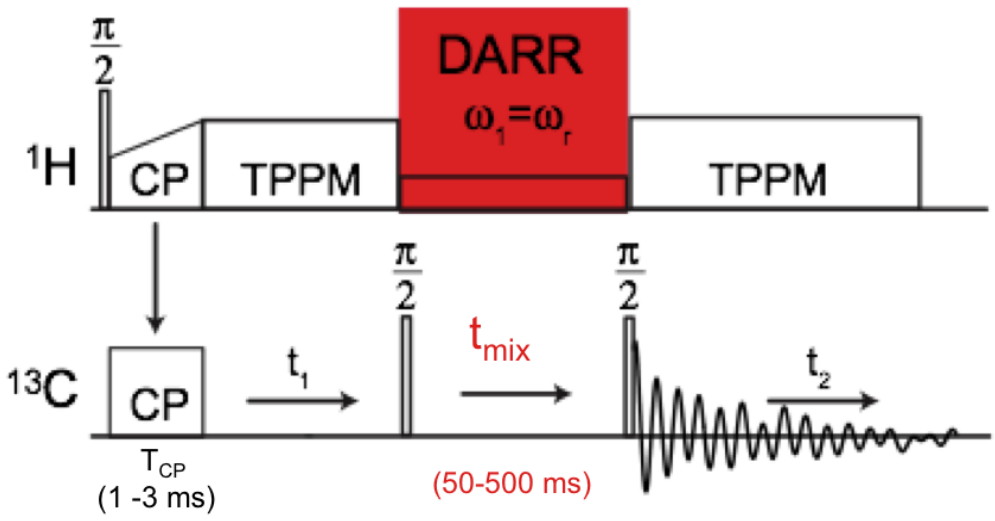

Figure 6: DARR pulse sequence [33].

The DARR experimental scheme starts with a variable amplitude cross-polarization using a ramped pulse on the ^{1}H channel. After an evolution time (t_1), a 90^{o} pulse is applied to the ^{13}C channel to place the magnetization along the z-axis. Afterward, the longitudinal spin mixing (t_{mix}) takes place with a low-power ^{1}H recoupling. During the DARR mixing period, the ^{1}H RF field is adjusted to the rotational resonance condition, $\omega_1 = \omega_r$, where ω_r is the spinning frequency of 10-15 kHz. The TPPM proton decoupling (two pulse phase modulated decoupling) [33] is applied during evolution and acquisition of the ^{13}C signal. The DARR technique overcomes the restriction of dipolar truncation [42-44], thus providing relatively longer distance information. With longer mixing times (~ 500 ms), it is possible to achieve an upper distance limit of ~ 6 Å [45-46]. In the 2D experiment, the traditional NMR spectrum appears on the diagonal and ^{13}C's pairs that are close in space are linked by symmetric off-diagonal peaks (**Figure 7**).

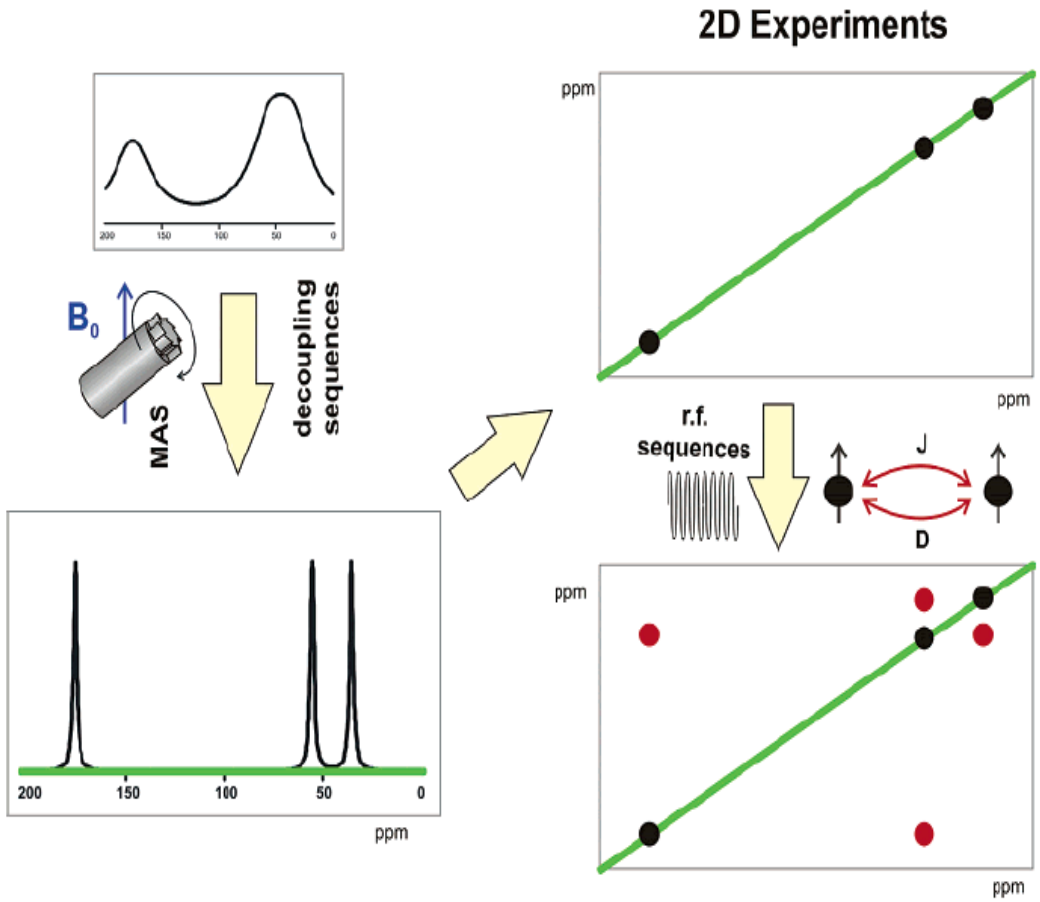

Figure 7: A schematic diagram of basic techniques for the investigation of istopically labeled biomolecular system in solid-state NMR, involving 1D and 2D NMR spectroscopic tools. [Adapted from Ref.36]

1.5. Results and Discussion

1.5.1. Structural Frameworks of Melanin

Melanin synthesized *in vitro* with a panel of catecholamine substrates such as L-dopa, methyldopa, epinephrine, and norepinephrine exhibited significant differences with respect to yield, color of soluble and insoluble products, surface charge, stable free radical content, antibody binding and other physical features [3]. These characteristic physiochemical differences between various catecholamine-derived pigments can be attributed to their structural divergence. Cross-polarization (CP) MAS ^{13}C spectra of melanins produced using different catecholamines as precursor showed the structural fingerprints of the pigments. The ^{13}C spectrum of L-dopa melanin revealed the presence of open chain aliphatic methylene groups ($(CH_2)_n$, 20-40 ppm), oxygenated aliphatic carbons (CH_nO, 60-80 ppm), aromatic and/or olefinic carbons (110-160 ppm) and carboxyls (172 ppm) (**Figure 8A**). This compositional finding was consistent with the previously reported studies of *C. neoformans* L-dopa melanin [5]. In addition, the CPMAS spectrum (**Figure 8B**) of the L-dopa substrate is distinctly different from the pigment, demonstrating the metabolic transformation of the obligatory precursor.

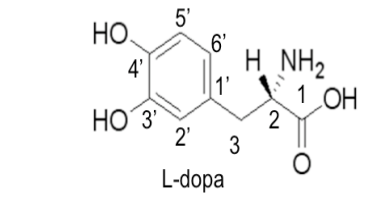

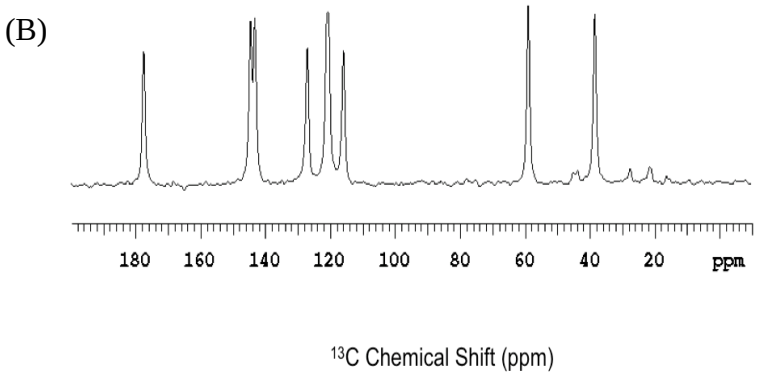

Melanin

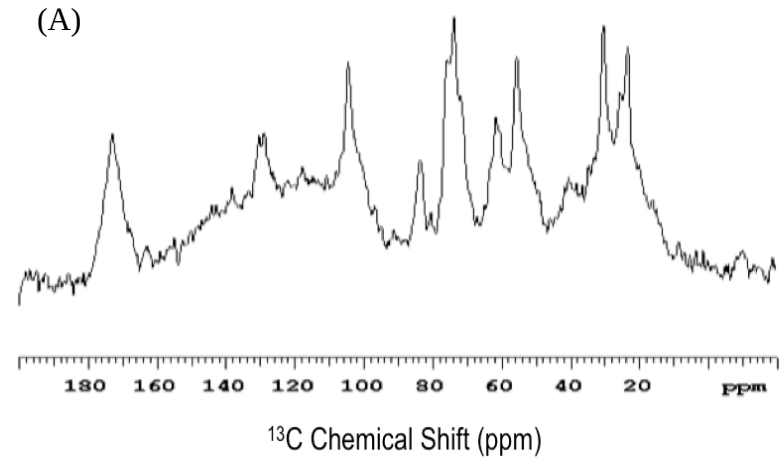

Figure 8: CPMAS ^{13}C spectra (150 MHz) of melanin produced with L-dopa (A) and L-dopa precursor (B). Both ^{13}C spectra were acquired at 15 kHz spinning frequency.

The aromatic peaks (114 ppm, 120 ppm, 128 ppm, and 145 ppm) of the L-dopa precursor possibly retained their aromatic characteristics in the polymeric form (**Figure 8A**), whereas the two peaks at 38 ppm and 58 ppm (**Figure 8B**) shifted significantly due to melanin production. The broader aromatic resonance in the melanin spectrum can be attributed to the structural heterogeneity and/ or proximity to unpaired electrons. In addition, the pigment spectrum exhibits new peaks at 25-85 ppm, indicating significant differences in the structural form of the biopolymer compared with the precursor.

To improve the spectral resolution and dispersion, CPMAS experiments have been conducted with various temperatures, spinning frequencies, and magnetic field strengths (**Figures 9-12**). Using higher magnetic field enhanced the spectral resolution, ruling out chemical shift heterogeneity as a cause of the broad appearance of the aromatic region of low-field melanin spectra (**Figure 9**). Lowering the temperature improved the overall signal-to-noise ratio of the melanin spectra as expected based on a more favorable Boltzmann factor, although it disfavored the signal intensity of carbonyl molecular groups, possibly because of their long spin relaxation times (**Figure 10**). Enhancing spinning speed caused a modest improvement in ^{13}C detection for the aliphatic and carboxyl resonances (**Figure 11**). ^{13}C spectral editing revealed the groups of non-protonated and highly mobile protonated carbons present in L-dopa melanin, supporting the involvement of glucose metabolites in melanin formation (**Figure 12**).

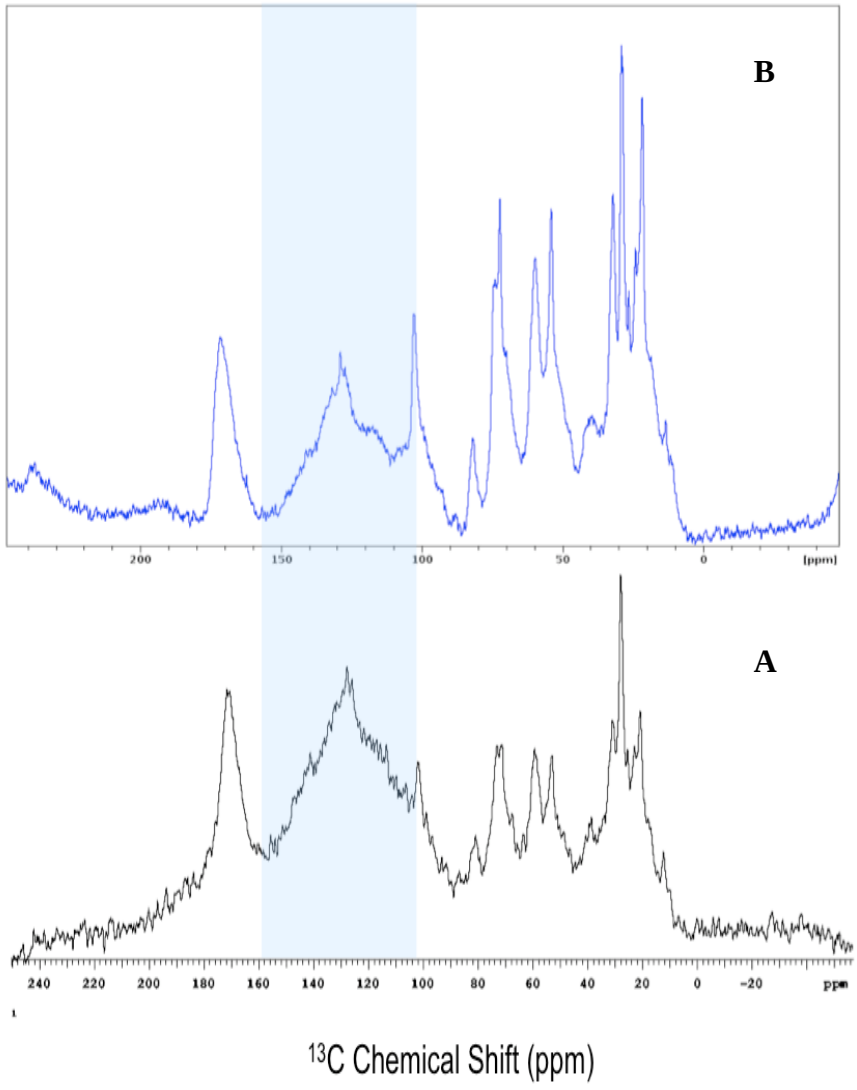

Figure 9: CPMAS ^{13}C spectra of methyldopa melanin. The data were acquired at different magnetic field strengths, 600 MHz (A) and 900 MHz (B), respectively. The sample was spun at 15 kHz.

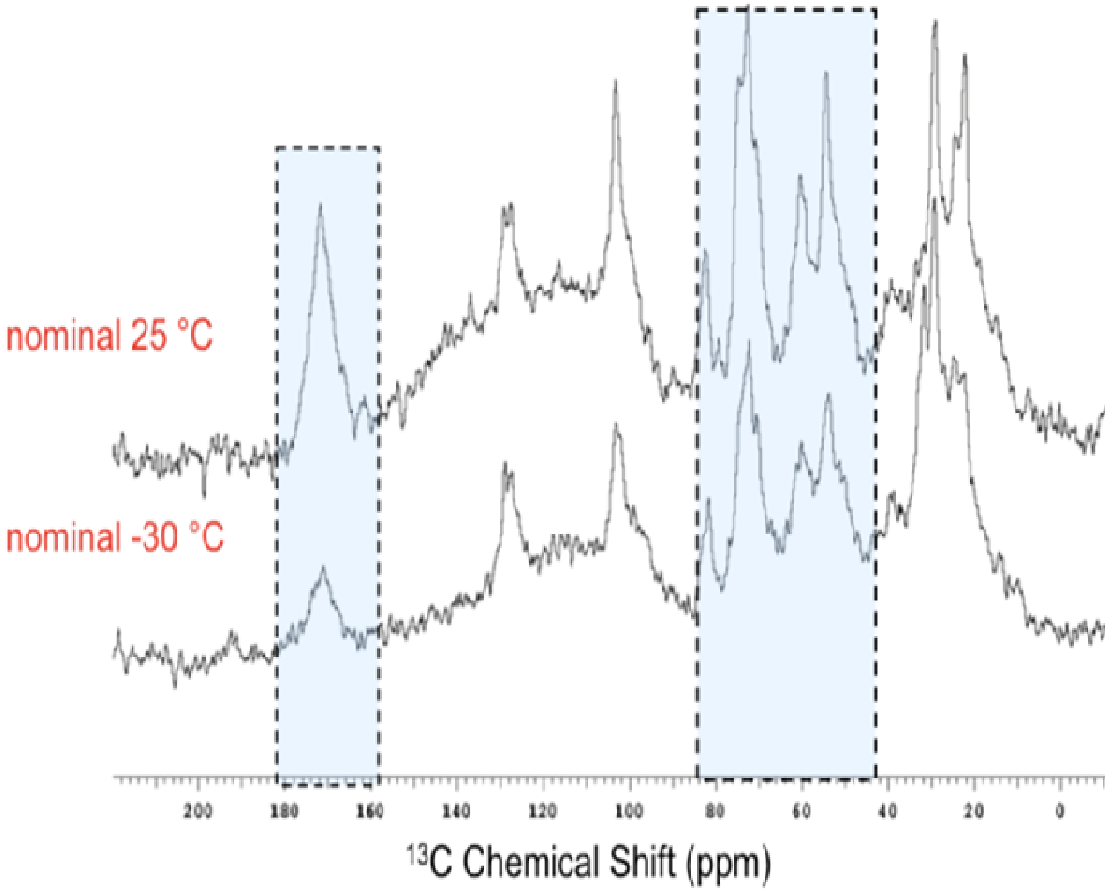

Figure 10: 150 MHz ^{13}C CPMAS spectra of L-dopa melanin. The data were acquired at different temperatures. The sample was spun at 30 kHz.

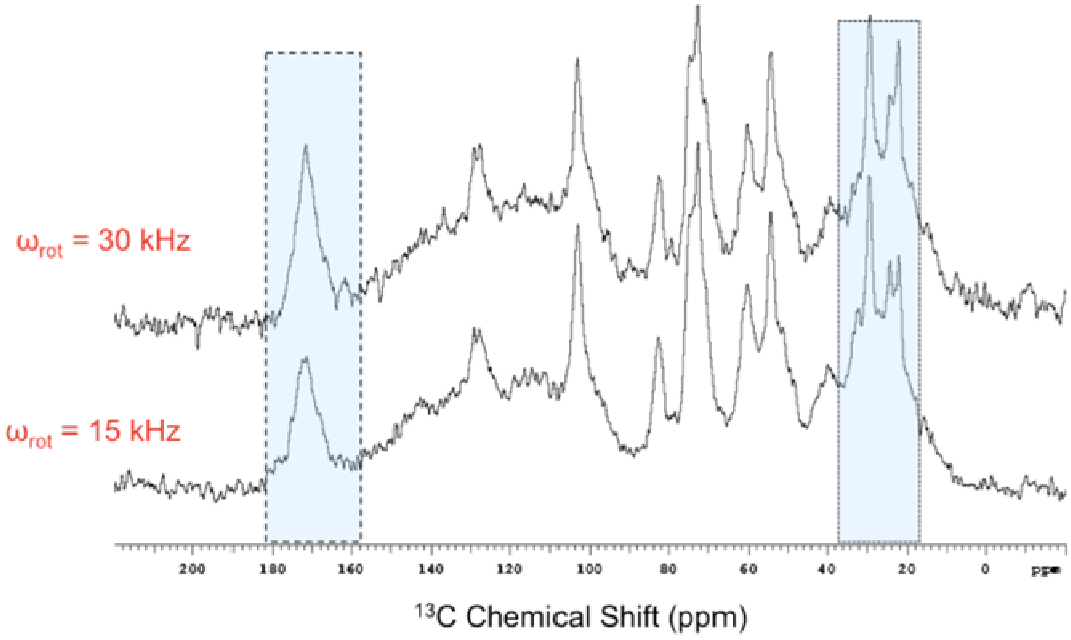

Figure 11: 150 MHz ^{13}C CPMAS spectra of L-dopa melanin. The spectra were acquired at two different spinning frequencies and at room temperature.

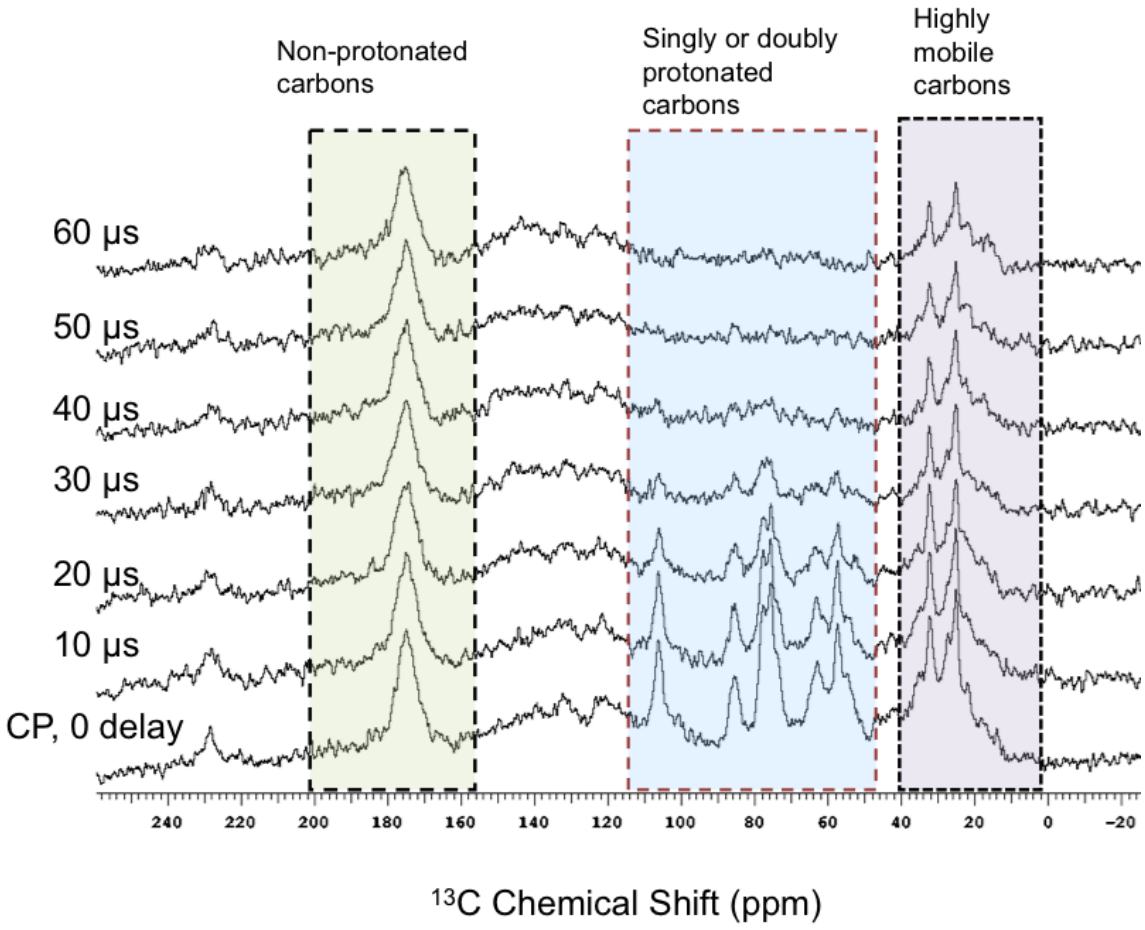

Figure 12: 150 MHz ^{13}C CPMAS spectra of L-dopa melanin. The spectra were acquired at 8 kHz spinning frequency. The introduction of a series of time delays (10 µs- 60 µs) in the proton decoupling (Figure 5) showed the dephasing of the singly and doubly protonated carbons.

The molecular composition of L-dopa melanin was also used as a basis for structural comparison between the pigments obtained from various catecholamine substrates. **Figures 13-14** show CPMAS ^{13}C NMR results for *C. neoformans* melanins synthesized in the presence of methyldopa, and epinephrine.

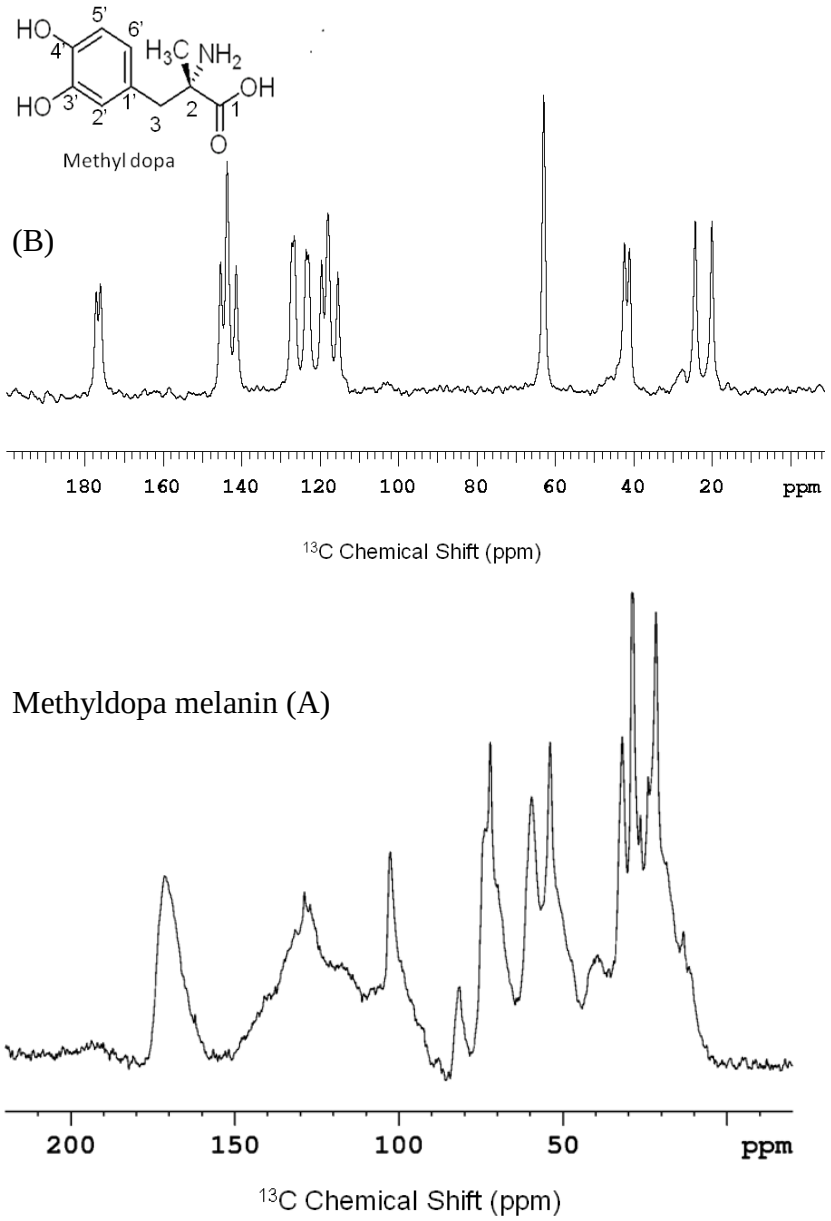

Figure 13: (A) CPMAS ^{13}C spectrum (225 MHz) of melanin produced with methyl dopa. (B) CPMAS ^{13}C spectrum (150 MHz) of methyldopa precursor. Both ^{13}C spectra were acquired at 15kHz spinning frequency.

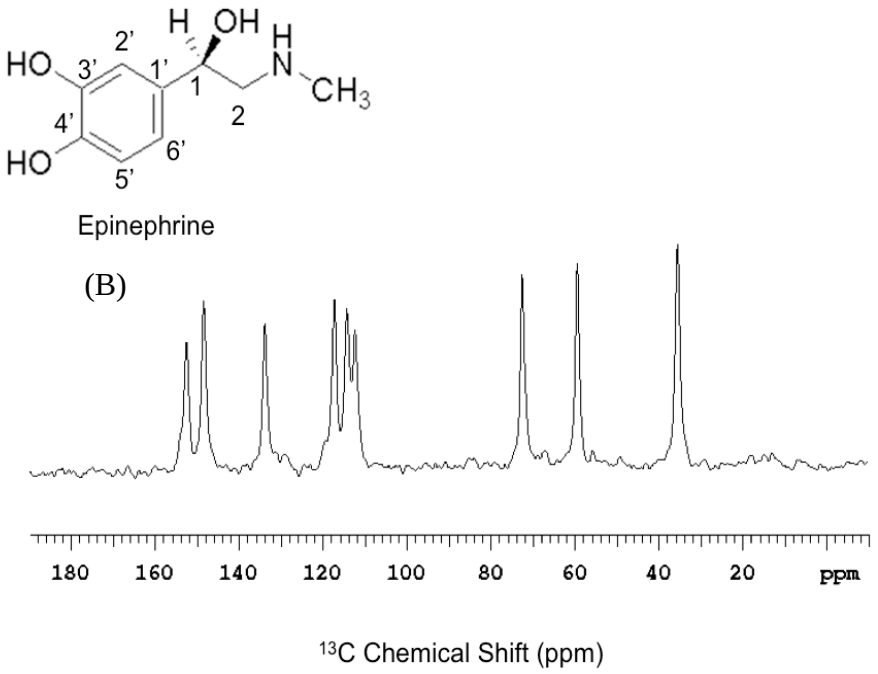

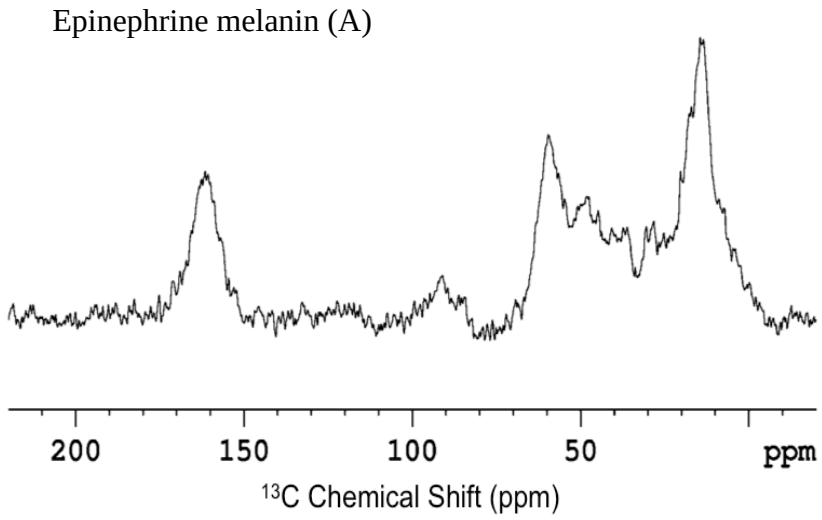

Figure 14: (A) 225 MHz ^{13}C CPMAS spectrum of melanin generated from epinephrine. (B) 150 MHz ^{13}C CPMAS spectrum of epinephrine precursor. The data were acquired at 15 kHz spinning frequency.

A comparison of the ^{13}C spectra of methyldopa (**Figure 13B**) and epinephrine (**Figure 14B**) to their respective pigments (**Figures 13A & 14A**) demonstrates the metabolic transformation of the precursors into structurally different polymeric forms. In case of methyldopa precursor, the aromatic ring of the precursor (110-150 ppm) is possibly converted to a heterogeneous aromatic structure in the pigment, exhibiting a broad aromatic resonance (**Figure 13A**). Conversely, the less prominent aromatic resonance in the biopolymer produced with epinephrine (**Figure 14A**) suggested a possible loss of aromatic ring structure of the precursor or severe line broadening during the metabolic transformation.

The ^{13}C spectrum of methyldopa melanin exhibited considerable similarity to the pigment generated from L-dopa, particularly in the aromatic region, suggesting a common pathway for the polymerization of the precursors to form the pigments (**Figure 15**). Conversely, both aromatic resonances (110-160 ppm) and the aliphatic regions (20-80 ppm) of the ^{13}C spectra of the pigments that were produced with norepinephrine and epinephrine showed different compositional characteristics compared to the spectrum of L-dopa melanin (**Figure 15**). Previous biophysical studies showed that the pigments isolated from *C. neoformans* cells grown in the presence of epinephrine and norepinephrine were substantially different from the L-dopa and methyldopa melanins in terms of the color of soluble and insoluble parts, yield, and paramagnetic activity. Thus, ^{13}C NMR spectra of the pigments confirmed the structural differences in the catecholamine-derived fungal melanins and allowed interpretation in terms of differences for both indole networks and methylene chains of associated membrane constituents.

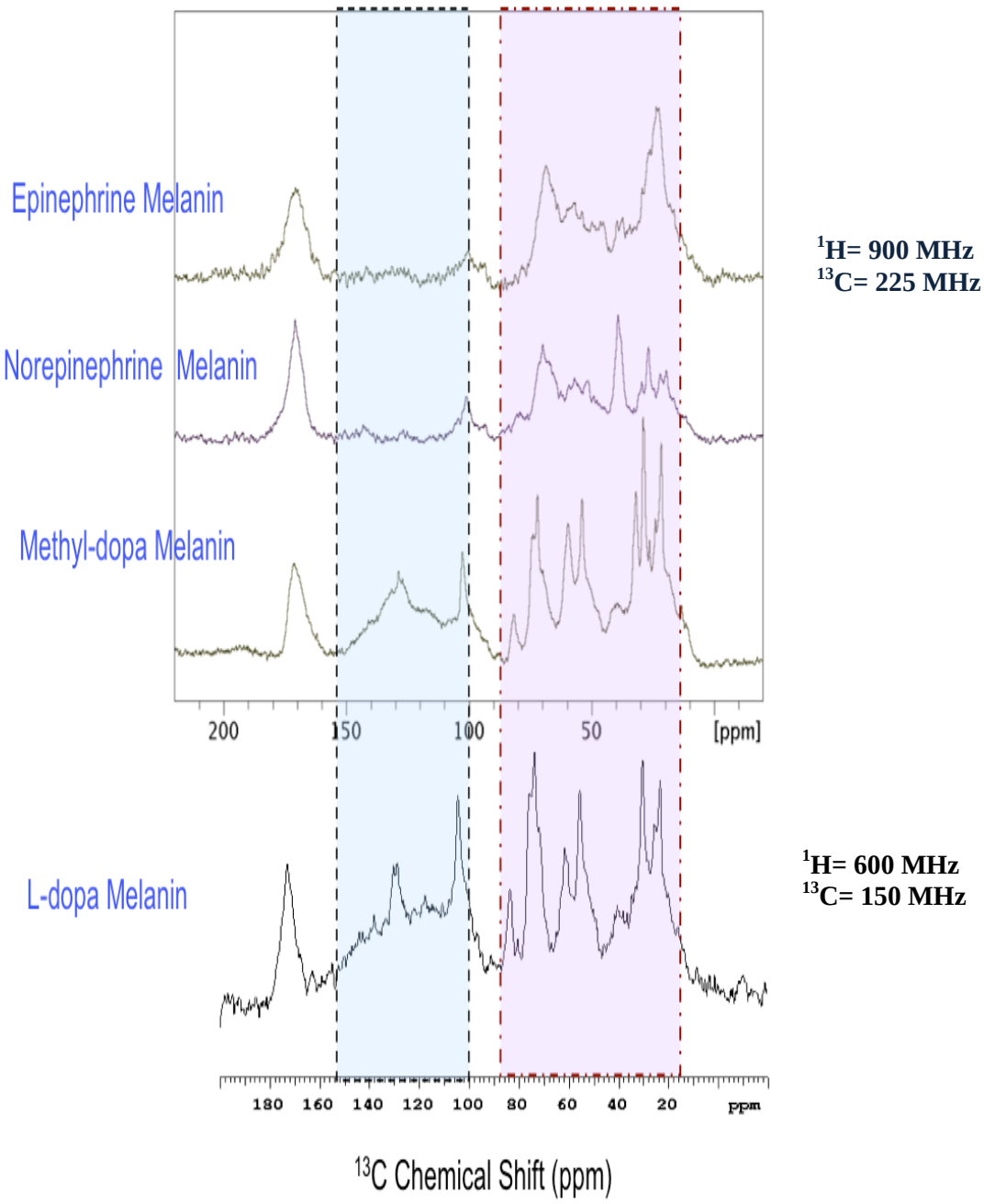

Figure 15: CPMAS ^{13}C spectra of melanins derived from four catecholamine precursors. All data were acquired at 15 kHz spinning frequency.

The cyclization of L-dopa that leads to indole formation is proposed to occur in *C. neoformans* via the Mason-Raper pathway (**Figure 16**) for melanin biosynthesis. The initial steps of the L-dopa oxidative cyclization process generate various cyclic intermediates such as dopachrome, DHI, and 5,6-indolequinone that finally lead to the production of the fungal eumelanin.

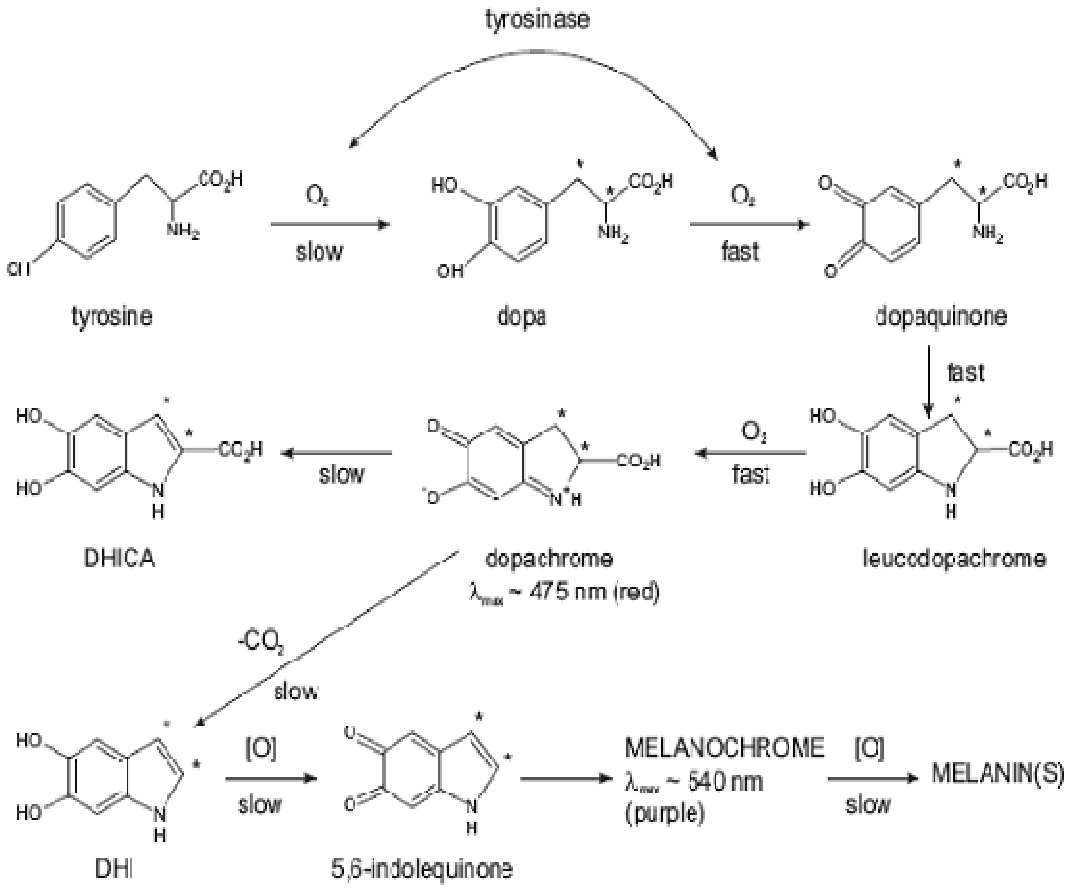

Figure 16: Mason−Raper scheme of melanogenesis. The early step in which tyrosinase catalyzes the conversion of tyrosine to L-dopa has been omitted .[Adapted from Ref.6]

In light of this proposal, it may be surprising that the ^{13}C spectrum of the fungal pigment generated from serotonin showed considerable similarity to the L-dopa melanin spectrum (**Figure 17**). The similarities between the structural fingerprints of the pigments generated from these two structurally different precursors suggest the possibility of an alternative pathway for melanin formation that excludes the initial cyclization steps proposed for L-dopa.

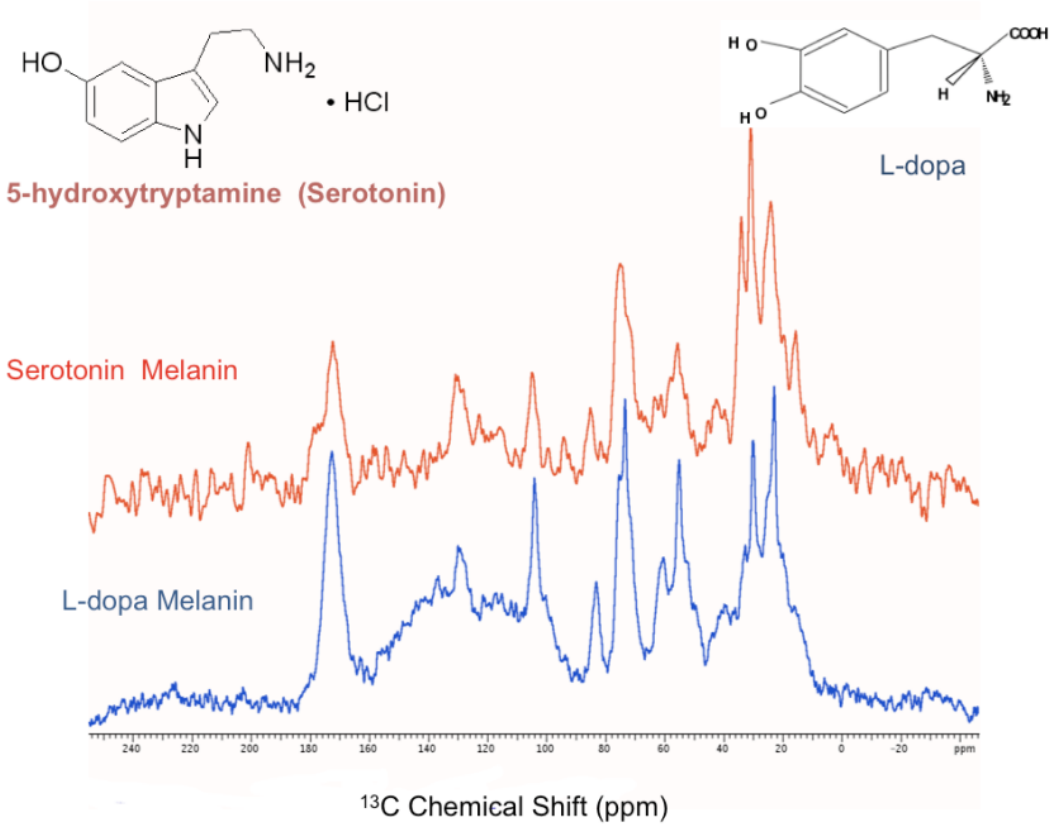

Figure 17: CPMAS ^{13}C spectra (150 MHz) of melanins derived from serotonin and L-dopa. The data were acquired at 15 kHz spinning frequency.

Although melanin biosynthesis is thought to involve the oxidative polymerization of L-dopa, the nature of connections to aliphatic moieties associated with the fungal melanin is not well understood. Previous studies have documented the possibility of covalently associated fungal cell wall components with the melanin as the pigment is deposited in the cell wall of *C. neoformans* [4-6]. The formation of aliphatic groups can be attributed to metabolic transformations of the glucose present in the chemically defined media in which the fungal cells were grown in the presence of the obligatory L-dopa precursor. Yet the association between the pigment and the fungal cell walls may depend on the particular cellular characteristics, as demonstrated by the use of a different cell line intended to optimize the yield of pigment biosynthesis. Compared to dopa-melanin extracted from the original cell line, this latter pigment showed enhanced yields but also significant differences in the aliphatic region of the ^{13}C spectrum (**Figure 18**).

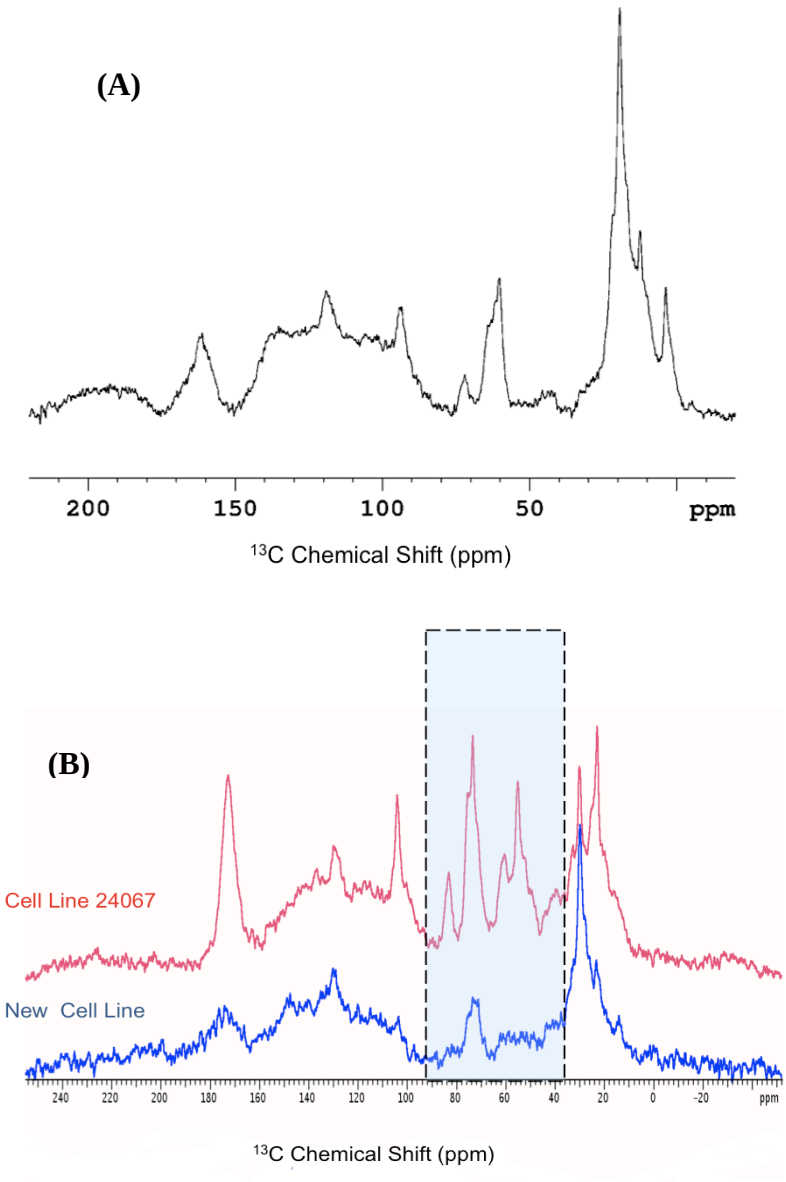

Figure 18: 225 MHz CPMAS ^{13}C spectrum of L-dopa melanin recovered from the new cell line (A). Figure 18B shows the comparison between 150 MHz ^{13}C spectra of L-dopa melanin extracted from two different cell lines. All data were acquired at 15 kHz spinning frequency.

Since the same extraction protocol was followed to recover both pigments grown using L-dopa as an obligatory precursor, the final products should presumably maintain similar structural characteristics. Additionally, the exhaustive chemical treatments during the extraction of the pigment are expected to remove all contaminations or loosely bound components, leaving only the strongly bonded chemical moieties of the pigment. Accordingly, the sparsely present oxygenated carbon groups (CH_nO, 40-80 ppm) in the structural fingerprint (**Figure 18**) suggest variations in the connections of the fungal cell wall components to the pigment and/or the possibility of a different metabolic transformation mechanism involved in the melanin biosynthesis.

As noted above, L-dopa has been shown to be an obligatory precursor of *C. neoformans* fungal melanin. Conversely, the pigment produced with epinephrine exhibited notable differences in the aromatic region compared to the dopa melanin. To investigate the competition and preferential uptake involving these two substrates, fungal melanin was synthesized with an equimolar mixture of L-dopa and epinephrine (1:1 mol/mol) and U-^{13}C-glucose. The ^{13}C NMR spectrum (**Figure 19**) of the pigment generated from the mixture of these two precursors exhibited a strong resemblance to the dopa melanin produced with ^{13}C glucose [6]; the spectrum is dominated by ^{13}C-glucose-derived resonances as expected. Considering the similarities in aliphatic region of the pigments, it can be suggested that fungal cell wall components that were derived from ^{13}C enriched glucose remained attached to the pigment generated from the equimolar mixture of L-dopa and epinephrine. This result suggested preferential incorporation of L-dopa into the final polymeric framework of the pigment. Using the spectral editing technique with the introduction of a time delay in proton decoupling, the singly or doubly protonated carbon

moieties in the polymeric structure were identified in the ^{13}C spectrum (**Figure 20**), which shows the gradual dephasing of the protonated carbon signals in the aliphatic region (50 -90 ppm).

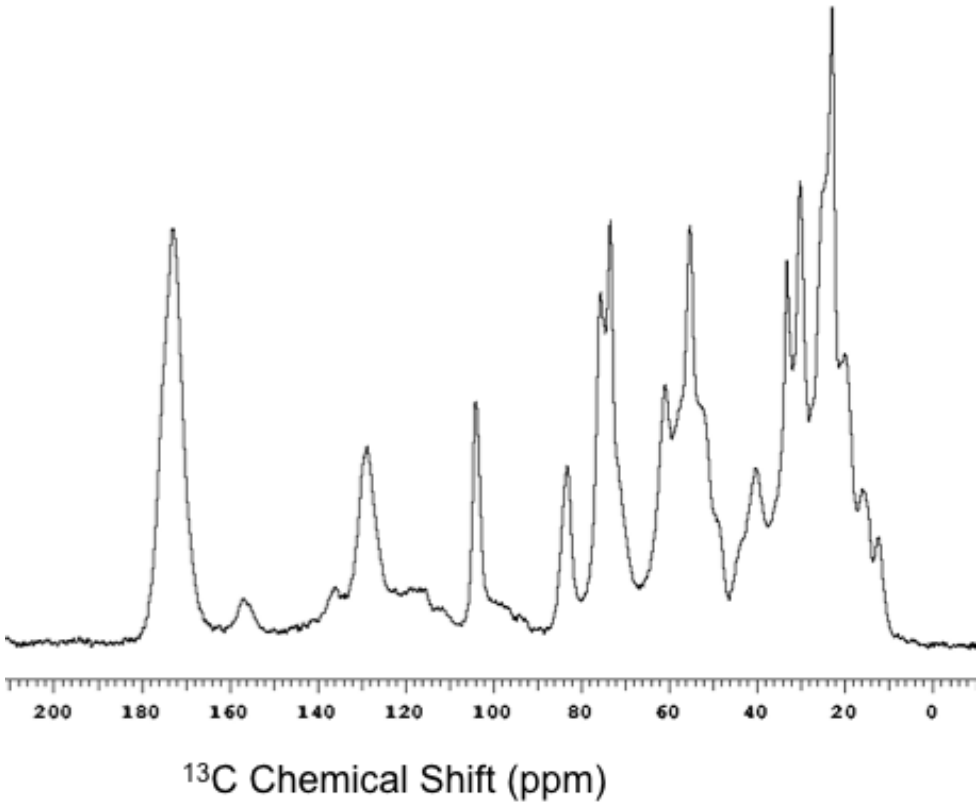

Figure 19: 150 MHz ^{13}C CPMAS spectrum of melanin generated from a mixture of L-dopa and epinephrine (1:1 mol/mol) and U-^{13}C-glucose. The spectrum was acquired at 15 kHz spinning frequency.

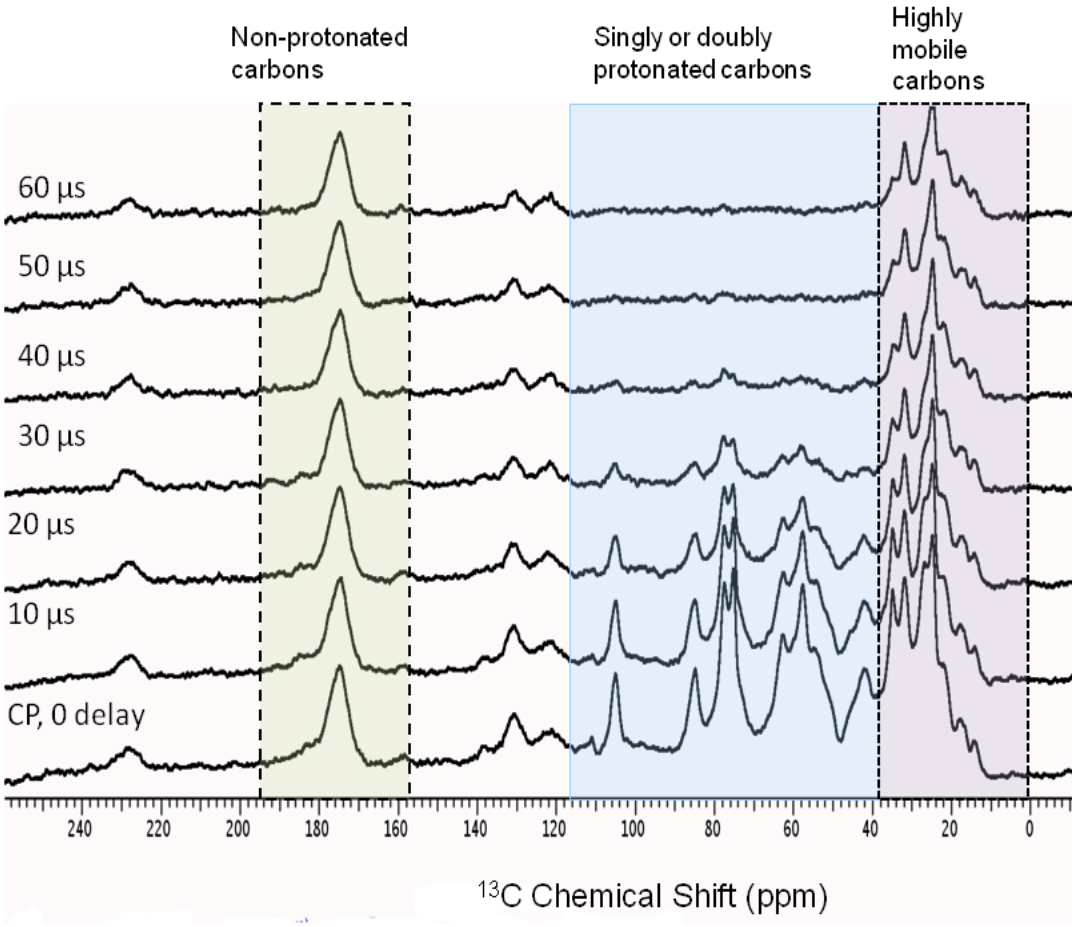

Figure 20: 150 MHz ^{13}C CPMAS spectra of melanin generated from a mixture of L-dopa and epinephrine (1:1 mol/mol) and U-^{13}C-glucose. The spectra were acquired at 8 kHz spinning frequency. The application of a series of time delays (10 µs- 60 µs) in the proton decoupling showed the dephasing of the singly or doubly protonated carbons.

1.5.2. Investigating melanin structure using isotopically labeled precursors

As *C. neoformans* requires exogenous precursors to produce melanin, it is possible to select different isotopic labeling schemes to unravel the molecular structure of the pigment derived from L-dopa. The fungal melanin synthesized using ring-^{13}C- L-dopa as a requisite precursor showed a prominent aromatic region in the CPMAS ^{13}C spectrum (**Figure 21**), describing the major aromatic constituents of the pigment. The broad appearance of the aromatic spectral region can be attributed to free radical content, chemical heterogeneity and unresolved ^{13}C-^{13}C couplings. In addition, the spectrum does not exhibit carboxyl resonances (172 ppm), indicating the absence of carbonyl (C=O) functional groups associated with the aromatic structure. This observation suggests the absence of a quinone type of structure (**Figure 16**) in the final polymeric form of the pigment. Delayed decoupling experiments demonstrated gradual suppression of the aromatic peak at 110 ppm with a considerable decrease in the overall intensity of the CP ^{13}C spectrum (**Figure 22**), indicating a heterogeneously protonated structural form of the aromatic groups in the biopolymer.

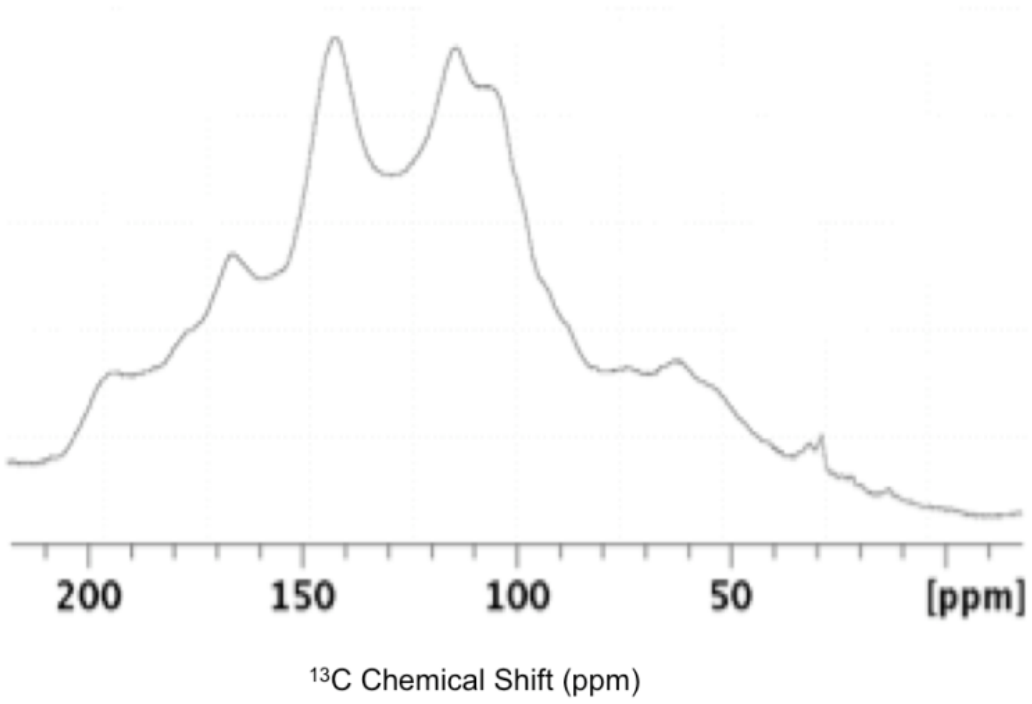

Figure 21: CPMAS ^{13}C (188 MHz) NMR spectra of melanin produced with ring ^{13}C -L-dopa and ^{12}C-glucose. The spectra were acquired at 10 kHz spinning frequency and room temperature.

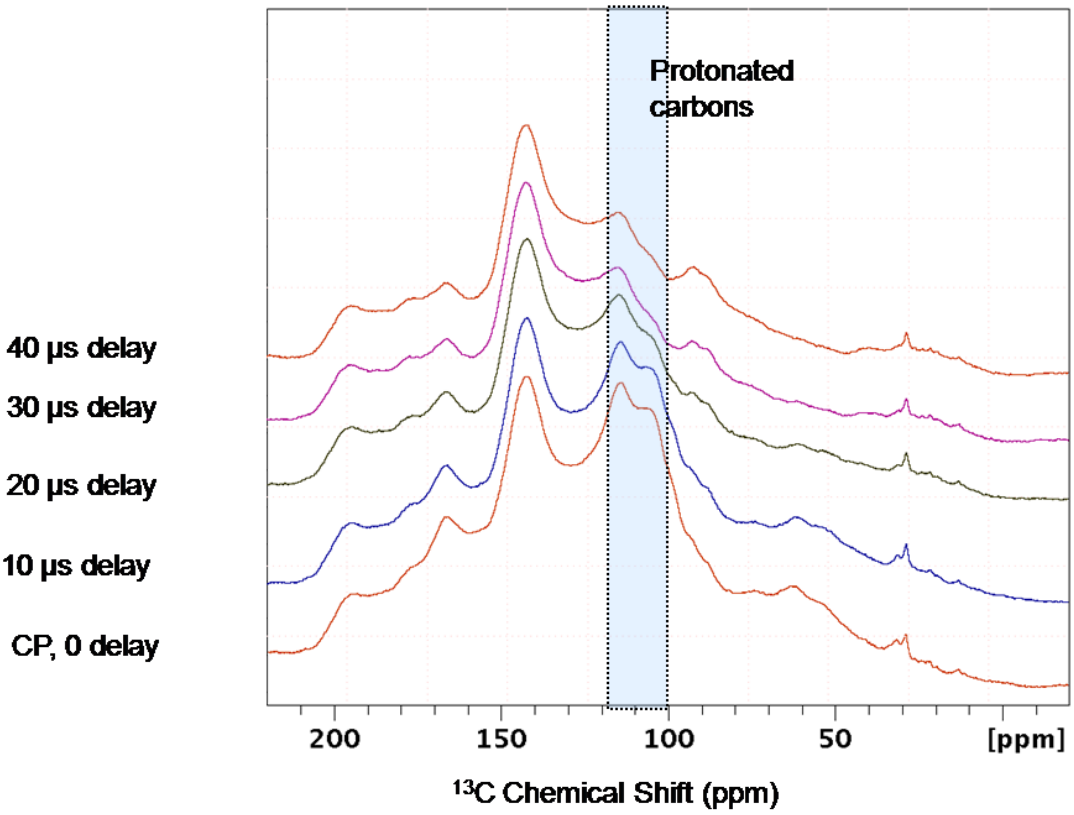

Figure 22: CPMAS ^{13}C (188 MHz) NMR spectra of melanin produced with ring ^{13}C -L-dopa and ^{12}C-glucose. The spectra were acquired at 10 kHz spinning frequency and at room temperature. The introduction of a series of time delays(10 µs- 40 µs) in the proton decoupling showed the dephasing of the protonated carbons.

The CPMAS ^{13}C spectrum of the pigment produced with ring-^{13}C- L-dopa and U-^{13}C-glucose exhibits the incorporation of ^{13}C groups into the molecular sites of the biopolymer from the precursors (**Figure 23**). With introduction of a series of time delay in the proton decoupling during the acquisition of ^{13}C signals in the CPMAS experiment (**Figure 24**), the protonated carbon groups became dephased, showing only the NMR signals from highly mobile long chain methylene groups (20-40 ppm), carbonyl /carboxyl groups (172 ppm) and selected aromatic sites (110-160 ppm) of the pigment.

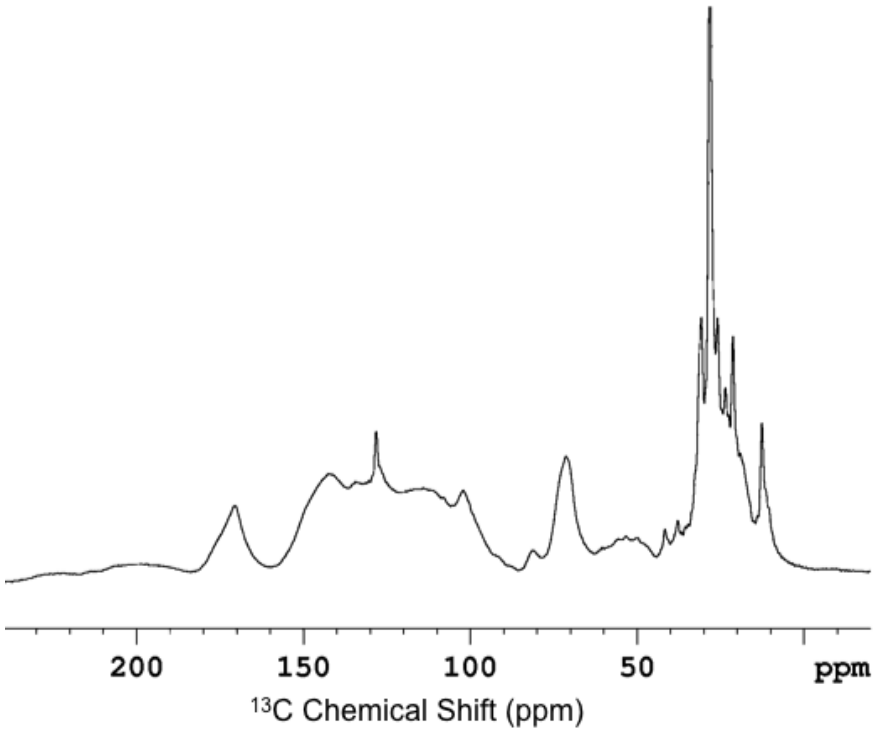

Figure 23: CPMAS ^{13}C (188 MHz) NMR spectra of melanin produced with ring ^{13}C -L-dopa and U-^{13}C-glucose. The spectra were acquired at 10 kHz spinning frequency and room temperature.

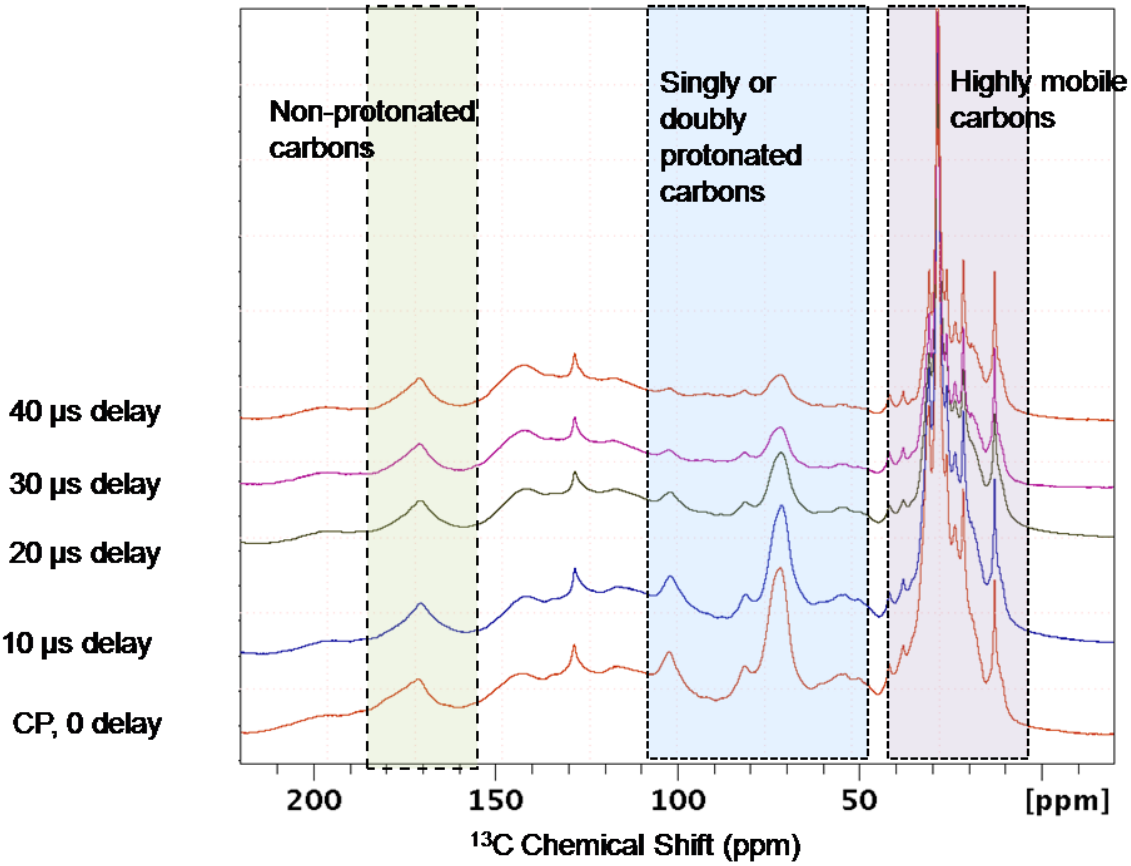

Figure 24: CPMAS ^{13}C (188 MHz) NMR spectra of melanin produced with ring ^{13}C -L-dopa and U-^{13}C-glucose. The spectra were acquired at 10 kHz spinning frequency and at room temperature. The introduction of a series of time delays (10 µs- 40 µs) in the proton decoupling showed the dephasing of the singly and doubly protonated carbons.

As the formation of indole structures via oxidative cyclization of L-dopa is imperative to produce melanin, 2,3-$^{13}C_2$-L-dopa was used to monitor the production pathways of *C. neoformans* melanin [6]. Previous NMR spectroscopic studies confirmed the incorporation of ^{13}C enriched sites of the precursor into the molecular structure of the pigment [6]. In addition, the Mason-Raper scheme suggested the formation of cyclic intermediates that ultimately lead to melanin production (**Figure 16**), and the process of cyclization requires the C-2 and C-3 carbons of L-dopa (**Figure 8B**) to be incorporated into the aromatic structure of the intermediates (carbons marked with asterisks in **Figure 16**). Previous structural studies with melanin derived from natural abundance L-dopa and ^{13}C enriched glucose highlighted the incorporation of glucose derived functional moieties such as long chain aliphatic groups, polysaccharides and carbonyls into the polymeric structure of the pigment [6]. The CPMAS ^{13}C spectra (**Figure 25**) of the fungal melanin synthesized from 2,3-$^{13}C_2$-L-dopa and U-^{13}C-glucose exhibited the characteristic distribution of the key functional groups originated from the isotopically enriched precursors. The broad aromatic resonance in the pigment (**Figure 25**) suggested the incorporation of isotopically enriched C-2 and C-3 carbon pairs of L-dopa into the aromatic structure of the pigment, corroborating the results mentioned in Ref. 6. The broad aromatic region of the spectrum (**Figure 25**) can be attributed to the heterogeneous nature of the aromatic component of the pigment as well as the presence of free radical content. The interrupted decoupling experiment also revealed the characteristic protonated carbon groups, showing the presence of oxygenated carbon moieties in the biopolymeric structure (**Figure 26**). With incorporation of ^{13}C-enriched substrate into the fungal melanin, an investigation of the spatial proximities of key molecular groups in the

pigment and cell wall becomes possible by designing two-dimensional (2D) ^{13}C-^{13}C correlation experiments.

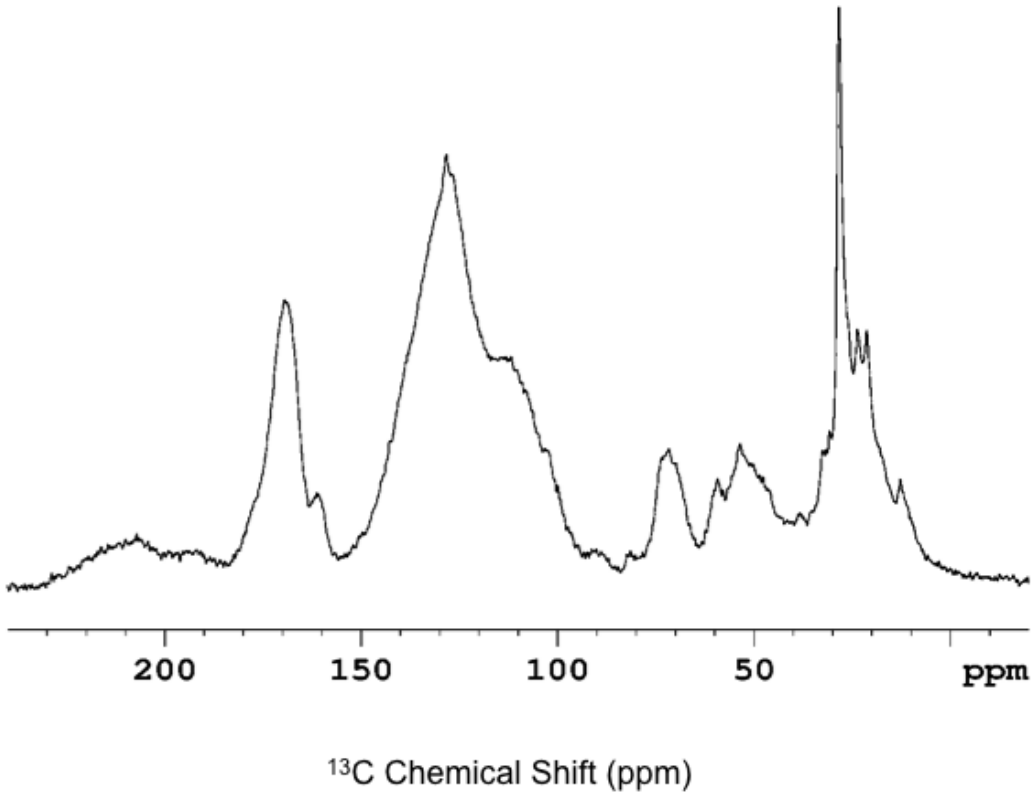

Figure 25: CPMAS ^{13}C (225 MHz) NMR spectrum of melanin produced with 2,3-$^{13}C_2$-L-dopa and U-^{13}C-glucose. The sample was spun at 15 kHz.

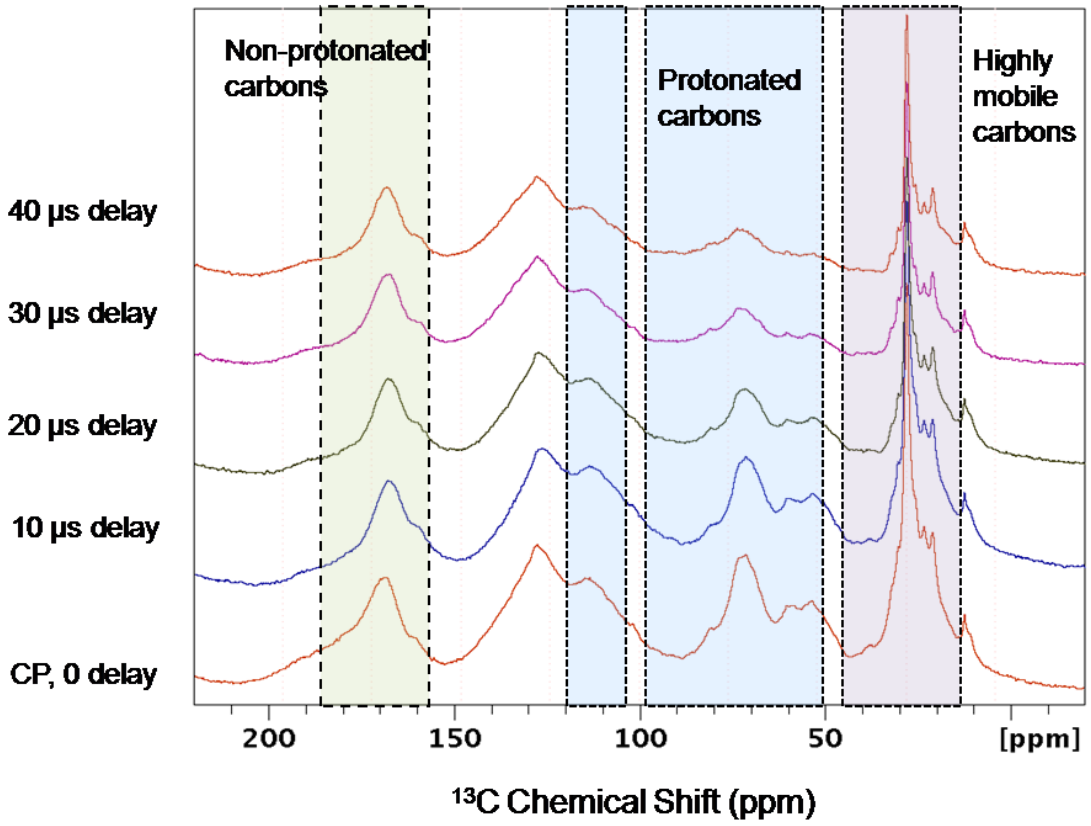

Figure 26: CPMAS ^{13}C (188 MHz) NMR spectra of melanin produced with 2,3-$^{13}C_2$-L-dopa and U-^{13}C-glucose. The spectra were acquired at 10 kHz spinning frequency and at room temperature. The introduction of a series of time delays (10 µs- 40 µs) in the proton decoupling showed the dephasing of the singly and doubly protonated carbons.

1.5.3. Exploring the possibility of proximity between fungal cell wall components and melanins

2D solid-state ^{13}C-^{13}C correlation studies have been carried out to investigate the spatial organization of key molecular groups of the pigment. Previous structural investigations of solvent-swelled melanin proposed covalent linking between the cell wall components and the melanin [6]. ^{13}C homonuclear correlation studies based on spin–diffusion measurements are a unique means to shed light on the through-space distance constraints on an isotopically labeled macromolecular system [32-34, 42-44]. The 2D dipolar assisted rotational resonance (DARR) technique relies on the through-space homonuclear dipolar coupling via proton irradiation by radiofrequency pulses and the through-space correlations of molecular groups are represented by relative positions of the cross peaks [42-44]. Accordingly, the cross peak intensities and their buildup rates with increasing mixing times show the spatial proximities between molecular sites in a polymeric system [34, 45, 46].

To investigate spatial connectivities between the molecular sites that originated via the metabolic transformation of glucose, 2D ^{13}C-^{13}C correlation investigation was carried out with the melanin generated from an equimolar mixture of L-dopa and epinephrine and uniformly ^{13}C-labeled glucose. **Figure 27** shows the 2D ^{13}C-^{13}C spectra of the pigment, which revealed the relative spatial positions of the glucose-derived molecular groups in the pigment. With an increase of the longitudinal DARR mixing time from 50 ms to 500 ms, the relative growth of the cross peaks showed the through-space connectivities between the moieties that were derived of the sugar source during the melanin biosynthesis.

With increasing DARR mixing time, the carbohydrate-alkyl chain crosspeaks at (74, 22), (82,22), and (104,22) grew in progressively. Similarly the cross peaks between polysaccharides and carboxyls at (172, 104) built up with longer DARR mixing time. Accordingly, ^{13}C-enriched glucose cross peaks were established for investigating the spatial contacts among the inter components in the pigment. From these results, it can be suggested that the ^{13}C glucose-derived moieties present in the pigment were within a 7 Å through-space distance.

Figure 27A

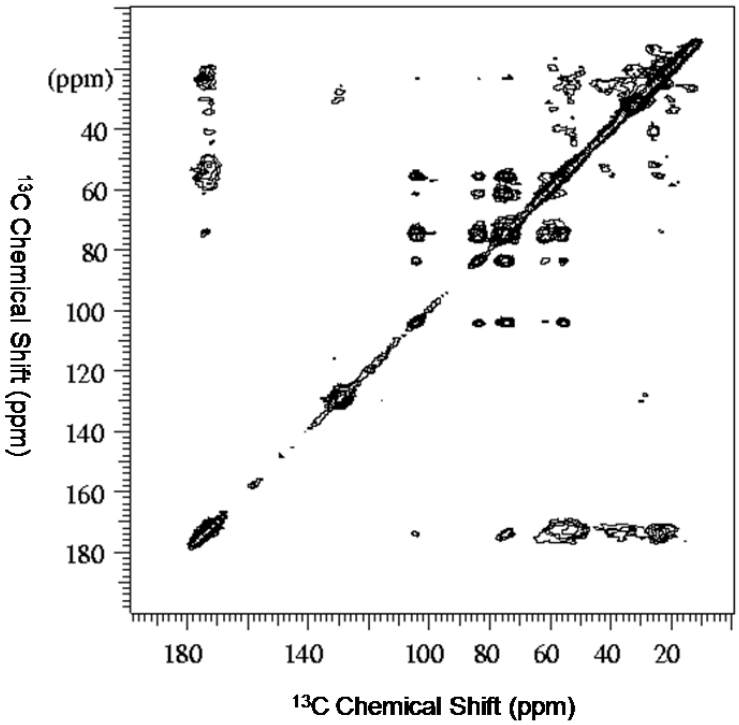

Figure 27B

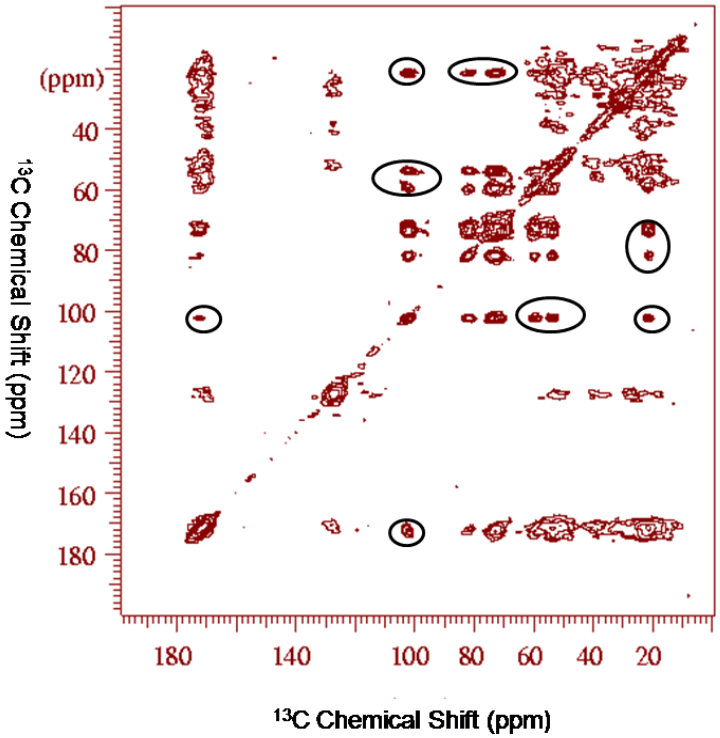

Figure 27C

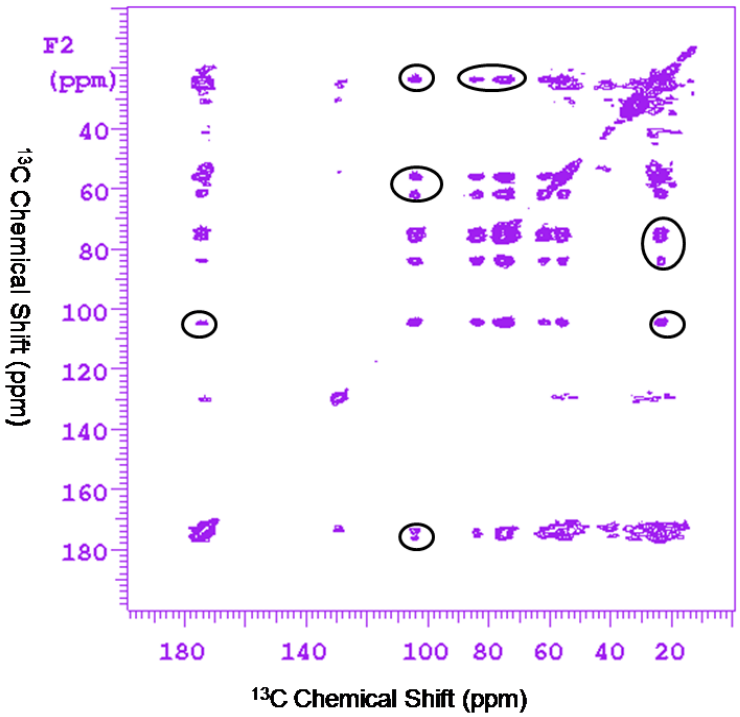

Figure 27: 2D ^{13}C-^{13}C chemical shift correlation spectra of melanin generated from an equimolar mixture of L-dopa and epinephrine and uniformly ^{13}C labeled glucose at 600 MHz with three DARR mixing times, 50 ms (A), 250 ms (B), and 500 ms (C). Circles designate cross peaks that grow in at longer mixing times.

To probe the distance constraints between the aromatic structures and the cell-wall components of the pigment, a comparative analysis of the through-space ^{13}C -^{13}C correlations was performed for two selectively labeled melanins: a pigment generated from ring-^{13}C-L-dopa and ^{12}C-glucose, and another pigment derived from ring-^{13}C-L-dopa and U-^{13}C-glucose.

The 2D ^{13}C spin diffusion measurement with 500 ms DARR mixing time revealed the through-space interconnections between carbon moieties generated from metabolic changes of the ^{13}C-enriched sugar source and the ^{13}C-labeled aromatic ring of the obligatory precursor which was transformed into the pigment (**Figure 28A**). An analogous ^{13}C-^{13}C measurement exhibited only the spatial contacts of the aromatic components generated form the ring-^{13}C-L-dopa precursor and U- ^{12}C-glucose as a sugar source (**Figure 28B**).

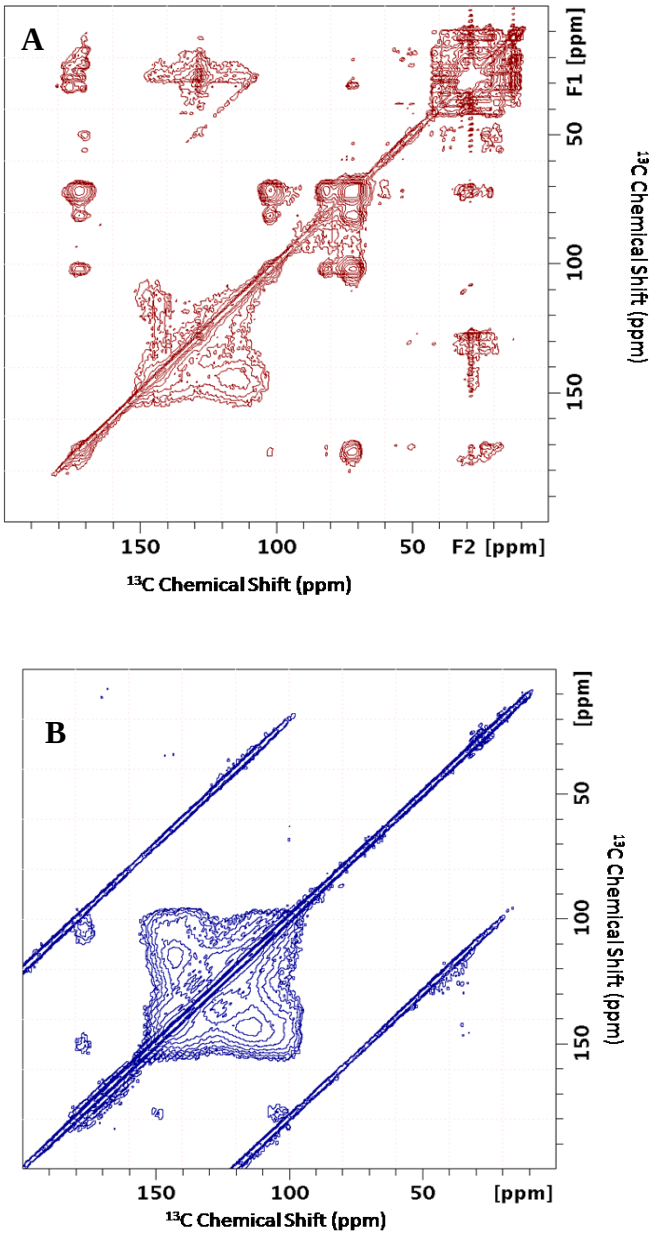

Figure 28: (A) 2D ^{13}C-^{13}C chemical shift correlation spectrum of melanin produced with ring-^{13}C-L-dopa and U-^{13}C-glucose at 750 MHz with 500 ms DARR mixing time. (B) 2D ^{13}C-^{13}C chemical shift correlation spectrum of melanin produced with ring-^{13}C-L-dopa and ^{12}C-glucose at 750 MHz with 500 ms DARR mixing time. Both spectra were acquired at 15 kHz spinning frequency and room temperature.

A comparison of these two solid-state ^{13}C-^{13}C chemical shift correlation studies and consideration of cross peaks derived solely from glucose (**Figure 27**) revealed the cross peaks between the aromatic components and the aliphatic moieties of the pigment, supporting the close association of the aliphatic components of the cell walls or membranes with the principal aromatic structure of the pigment (**Figure 29**).

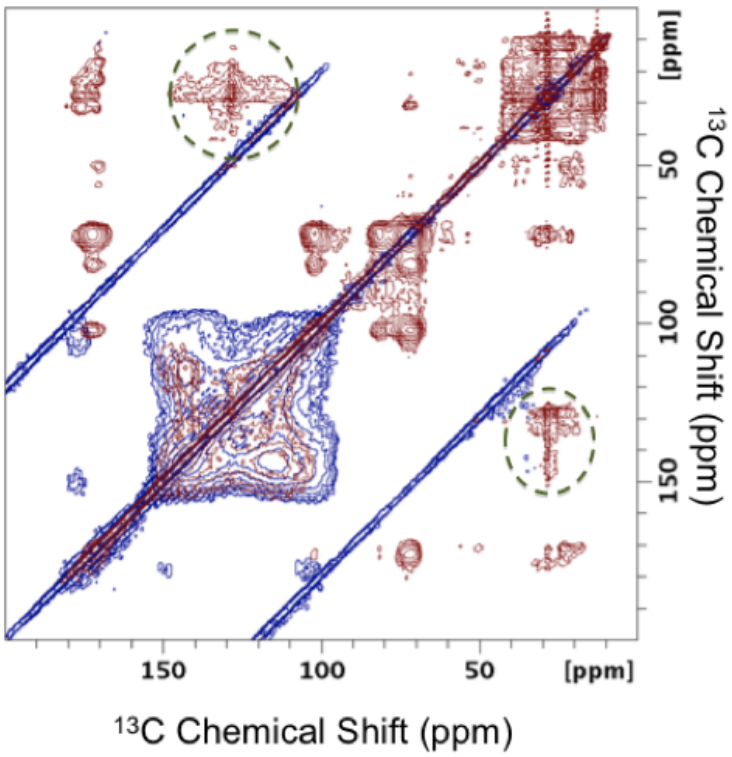

Figure 29: Superimposed 2D ^{13}C-^{13}C chemical shift correlation spectra of melanins produced with ring-^{13}C-L-dopa and ^{13}C-glucose (red), and ring-^{13}C-L-dopa and ^{12}C-glucose (blue). All spectra were obtained at 750 MHz with 500 ms DARR mixing time.

For the pigment generated from the 2,3-$^{13}C_2$-L-dopa substrate with ^{13}C enriched sugar source, the 2D solid-state ^{13}C-^{13}C chemical shift correlation experiments (**Figure 30**) with three different DARR mixing times (50 ms, 250 ms and 500 ms) exhibited the growth of cross peaks at (172, 123 ppm), supporting spatial contacts between the aromatic sites and carboxyl groups. The carboxyl groups were produced primarily from the ^{13}C enriched glucose, shown in the 1D (**Figure 19**) and 2D (**Figure 27**) ^{13}C spectra of the melanin produced with a mixture of natural abundance L-dopa and epinephrine and U-^{13}C glucose which was the only source of ^{13}C isotopic-enrichment in the preparation. Accordingly, 2D ^{13}C-^{13}C spin diffusion measurements with the melanin obtained from 2,3-$^{13}C_2$-L-dopa substrate with U-^{13}C-enriched sugar source confirmed the spatial connections between the aromatic sites and the sugar-derived components of the melanin ghosts. Together, these DARR results indicate proximities of six-membered ring with aliphatic chain moieties and of five-membered ring with carbonyl groups.

A series of similar experimental measurements (**Figure 31**) for the melanin produced with 2,3-$^{13}C_2$-L-dopa and U-^{13}C -glucose at higher magnetic field corroborated the results obtained at lower field, establishing the presence of spatial contacts between the aromatic sites of the pigment with the glucose-derived components.

Figure 30A

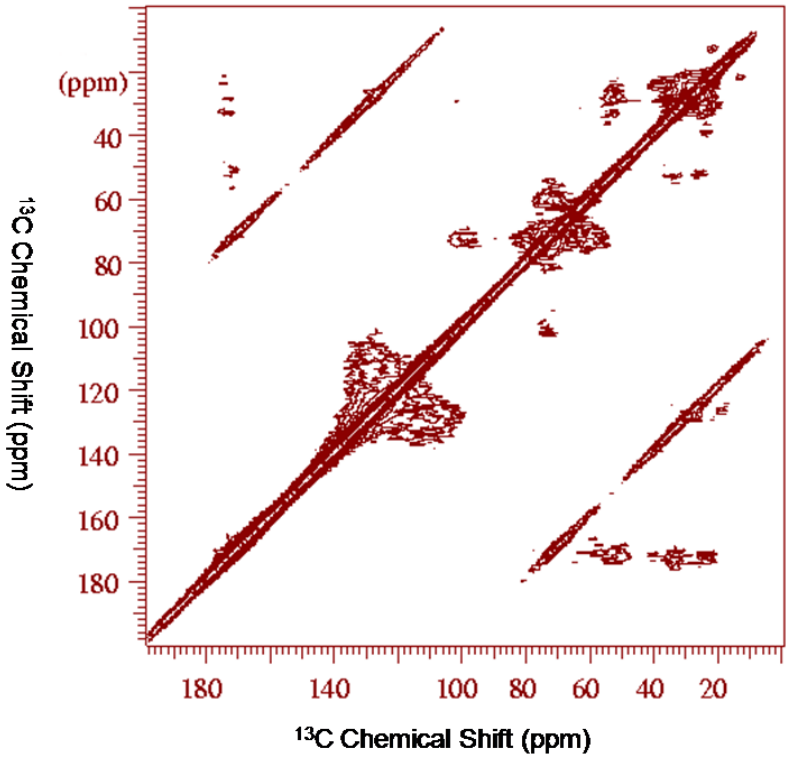

Figure 30B

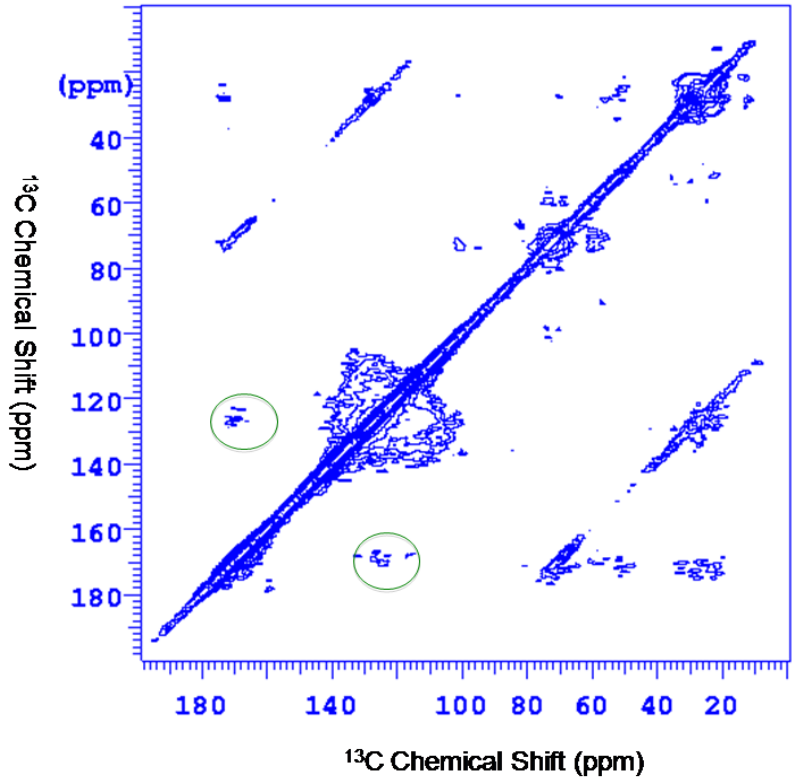

Figure 30C

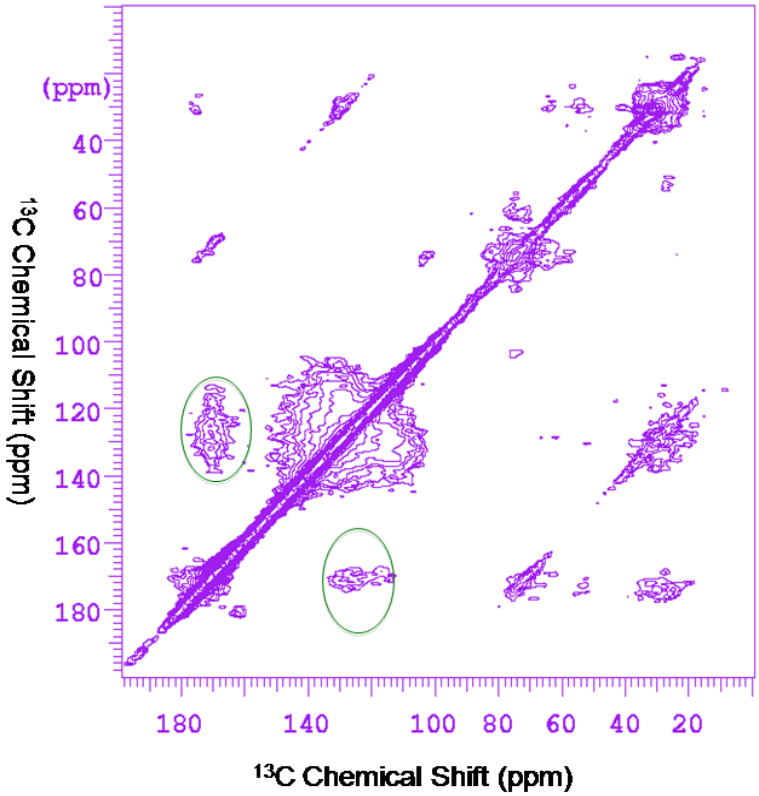

Figure 30: 2D ^{13}C-^{13}C chemical shift correlation spectra of melanin generated from 2,3-$^{13}C_2$-L-dopa and uniformly ^{13}C labeled glucose at 600 MHz with three DARR mixing times, 50 ms (A), 250 ms (B), and 500 ms (C). The data were acquired at room temperature and 15 kHz spinning frequency.

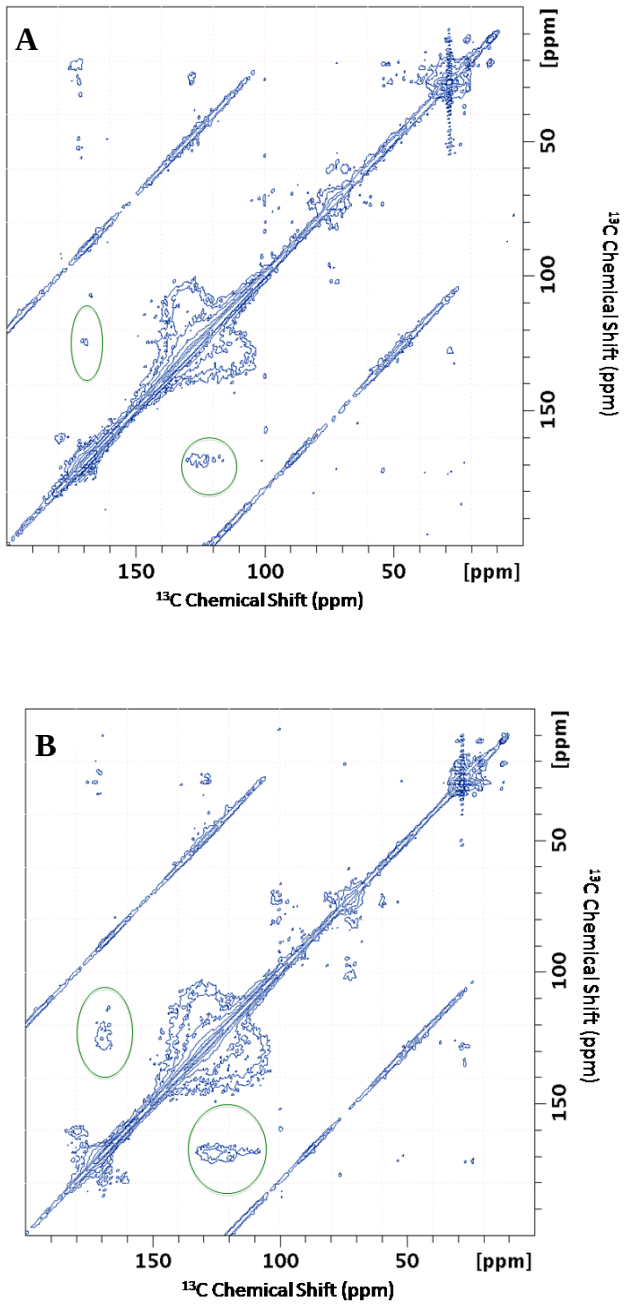

Figure 31:2D ^{13}C-^{13}C chemical shift correlation spectra of melanin generated from 2,3-$^{13}C_2$-Ldopa and uniformly ^{13}C labeled glucose at 750 MHz with two DARR mixing times, 250 ms (A), and 500 ms (B). The spectra were acquired at room temperature and 15 kHz spinning frequency.

As a sugar source, glucose can be metabolized through various enzymatic pathways to form numerous ^{13}C -labeled products incorporated into cell walls and/or lipid-like structures [6]. An alternative possibility is the incorporation of intact ^{13}C-enriched glucose as a major constituent the fungal cell wall and/or the source of aliphatic constituents associated with the pigment. Considering the extensive enzymatic and chemical treatments utilized to extract the melanin particles from the fungal cells, the presence of sugar-derived aliphatic moieties supports the possibility that the indole-based pigment is covalently associated with the fungal cell wall. Results of 2D solid-state ^{13}C-^{13}C chemical shift exchange studies (**Figures 27-31**) demonstrated through-space contacts between the key aromatic constituents of the pigment and various sugar-derived ^{13}C-groups in the pigment. The protonated aromatic moieties, which are derived from the six-carbon aromatic ring of L-dopa, are spatially close to the long-chain aliphatic groups derived from sugars. The five-carbon ring in the indole-based structural units of the pigment, which is generated by the cyclization of L-dopa, maintains the through-space connectivities to the carbonyl or carboxylate groups of glucose-derived moieties.

1.5.4. Synthesis of ^{15}N-labeled L-dopa precursor

A comprehensive molecular picture of the indole-based pigment can be achieved by investigating ^{15}N-enriched melanin along with studies that have been pursued with ^{13}C-labeled pigments. Accordingly, it is imperative to synthesize ^{15}N-labeled L-dopa to proceed with this investigative goal, as an isotopically enriched melanin can be recovered when *C. neoformans* cells are grown in the presence a labeled obligatory precursor. An enzyme-based oxidation method [47-48] was used to synthesize ^{15}N-labeled L-dopa from $^{15}NH_2$-L-tyrosine as a starting substrate. Tyrosinase, a copper containing enzyme, catalyses the oxidation of L-tyrosine to produce orthodiphenol [47-48]. Tyrosinase was immobilized on chitosan flakes used as a support and glutaraldehyde was used as a cross-linking agent. Afterwards, the immobilized enzyme was used to accomplish the oxidative conversion of $^{15}NH_2$-L-tyrosine to ^{15}N-labeled L-dopa. L-ascorbate was used simultaneously to inhibit further oxidation to dopachrome, yielding only L-dopa as a final product [47-48]. UV-Vis optical absorption and HPLC techniques were used for preliminary characterization of the final product. This tyrosinase-based oxidation method has been developed as an efficient and cost-effective alternative to chemical synthesis of ^{15}N-labeled L-dopa. The production of melanin was tested by growing fungal cells in the presence of the synthesized L-dopa; spectroscopic studies are ongoing.

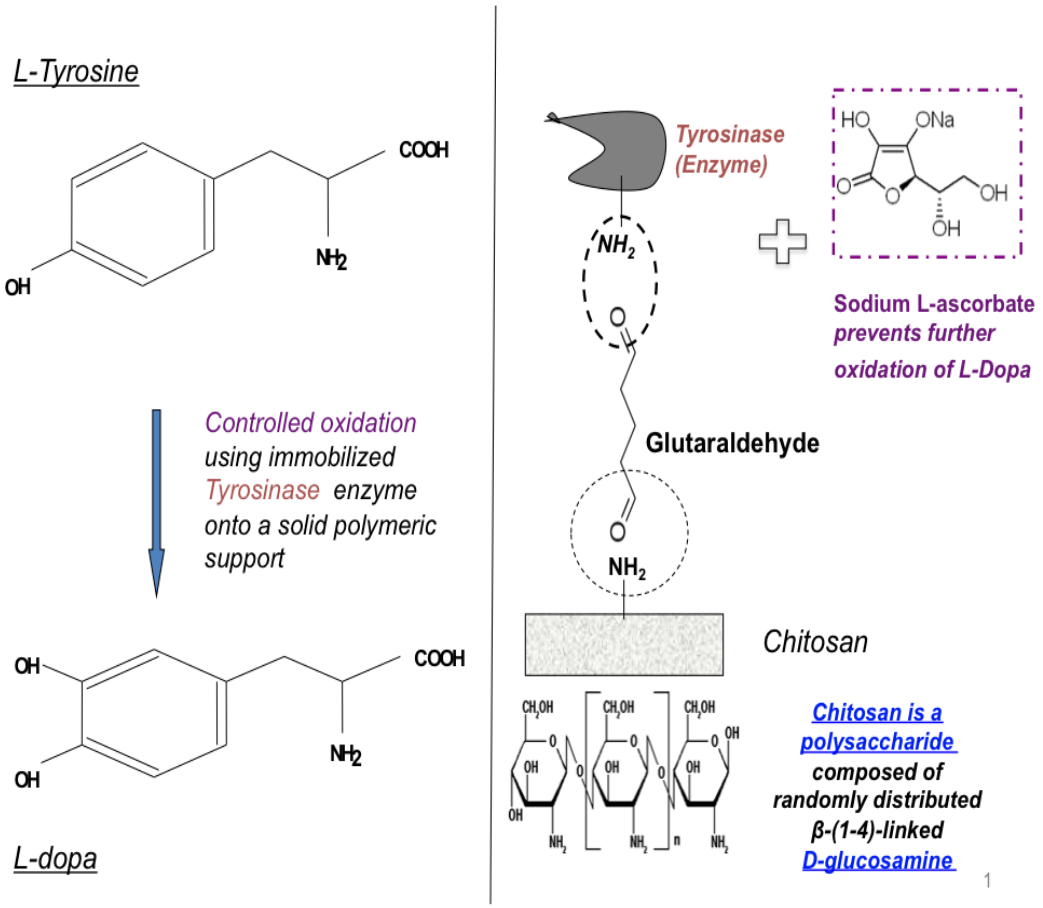

Figure 32: A schematic diagram showing L-dopa synthesis.

1.6. Conclusions

Solid-state NMR methods offer a unique means for the structural investigation of a biologically important but intractable polymer, melanin, which is associated with fungal virulence and drug resistance. In light of melanin's amorphous and heterogeneous physical characteristics, the application of high magnetic field has proven to be particularly effective in unraveling structural characteristics of this enigmatic polymer. In addition, the requirement of exogenous obligatory precursors for the biosynthesis of *Cryptococcus neoformans* melanins provided unique opportunities for probing melanin structure and assembly in the fungal cell wall. Varying experimental conditions such as spinning speeds, temperatures, magnetic field strengths, 1D and 2D ^{13}C MAS NMR and specific isotopic labeling schemes together provided a powerful protocol to obtain structural fingerprints of the pigments. Fungal melanins generated from different precursors exhibited distinctive aromatic structural features, including surprising aliphatic moieties. The use of ^{13}C-enriched precursors revealed metabolic transformations and possible cross-linked molecular architectures of the pigments. The investigation of melanin biosynthesized with a 1:1 (mol/mol) L-dopa-epinephrine mixture and U-$^{13}C_6$-glucose as a sugar source highlighted the relative competition of exogenous precursors involved in pigment production. ^{13}C spectral editing revealed the groups of non-protonated and highly mobile protonated carbons present in L-dopa melanin, also supporting the involvement of glucose metabolites in melanin formation. 2D solid-state ^{13}C–^{13}C correlation (dipolar assisted rotational resonance) measurements revealed proximities between key molecular groups of the melanins produced with 2,3-$^{13}C_2$-L-dopa, ring-^{13}C-L-dopa, and U-$^{13}C_6$-glucose precursors and supported plausible covalent

bonding of fungal cell wall components to melanin. In summary, 1D and 2D NMR results provided essential clues to unravel the mystery of melanin structure and shed light on the overall metabolic pathways leading to fungal melanin formation, laying the groundwork for therapeutically useful modifications of this process.

1.7. References

1. Hill, H. Z., The Function of Melanin or 6 Blind People Examine an Elephant. *Bioessays* **1992**, 14 (1), 49-56.

2. Bell, A. A.; Wheeler, M. H., Biosynthesis and Functions of Fungal Melanins. *Annual Review of Phytopathology* **1986**, 24, 411-451.

3. Garcia-Rivera, J.; Eisenman, H. C.; Nosanchuk, J. D.; Aisen, P.; Zaragoza, O.; Moadel, T.; Dadachova, E.; Casadevall, A., Comparative analysis of *Cryptococcus neoformans* acid-resistant particles generated from pigmented cells grown in different laccase substrates. *Fungal Genetics and Biology* **2005**, 42 (12), 989-998.

4. Langfelder, K.; Streibel, M.; Jahn, B.; Haase, G.; Brakhage, A. A., Biosynthesis of fungal melanins and their importance for human pathogenic fungi. *Fungal Genetics and Biology* **2003**, 38 (2), 143-158.

5. Tian, S. Y.; Garcia-Rivera, J.; Yan, B.; Casadevall, A.; Stark, R. E., Unlocking the molecular structure of fungal melanin using C-13 biosynthetic labeling and solid-state NMR. *Biochemistry* **2003**, 42 (27), 8105-8109.

6. Zhong, J. Y.; Frases, S.; Wang, H.; Casadevall, A.; Stark, R. E., Following fungal melanin biosynthesis with solid-state NMR: Biopolyrner molecular structures and possible connections to cell-wall polysaccharides. *Biochemistry* **2008**, 47 (16), 4701-4710.

7. Nosanchuk, J. D.; Valadon, P.; Feldmesser, M.; Casadevall, A., Melanization of Cryptococcus neoformans in murine infection. *Molecular and Cellular Biology* **1999**, 19 (1), 745-750.

8. Rosas, A. L.; Nosanchuk, J. D.; Feldmesser, M.; Cox, G. M.; McDade, H. C.; Casadevall, A., Synthesis of polymerized melanin by *Cryptococcus neoformans* in infected rodents. *Infection and Immunity* **2000**, 68 (5), 2845-2853.

9. Duff, G. A.; Roberts, J. E.; Foster, N., Analysis of the structure of synthetic and natural melanins by solid-phase NMR. *Biochemistry* **2002**, 27 (18), 7112.

10. Bhavin B. Adhyaru; Novruz G. Akhmedov; Alan R. Katritzky; Clifford R. Bowers, Solid-state cross-polarization magic angle spinning 13C and 15N NMR characterization of Sepia melanin, Sepia melanin free acid and Human hair melanin in comparison with several model compounds. *Magnetic Resonance in Chemistry* **2003**, 41 (6), 466-474.

11. Casadevall, A., Evolution of Intracellular Pathogens. *Annual Review of Microbiology* **2008**, 62, 19-33.

12. Dadachova, E.; Nosanchuk, J. D.; Shi, L.; Schweitzer, A. D.; Frenkel, A.; Nosanchuk, J. S.; Casadevall, A., Dead cells in melanoma tumors provide abundant antigen for targeted delivery of ionizing radiation by a mAb to melanin. *Proceedings of the National Academy of Sciences of the United States of America* **2004**, 101 (41), 14865-14870.

13. Wang, Y. L.; Aisen, P.; Casadevall, A., Melanin, melanin "ghosts," and melanin composition in Cryptococcus neoformans. *Infection and Immunity* **1996**, 64 (7), 2420-2424.

14. Kayser, H.; Palivan, C. G., Stable free radicals in insect cuticles: Electron spin resonance spectroscopy reveals differences between melanization and sclerotization. *Archives of Biochemistry and Biophysics* **2006**, 453 (2), 179-187.

15. Sealy, R.; Hyde, J.; Felix, C.; Menon, I.; Prota, G., Eumelanins and pheomelanins: characterization by electron spin resonance spectroscopy. *Science* **1982**, 217 (4559), 545-547.

16. Reszka, K. J.; Matuszak, Z.; Chignell, C. F., Lactoperoxidase-Catalyzed Oxidation of Melanin by Reactive Nitrogen Species Derived From Nitrite (NO_2^-): An EPR Study. *Free Radical Biology and Medicine* **1998**, 25 (2), 208-216.

17. Kalyanaraman, B.; Felix, C. C.; Sealy, R. C., Photoionization and photohomolysis of melanins: an electron spin resonance-spin trapping study. *Journal of the American Chemical Society* **2002**, 106 (24), 7327.

18. Wielgus, A. R.; Sarna, T., Melanin in human irides of different color and age of donors. *Pigment Cell Research* **2005**, 18 (6), 454-464.

19. Hong, L.; Simon, J. D., Current understanding of the binding sites, capacity, affinity, and biological significance of metals in melanin. *Journal of Physical Chemistry B* **2007**, 111 (28), 7938-7947.

20. Nighswander-Rempel, S. P.; Riesz, J.; Gilmore, J.; Bothma, J. P.; Meredith, P., Quantitative Fluorescence Excitation Spectra of Synthetic Eumelanin. *The Journal of Physical Chemistry B* **2005**, 109 (43), 20629.

21. Stark, K. B.; Gallas, J. M.; Zajac, G. W.; Golab, J. T.; Gidanian, S.; McIntire, T.; Farmer, P. J., Effect of stacking and redox state on optical absorption spectra of melanins-comparison of theoretical and experimental results. *Journal of Physical Chemistry B* **2005**, 109 (5), 1970-1977.

22. Galvao, D. S.; Caldas, M. J., Polymerization of 5,6-Indolequinone - a View into the Band-Structure of Melanins. *Journal of Chemical Physics* **1988**, 88 (6), 4088-4091.

23. Cheng, J.; Moss, S. C.; Eisner, M.; Zschack, P., X-Ray Characterization of Melanins .1. *Pigment Cell Research* **1994**, 7 (4), 255-262.

24. Cheng, J.; Moss, S. C.; Eisner, M., X-Ray Characterization of Melanins .2. *Pigment Cell Research* **1994**, 7 (4), 263-273.

25. Geis, P. A.; Wheeler, M. H.; Szaniszlo, P. J., Pentaketide Metabolites of Melanin Synthesis in the Dematiaceous Fungus Wangiella-Dermatitidis. *Archives of Microbiology* **1984**, 137 (4), 324-328.

26. Brakhage A. A.; Langfelder, K.; Wanner, G.; Schmidt, A; Jahn, B., Pigment biosynthesis and virulence. *Contributions to microbiology* **1999**, 2, 205-15.

27. Missall, T. A.; Moran J. M.; Corbett, J. A.; Lodge, J. K., Distinct stress responses of two functional laccases in *Cryptococcus neoformans* are revealed in the absence of the thiol-specific antioxidant Tsa1. *Eukaryot. Cell* **2005**, 4,202.

28. Williamson, P. R., Biochemical and Molecular Characterization of the Diphenol Oxidase of Cryptococcus-Neoformans - Identification as a Laccase. *Journal of Bacteriology* **1994**, 176 (3), 656-664.

29. Williamson, P. R., Laccase and melanin in the pathogenesis of Cryptococcus neoformans. *Front Biosci* **1997**, 2, e99-e107.

30. Polacheck, I.; Kwonchung, K. J., Melanogenesis in *Cryptococcus-Neoformans*. *Journal of General Microbiology* **1988**, 134, 1037-1041.

31. Folch,J., Lees,M. and Stanley,G.H.S., A simple method for the isolation and purification of total lipides from animal tissues *J. Biol. Chem*.**1957**, 226, 497-509 .

32. Duer, M. J., Solid State NMR Spectroscopy: Principles and Applications. Wiley-Blackwell: 2002.

33. Laws, D. D.; Bitter, H. M. L.; Jerschow, A., Solid-state NMR spectroscopic methods in chemistry. *Angewandte Chemie-International Edition* **2002**, 41 (17), 3096-3129.

34. McDermott, A., Structure and Dynamics of Membrane Proteins by Magic Angle Spinning Solid-State NMR. *Annual Review of Biophysics* **2009**, 38 (1), 385-403.

35. Tycko, R., Biomolecular solid state NMR: Advances in structural methodology and applications to peptide and protein fibrils. *Annual Review of Physical Chemistry* **2001**, 52, 575-606.

36. Luca, S.; Heise, H.; Baldus, M., High-resolution solid-state NMR applied to polypeptides and membrane proteins. *Accounts of Chemical Research* **2003**, 36 (11), 858-865.

37. Baldus, M., Solid-state NMR spectroscopy: Molecular structure and organization at the atomic level. *Angewandte Chemie-International Edition* **2006**, 45 (8), 1186-1188.

38. Schwalbe, H.; Bielecki,A., Recent Advances in High-Resolution Solid-State NMR Spectroscopy13. *Angewandte Chemie International Edition* **2001**, 40 (11), 2045-2050.

39. Peersen, O. B.; Wu, X. L.; Smith, S. O., Enhancement of CP-MAS Signals by Variable-Amplitude Cross Polarization. Compensation for Inhomogeneous B_1 Fields. *Journal of Magnetic Resonance, Series A* **1994**, 106 (1), 127-131.

40. Metz, G.; Wu, X. L.; Smith, S. O., Ramped-Amplitude Cross-Polarization in Magic-Angle-Spinning NMR. *Journal of Magnetic Resonance Series A* **1994**, 110 (2), 219-227.

41. Opella, S. J.; Frey, M. H., Selection of nonprotonated carbon resonances in solid-state nuclear magnetic resonance. *Journal of the American Chemical Society* **2002**, 101 (19), 5854.

42. Takegoshi, K.; Nakamura, S.; Terao, T., ^{13}C-^{1}H dipolar-assisted rotational resonance in magic-angle spinning NMR. *Chemical Physics Letters* **2001**, 344 (5-6), 631-637.

43. Takegoshi, K.; Nakamura, S.; Terao, T., ^{13}C-^{1}H dipolar-driven ^{13}C-^{13}C recoupling without ^{13}C rf irradiation in nuclear magnetic resonance of rotating solids. *The Journal of Chemical Physics* **2003**, 118 (5), 2325-2341.

44. Takegoshi, K.; Terao, T., 13C nuclear Overhauser polarization nuclear magnetic resonance in rotating solids: Replacement of cross polarization in uniformly ^{13}C labeled molecules with methyl groups. *The Journal of Chemical Physics* **2002**, 117 (4), 1700-1707.

45. Crocker, E.; Patel, A. B.; Eilers, M.; Jayaraman, S.; Getmanova, E.; Reeves, P. J.; Ziliox, M.; Khorana, H. G.; Sheves, M.; Smith, S. O., Dipolar assisted rotational resonance NMR of tryptophan and tyrosine in rhodopsin. *Journal of Biomolecular Nmr* **2004**, 29 (1), 11-20.

46. Yang, J.; Paramasivan, S.; Marulanda, D.; Cataidi, M.; Tasayco, M. L.; Polenova, T., Magic angle spinning NMR spectroscopy of thioredoxin reassemblies. *Magnetic Resonance in Chemistry* **2007**, 45, S73-S83.

47. Carvalho, G. M. J.; Alves, T. L. M.; Freire, D. M. G., L-DOPA production by immobilized tyrosinase. *Applied Biochemistry and Biotechnology* **2000**, 84-6, 791-800.

48. Ho, P. Y.; Chiou, M. S.; Chao, A. C., Production of L-DOPA by tyrosinase immobilized on modified polystyrene. *Applied Biochemistry and Biotechnology* **2003**, 111 (3), 139-152.

2.1. Introduction

Fluorescence spectroscopic measurements can give a plethora of information on a variety of molecular processes such as conformational changes of biomolecules, rotational diffusion and binding phenomena, solvent interactions, and distance between binding sites on a macromolecular system [1, 2, 3]. Progress in fluorescence technology is immensely beneficial for the development of cellular imaging [4, 5] and single-molecule detection [6, 7, 8]. Time-resolved fluorescence analysis reveals molecular information, which is usually lost during the time-averaging process [3, 9]. Thus, time-resolved experiments provide the information on molecular shape and conformations of the donor molecules and the local distribution of the acceptor molecules around the donors [3, 9, 10]. The present study dealt with the structural investigation of Y-shaped and double-stranded DNA using time-resolved fluorescence spectroscopy. An energy transfer mechanism involving gold nanoparticles as an acceptor was investigated to overcome the distance limitation of conventional fluorescence resonance measurements. Additionally, the plausible use of quantum dots as a fluorescence donor in the diffusion-controlled resonance energy transfer process was demonstrated with time-dependent fluorescence measurements.

Fluorescence resonance energy transfer (FRET) is a nonradiative energy transfer process between an excited donor and a ground state acceptor residing in the proximity of the donor molecule [1, 3, 10]. The rate of the energy transfer process, which originates from through-space long-range dipole-dipole interactions, is governed by several factors such as the extent of spectral overlap, the relative orientation of the transition dipoles, and the

distance between the donor and the acceptor molecules [1]. The efficiency of the energy transfer can be estimated from either steady-state or time-dependent measurements of the luminescence properties of the donor molecule. Steady-state measurements describe the change in fluorescence *intensity* of the donor in the presence of the acceptor. Similarly, time-resolved studies deal with the change in the fluorescence *lifetime* of the donor in the presence of the acceptor [3]. Fluorescence lifetime, an average value of the time spent by a fluorophore in the excited state prior to relaxing back to its ground state, determines the available time for a fluorophore to interact with or diffuse in its environment [1, 3, 10].

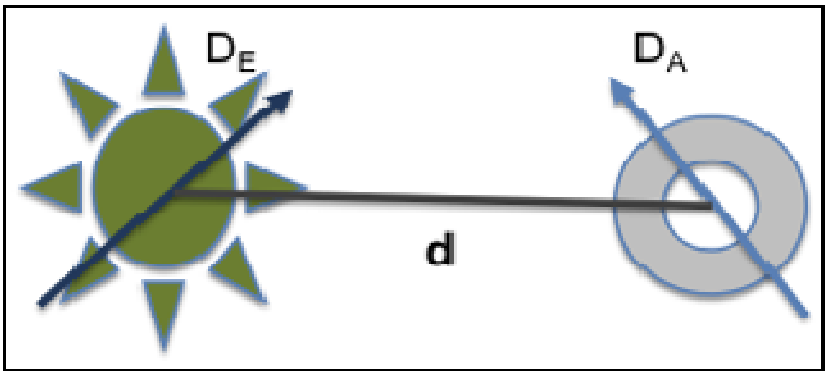

Figure 33: A donor-acceptor pair is separated by the distance *d*, and the arrows designated as D_E and D_A represent transition dipoles of donor and acceptor, respectively.

FRET efficiency (*E*) can be expressed in terms of the fraction of energy transferred from the excited donor to the acceptor through the nonradiative energy transfer process (k_{ET}) (**Eq.3**) [11].

$$E = \frac{k_{ET}}{k_f + k_{ET} + \sum_i k_i} \qquad [3]$$

In **Eq.3**, k_{ET} represents the rate of non-radiative energy transfer, whereas k_f is the rate of radiative decay of the emitter , and the rate constants k_i designate any other possible deactivation pathways of the donor [11].

The energy transfer rate (k_{ET}) is dependent on the lifetime of the donor (τ_D) in the absence of an acceptor, and the distance (*d*) between the donor and acceptor (**Eq. 4**) [1, 3, 11].

$$k_{ET}(d) = \frac{1}{\tau_D}\left(\frac{d_0}{d}\right)^6 \qquad [4]$$

The FRET efficiency (*E*) is inversely proportional to the 6th power of the distance (*d*) between the donor and acceptor, since the energy transfer process is governed by through-space transition dipole-dipole interaction (**Eq.5**) [1,12].

$$E = \frac{1}{1 + \left(\frac{d}{d_0} \right)^6} \qquad [5]$$

The physical distance (*d*) between a donor-acceptor pair involved in the FRET process can be evaluated in terms of the Förster distance (d_o), which is the distance corresponding to the 50% level of nonradiative energy transfer between a specific donor-acceptor pair. Whereas 50% of the excited donor molecules in the ensemble decay at d_0 through nonradiative energy transfer to the acceptor molecules, the other half use various radiative or nonradiative channels to decay to their ground state.

For practical purposes, the FRET process between a specific pair of donor and acceptor can be used to determine a distance range $d_0 \pm 0.5\ d_0$ [1]. The characteristic Förster distance (d_0) is dependent on the refractive index (*n*) of the medium, the quantum yield of the donor in the absence of the acceptor, and the overlap integral related to the degree of spectral overlap between the donor emission and the acceptor absorption. Thus, the Förster distance, d_0 (in Å), of a pair of donor and acceptor can be estimated from the spectral properties of the donor-acceptor system (**Eq. 6&7**) [1-3].

$$d_0 = 9.78 \times 10^3 \left[\kappa^2 n^{-4} \Phi_D J(\lambda)\right]^{1/6} \quad [6]$$

$$J(\lambda) = \int_0^{\infty} F_D(\lambda)\varepsilon_A(\lambda)\lambda^4 d\lambda \quad [7]$$

The integral $J(\lambda)$ designates the spectral overlap between the normalized emission of the donor F_D, and the absorption of the acceptor, $\varepsilon_{A,}$ at the range of emission wavelengths (λ) of the donor (**Eq. 7**) [1, 9-11].

In **Eq.6**, Φ_D denotes the quantum yield of the donor in the absence of the acceptor, n is the refractive index of the medium, which is typically assumed to be 1.4 for biomolecules in aqueous medium, and κ^2 describes the relative orientation of the transition dipoles of the donor and the acceptor [1,10]. The value of the transition dipole orientation factor can vary from 0 (perpendicular) to 4 (collinear or parallel). In general, κ^2 is approximated to be 2/3 for biological systems, based on various experimental analyses of mobility and dynamics of the linker of the donor and acceptor in a solution phase [1,10]. The Förster approximation assumes that the diffusion length of the donor-acceptor pair is small compared with the critical transfer distance (Förster distance), owing to high solvent viscosity. Thus, molecules remain stationary while the energy transfer process occurs, and an average value for orientation factor can be assumed due to rapid Brownian rotation [3].

The efficiency of the FRET process can be determined from steady-state (**Eq.8**) or time-resolved (**Eq.9**) measurements [1-12].

$$E = \left(1 - \frac{I_{DA}}{I_D}\right) \qquad [8]$$

$$E = \left(1 - \frac{\tau_{DA}}{\tau_D}\right) \qquad [9]$$

I denotes the relative donor fluorescence intensity in the absence (I_D) and presence (I_{DA}) of the acceptor, and τ represents the fluorescence lifetime of the donor in the absence (τ_D) and presence (τ_{DA}) of the acceptor.

An investigation of the energy transfer dynamics by measuring the lifetime of the fluorophore can offer insight into the donor-acceptor separation and the influence of the environment in which the donor and acceptor are situated. The time correlated single photon counting (TCSPC) technique involves an excitation of the fluorophore by a continuous and periodic train of short light pulses and measurement of the arrival time of single fluorescence photons (signal) with respect to the time of last excitation pulse [3,14]. TCSPC relies on the principle that the probability distribution for a single fluorescence photon is equivalent to the actual intensity-versus-time distribution for all photons emitted [3,14-17]. Hence, a histogram of arrival time of the emitted photons is built up after a repeated evaluation of this single photon's counting for a sufficiently large

number of times. TCSPC is capable of measuring decay dynamics at very low concentrations [14-17]. However, the temporal resolution of TCSPC is typically restricted to ~ 60 ps [3]. A single or multi-exponential mathematical model is used to analyze the emission dynamics and to extract lifetime values from the decay profile. In the multi-exponential model, the intensity is anticipated to follow a decay model that is the sum of individual single exponential decays (**Eq.10**) [3,14-17].

$$F(t) = \sum_{i=1}^{n} \alpha_i \exp(-t/\tau_i) \qquad [10]$$

In this expression (**Eq.10**), the τ_i denote the decay times, α_i are the amplitudes of the components at t =0, and n is equal to the number of decay times. In some cases, the fluorophores under investigation experience differences in their local environment and the emission dynamics cannot be related to a limited number of discrete decay times. The decay profile can be expressed more realistically in terms of a distribution of decay times according to an assumed distribution function.

The total decay law can be presented as the sum of the individual decays weighted by the amplitudes, where $\int \alpha(\tau)\, d\tau = 1.0$ [3],

$$F(t) = \int_{\tau=0}^{\infty} \alpha(\tau) \exp(-t/\tau) d\tau \qquad [11]$$

Typically, a Gaussian or Lorentzian lifetime distribution is used for the $\alpha(\tau)$ distribution.

The deduction of kinetic parameters from a decay profile in a time-dependent measurement requires the use of a reconvolution method, incorporating the response of instrument for excitation optical pulses (prompt) [3,14]. In principle, the prompt approximates a δ-function in comparison to the decay profile. Instrumental factors such as timing jitters introduced by the detector, electronic delays and optical components of an instrument, can cause a broadening of the pulse width. These instrumental responses can cause deviation from the δ-function approximation in the present setup where a 50 ps wide optical pulse is used to measure fluorescence lifetimes on the nanosecond time-scale. Accordingly, the decay model, *i(t)*, is required to be reconvoluted with the prompt (*P(t)*) before comparing the decay model with the measured decay (*F(t)*). Symbolically this reconvolution process can be expressed as **Eq.12** [3, 14].

$$F(t) = i(t) \otimes P(t) \qquad [12]$$

The iterative least squares reconvolution method is used for computing the convolution integral using assumed fit parameters to obtain the fitted decay function *F'*(t). Afterward,

the computed $F'(t)$ is compared with the decay $F(t)$ to assess the "goodness of fit", quantified by the parameter χ^2 (**Eq.13**). Thus, $F'(t)$ is consistently recalculated using a range of parameters until the best possible agreement between the values of $F'(t)$ and $F(t)$ can be reached with the minimization of χ^2 .

$$\chi^2 = \sum_{\text{data}} \left[\frac{\text{Actual deviation}}{\text{Expected deviation}} \right]^2 \qquad [13]$$

$$\chi^2 = \sum_N \left[\frac{F(i) - F'(i)}{\sigma(i)} \right]^2 = \sum_N [W(i)]^2 \qquad [14]$$

where σ (i) is the standard deviation of the ith data point and W(i) is the weighted residual. A perfect agreement between the data and the anticipated model with a specific set of fit parameters is found when the normalized χ^2 value (χ^2_R) is close to 1; a value less than 1.2 is generally considered to be acceptable [3].

$$\chi_R^2 = \frac{\chi^2}{N-p} = \frac{\chi^2}{\nu} \qquad [15]$$

In **Eq.15**, N is the dimension of the data set, p is the number of fitted parameters (floating parameters, and the denominator ν represents the number of degrees of freedom of the fit. For TCSPC the number of data points (N) is generally larger than the number of parameters, therefore (N-p) is approximately equal to N. Considering only random errors contributing to χ^2_R, this value is expected to be close to unity [3]. Additionally, a good fitting model can be assessed by inspecting visually the distribution of weighted residuals, which are expected to be a plateau and randomly distributed about zero for a perfect fit of the model to the decay profile [3, 14-17].

2.2. Investigating the energy transfer mechanism between a DNA conjugated organic donor and gold nanoparticle by time-resolved spectroscopy.

An investigation of molecular interactions and conformational changes of biomolecules such as proteins and nucleic acids is imperative to understand their structural and functional properties [1-3,9,10]. For instance, the conformational dynamics of DNA (Deoxyribonucleic acid) play a significant role in regulating cellular functions as well as modulating the sensitivity and selectivity of DNA-based sensors, promising diagnostic devices to decipher the genetic basis of diseases [18]. Förster resonance energy transfer (FRET), a fluorescence-based "spectroscopic ruler" technique [1], involves the non-radiative energy transfer between a pair of organic donor and acceptor molecules and is an attractive optical method to probe distance-dependent structural properties of a molecular system [1-3]. However, the application of FRET to study large macromolecules is restricted due to an upper distance limit of ~ 10 nm [1, 19]. Recently, the use of metallic nanoparticles as an acceptor in the energy transfer process has been claimed to surmount the distance-barrier of the conventional FRET method, offering a promising alternative to investigate conformational changes of macromolecules [20-22]. Although the resonance energy transfer (RET) between the donor fluorophore and the acceptor nanoparticle takes place at a longer distance, no standard rule for its distance-dependence has been established [23-25].

The conventional FRET process is based primarily on the rate of the nonradiative energy transfer between donor and acceptor molecules, appropriately tagged with a biomolecule of interest [1-3]. Owing to excitation, energy emitted from the donor molecule is

absorbed by the acceptor through distance-dependent dipolar coupling. The selection of a specific donor-acceptor system in the FRET is fundamentally dependent on the overlap of the emission band of the donor fluorophore with the excitation band of the acceptor molecule. The energy transfer process is controlled by the spatial proximity of the donor and acceptor. Any perturbation in the conformation of the biomolecule causes an alteration in the distance between the donor and acceptor, and consequently influences the energy transfer process. Thus, FRET can be utilized to elucidate dynamic conformational changes of biomolecules in microscopic detail [1-3, 7,9]. As FRET is regulated by the electromagnetic coupling of two dipoles involved in the conventional organic donor–acceptor system, the application of FRET to study large macromolecules suffers from the spatial limitation of 10 nm [19-20]. Metal nanoparticles have been used as a promising acceptor to overcome this distance barrier of the FRET measurement because of their unique size-dependent optical properties [18]. The application of nanoparticles as acceptors in the FRET method has significantly improved the quantum efficiency of the energy transfer process to probe a comparatively larger conformational change of a macromolecule, which, until now, has been out of reach of the conventional FRET technique involving an organic acceptor molecule [19-20]. The primary reason for the enhanced sensitivity of the energy transfer process is attributed to the electromagnetic interaction between the dipole of the donor fluorophore and the surface electrons of the metal nanostructure [19-20], which can take place at a longer distance compared to dipole-dipole coupling. Since the electronic distribution of a metallic nanoparticle is influenced by its size and shape, a suitably controlled nanoparticle can modulate the energy transfer process when it is placed in the vicinity of the donor molecule [19-20]. In

addition, the orientation of the electronic dipole of the donor with respect to the distance vector between the donor and nanoparticle leads to an alteration in the efficiency of the energy transfer process. Recent theoretical studies claimed that the distance-dependence of the resonance energy transfer (RET) involving the metal nanoparticle and organic donor fluorophore could vary depending on the conditions of the energy transfer process [25]. The ratio of the size of the nanoparticle and the distance vector between the donor and acceptor plays a crucial role in the energy transfer mechanism [25]. In addition, biosensing tools involving nanomaterials (e.g. quantum dots) conjugated with biomolecules are essentially based on the efficiency of the energy transfer process between acceptor and donor nanostructures [1, 21].

Time-resolved spectroscopic studies offer a unique approach to unravel the mechanistic details of the resonance energy transfer process involving a metal nanoparticle as an acceptor under both *in vitro* and *in vivo* experimental conditions [1, 3, 12-14]. In the present study, we investigated the distance–dependent mechanism of the resonance energy transfer process between fluorescein (donor) and gold nanoparticle (acceptor), both attached to DNA, using time-resolved spectroscopic method. The quenching efficiency of the gold nanoparticle as a function of distance between the donor and acceptor was determined by the time-resolved lifetime analyses of the donor molecule. A comparative analysis between RET and conventional FRET methods was performed to validate the enhanced efficiency of the RET mechanism involving a gold nanoparticle as the acceptor.

2.2.1. Experimental Method

The time-resolved fluorescence measurements were carried out using a time correlated single photon counting (TCSPC) system (Horiba Jobin-Yvon) at room temperature. A 50 ps diode laser operating at 1 MHz repetition rate and 467 nm emission wavelength was used as the excitation source. The time-resolved data analysis was performed with DAS6 software based on a deconvolution technique using the iterative nonlinear least squares method. The steady-state fluorescence spectra were acquired using a spectrometer with a Xenon lamp as an excitation source at 367 nm. FAM modified (5'-C_6- FAM) oligostrands were purchased from IDT DNA Technologies. 6-FAM (Fluorescein), which is a single-isomer derivative of fluorescein, is generally used in the pH range 7.5-8.5 as a fluorescent label and can be attached to the oligonucleotide. Commercially obtained gold nanoparticles (1.4 nm diameter) from Nanoprobes Inc. were attached to the complementary thiol labeled (HS-C_3) DNA strands. The resultant gold nanoparticle–dye conjugated double stranded (ds) DNA were prepared and purified following the experimental method reported in Ref. 26. (DNA samples used in this study were prepared by Prof. Dan Luo's group at Cornell University). For all steady state and time-resolved fluorescence measurements, 60 nM DNA solutions were prepared using TE buffer (Sigma Cat# 93302), maintaining the pH of the solution at 7.5.

2.2.2. Results and Discussion

The steady-state emission measurement of FAM attached to DNA showed a characteristic emission maximum at 518 nm with a full width at half maximum of ~ 30 nm (**Figure 34**). The time-resolved photo luminescence (PL) lifetime measurement of the FAM-DNA system at the emission maximum showed a single exponential decay with an average lifetime of 4.18 ns (± 0.02 ns) (**Figure 34**). These results confirmed that FAM remained as a stable monomer in the solution at the pH 7.5 [11], without forming a dimer or higher aggregate at the experimental conditions discussed herein.

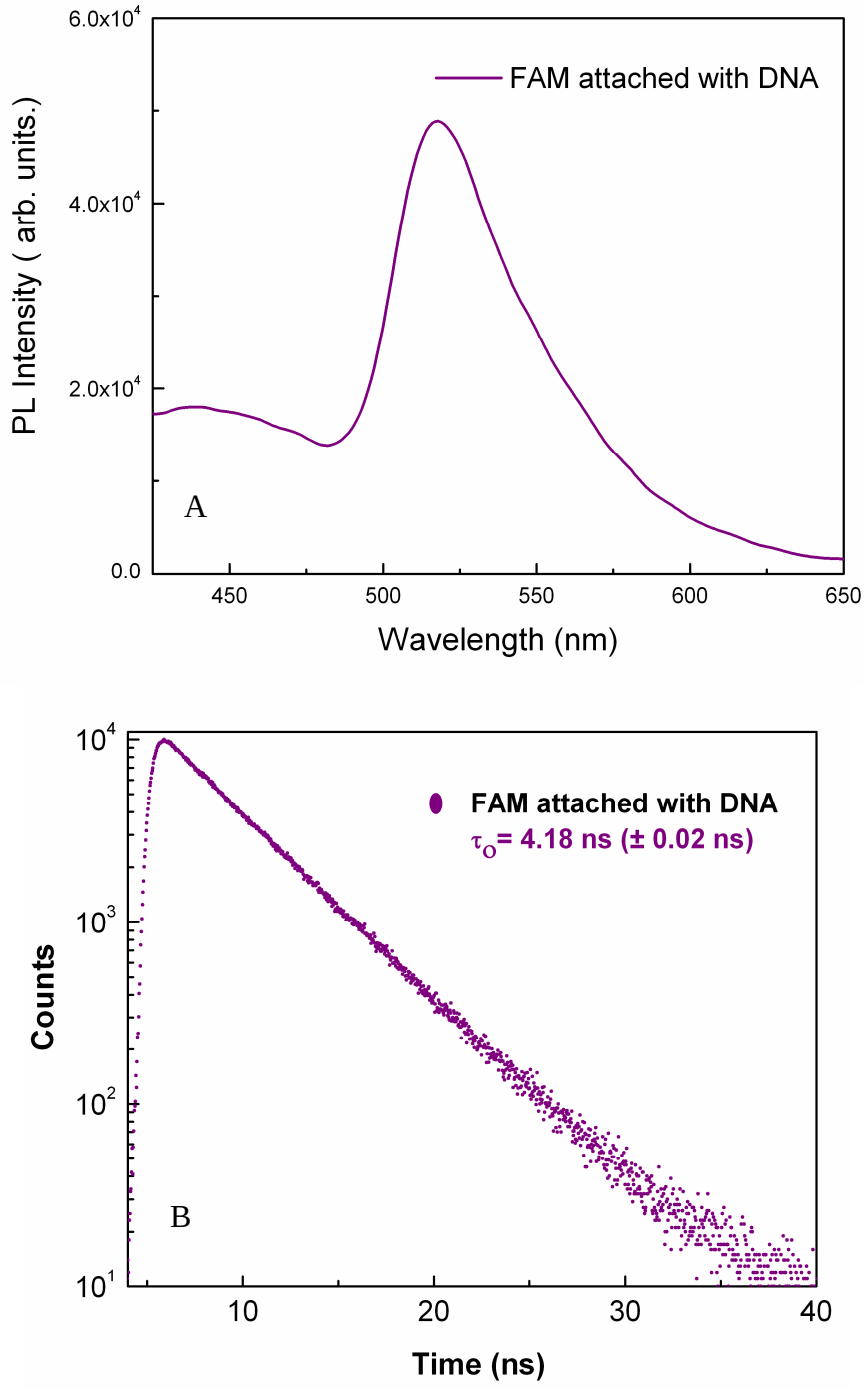

Figure 34: Steady-state PL spectrum of FAM conjugated with DNA showing the emission maximum at 518 nm (A). Time-resolved emission dynamics of FAM exhibiting a single exponential decay with lifetime of 4.18 ns (B).

Time-resolved fluorescence measurements were performed to investigate a distance-dependent quenching process between the donor FAM and the acceptor gold nanoparticles, separated by double stranded DNA with an increasing number of base pairs. Since the persistence length of double stranded DNA is about 50 nm (~ 150 bp) [27], short DNA strands can be considered as a rigid rod. The calculated separation distance assumes a linear DNA strand, with a C_6 spacer between the DNA and the donor and a C_3 spacer with thiol linkage connecting the acceptor gold nanoparticle to the DNA strand (**Figure 35**). The time-resolved fluorescence analysis of 16 bp exhibited a single exponential decay with a lifetime value of 3.13 ns (±0.04 ns). The measured lifetimes of 20 bp, 26 bp and 36 bp fragments were 3.16 ns (± 0.05 ns), 3.84 ns (± 0.04 ns), and 3.86 ns (± 0.03 ns), respectively (**Figure 36**).

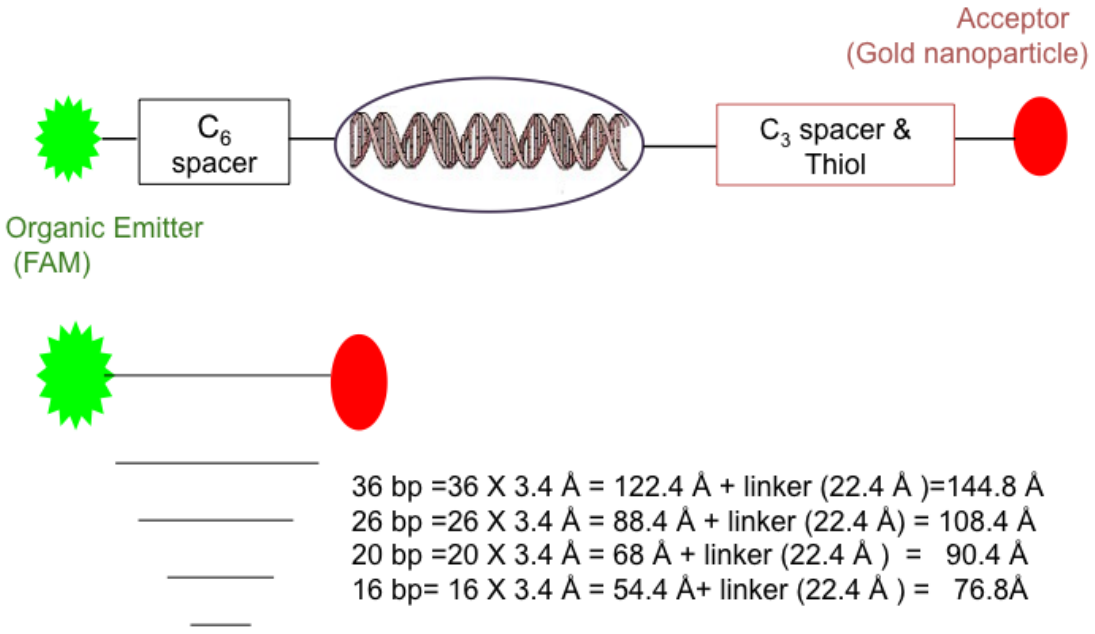

Figure 35: A schematic drawing of the system under investigation. A 1.4 nm gold nanoparticle and a FAM donor are attached to the two ends of a double stranded DNA via linkers. Four different lengths investigated in the present study are also indicated.

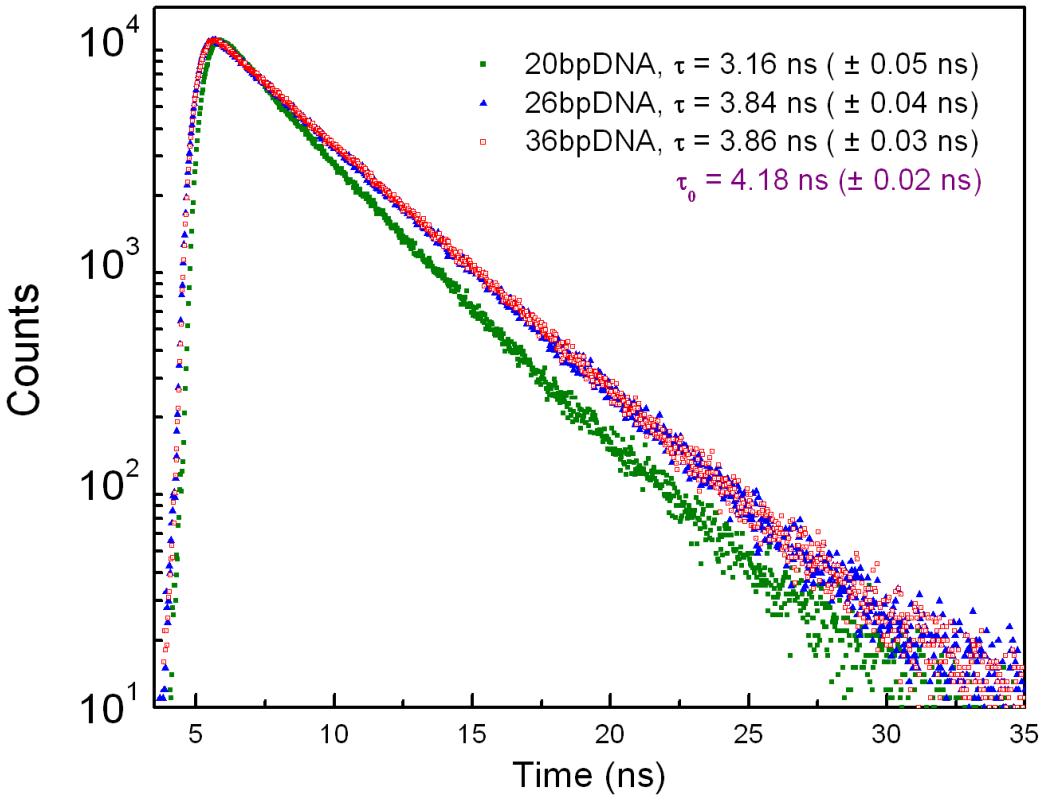

Figure 36: Results of time-resolved luminescence measurements indicating the change in lifetime observed for the three different distances studied (20 bp, 26 bp and 36 bp).

The quenching efficiencies (Q_{eff}) and energy transfer rates (k_{ET}) were calculated following equations (**Eq.16**) and (**Eq.17**), respectively, by comparing the measured lifetimes of the quenched fluorophore (τ') with the fluorophore's lifetime (τ_0) in the absence of gold nanoparticle in the identical DNA conjugated system.

$$Q_{eff} = 1 - \frac{\tau'}{\tau_0} \quad [16]$$

$$k_{ET} = \frac{1}{\tau'} - \frac{1}{\tau_0} \quad [17]$$

The quenching efficiency of the gold nanoparticle gradually decreased with an increase in the length of the DNA strands. Similarly, the nonradiative energy transfer rate followed a diminishing trend with increasing distance between the donor and acceptor. Our experimental outcomes supported the enhanced quenching ability of the gold nanoparticles at a longer distance compared to the traditional FRET process.

The interaction between metal nanoclusters and organic fluorophore varies with distance between the donor-acceptor pair. At a shorter distance (< 20 Å), radiative enhancement causes an increase of the spontaneous emission rate of donors that are placed in the proximity of metal nanostructures where the density of photonic states is higher than in a homogeneous medium [8,9]. Enhanced rates of the spontaneous emission can lead to the reduction of the excited-state lifetime of the emitter. At an intermediate distance (20-300Å), non-radiative energy loss of the donor is a predominant process [19, 20]. The non-radiative energy-transfer process varies as f/d^n, where f is the fluorophore's oscillator

strength, *d* is the distance between the donor and the metal surface, and *n* depends on geometric factors [1]. Recent theoretical studies have attempted to uncover the nonradiative energy transfer mechanism between metal nanoparticles and organic fluorophores [19-20, 22-25, 28]. The suggested explanations regarding the reported deviation of the energy transfer process between nanoparticles and organic donor from the conventional FRET process are attributed to the breakdown of point dipole approximations, insufficient orientation averaging during the lifetime of the donor, and excitation of electron-hole (e-h) pairs in the nanoparticles [22-25, 28]. Quantum mechanical studies predicted the rate of the energy transfer process from a fluorescent dye to a spherical nanoparticle might follow a variable distance dependence as $1/d^n$, with n =3,4 at intermediate distances, and Förster's $1/d^6$ dependence could be regarded at large separations between the donor and nanoparticles [23]. Additionally, the predicted energy transfer rate showed an asymptotic, nontrivial nanoparticle size dependence and the orientation factor varied from 1 to 4, contrasting with the traditional FRET process [23]. The use of a spherical jellium model to validate the rate of the non-radiative energy transfer process from the excited fluorescein to the gold nanoparticle has revealed that primary contributions to the energy transfer process originate from the d^{-6} term at the distances < 28 Å [28]. In addition, it has been suggested that the excitation of plasmons or electron-hole pairs of the nanoparticle are not sufficient to explain the energy transfer rate between the donor and nanoparticles at a longer distance [28]. A recent development of generalized Förster theory incorporating distance and torsional fluctuations pointed out that the deviation of the energy transfer process between metal nanoparticle and organic donor could originate from quantum mechanical modulations of donor-acceptor coupling

[13]. Considering n=4 for the dipole–metal surface energy transfer process, the characteristic distance (d_0) involving the nonradiative surface energy transfer (SET) between FAM and gold nanoparticle was estimated to be 76.3 Å [19,20], using the Persson and Lang's model [29]. However, the gold nanoparticle is assumed to be an infinitely wide plane of dipoles and the true n value could be slightly greater than 4 in respect of the dipole-surface energy transfer process [19,20]. Recent experimental studies on the surface energy transfer involving DNA conjugated fluorescent dyes and gold nanoparticle system analyzed the experimental results in the light of the Persson and Lang's model [29], supporting a $1/d^4$ distance dependence of the energy transfer process [19,20]. Additionally, salt concentration, length of linker molecules connecting the dye and DNA, and orientation of the fluorescent donor were found to be crucial players for the energy transfer process [30].

A comparison of quenching efficiencies obtained from our experimental results with a theoretical curve generated from the expression (**Eq. 18**) with d_o value of 70 Å indicated that the energy transfer process involving gold nanoparticle as quencher followed largely a $1/d^4$ distance dependence (**Figure 37**). The d_o value refers to the separation distance at which the donor will exhibit equal probabilities for energy transfer and spontaneous emission in the presence of an absorber (gold nanoparticles).

$$Q_{eff} = \frac{1}{1+\left(\frac{d}{d_0}\right)^n} \qquad [18]$$

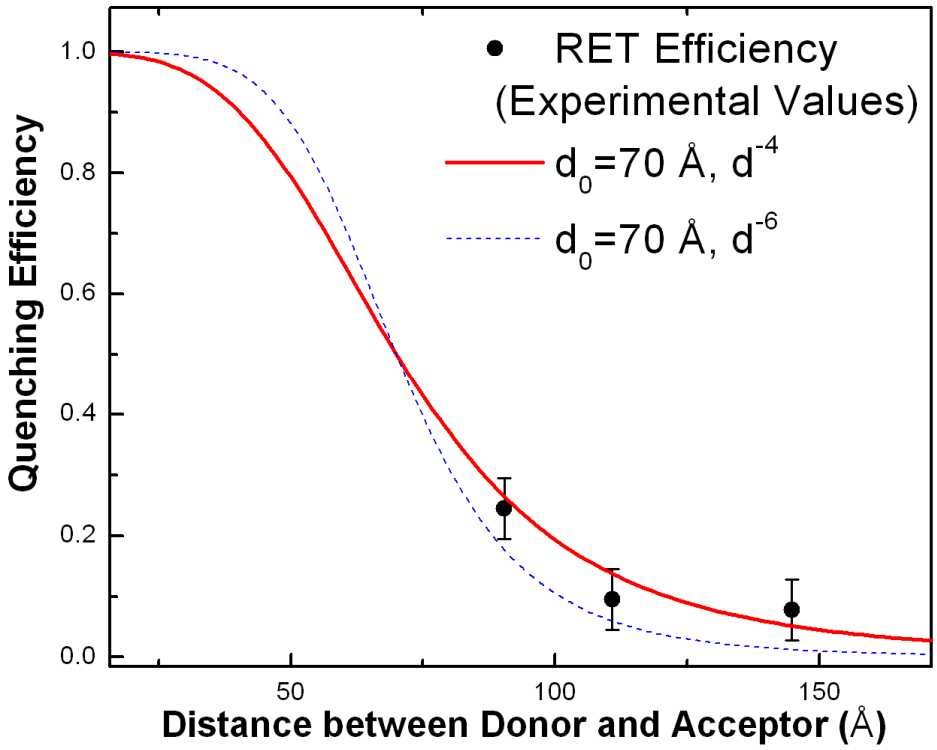

Figure 37: The quenching efficiency plotted as a function of distance for $1/d^4$ and $1/d^6$ models. At distances greater than 10 nm, the system shows quenching efficiencies closer to the $1/d^4$ model.

In summary, this investigation demonstrated the energy transfer between an organic donor and nanoparticle quencher separated by distances greater than the distance limits of the conventional FRET technique. Further experimental investigation at shorter separation distance between the donor fluorophore and nanoparticle is required to unravel the mechanistic details of the non-radiative energy transfer process involving metal nanoparticle quencher.

2.3. Structural study of Y-DNA using Time-resolved Fluorescence Spectroscopy

DNA, which has a toolbox of versatile physiochemical properties, can be used as a generic material to develop novel supramolecular structures because of its highly selective molecular recognition property [31, 32]. Y-shaped DNA (Y-DNA) can play a key role in the formation of unique assembled architectures [26]. For instance, dendrimer-like DNA (DL-DNA) structures were synthesized by assembling Y-DNA of varying lengths [26, 33]. DL-DNA has a promising role in the development of nano-barcode technology [34, 35], by functioning as a structural scaffolding as well as a structural probe involving multiplexed molecular sensing process [33]. Supramolecular assemblies of dendrimers can lead to the formation of multilayered gels and multimolecular megamers with complex architectural features [33]. DNA-based dendrimers are potentially beneficial to numerous *in vivo* applications such as drug and gene delivery, imaging, and tissue repair [36-37], because of their biocompatibility and chemical homogeneity of DL-dendrimers [34, 35, 38]. The ability to control the size, topology and ultimately the chemical properties of dendrimers relies on the structural stability of the building units [32]. Therefore, the physiochemical properties of Y-DNA can significantly affect the overall characteristics of the supramolecular structures. Y-DNA is composed of three entangled oligonucleotide components that are partially complementary to each other [26, 34]. The formation of Y-DNA has been achieved by stepwise as well as all-in-one (one pot) synthesis methods [26, 34]. The stepwise approach followed an initial hybridization of two oligonucleotides with partially complementary sequences, resulting in one arm of a Y-DNA; afterwards, the attachment

of a third oligonucleotide having the complementary base sequence to the first two unmatched portions of oligonucleotides, formed the other two arms of the Y-DNA. In the one-pot synthesis process, equal moles of all three oligonucleotides were mixed together to form the Y-DNA. Thus, designing appropriate base-sequences is imperative to construct a Y-DNA having a desired length [33-35]. The overall dimension and growth of an assembled structure critically depend on the conformational stability and structural flexibility of Y-DNA as a building block [32, 36, 37]. Hence, investigating the Y-DNA's structural properties in the solution state, which is the natural environment for organizing supramolecular architectures, is essential for the development of the self-assembly techniques using Y-DNA. In the present study, we used the time-resolved fluorescence resonance energy transfer (FRET) method to investigate the geometric dimension and structural stability of Y-DNA. As noted above, the FRET process involves a donor fluorophore in its excited state transferring energy by a nonradiative mechanism to an acceptor molecule placed in close proximity to the donor [1, 3, 9, 14]. Thus, FRET is not the result of a concentration-dependent re-absorption process involving intermediate photon transfer between a donor-acceptor pair [1,3]. Time-resolved analysis reveals molecular information, which, in general, is lost during time-averaging process [1,3,9,10,14]. Accordingly, unlike steady-state measurements, time-resolved experiments give information on the molecular shape and conformations of the donor molecules and the local distribution of the acceptor molecules around the donors [1,10]. A pair of fluorophore (Alexa 488) and black-hole quencher (Dabcyl) were successively positioned at two different ends of Y-DNA. The lifetime of the fluorophore was measured to observe the quenching effect of the absorber, reflecting the relative

distance between the donor and acceptor. In the FRET process, the donor and acceptor are coupled by a distance-dependent dipole-dipole interaction [1, 3]. The distance between the donor and acceptor and the extent of spectral overlap between them control the rate of energy transfer [1, 3]. Hence, time-dependent study of the emission lifetime of the fluorophore attached with Y-DNA is a unique means to shed light on the structural properties of the Y-DNA.

2.3.1. Experimental Method

Y-DNA consisted of three overlapping single oligonucleotide strands. Two of the oligonucleotides were either labeled with a fluorophore (Alexa 488, E_x= 495 nm and E_m =519 nm) or quencher. The fluorescent donor and acceptor were successively placed at two different ends of Y-DNA (**Figure 38**). Y-DNA was synthesized and purified following the methods described in the Refs.26 and 33 (All Y-DNA samples used in this study were obtained from Prof. Dan Luo's group at Cornell University). Y-DNA solutions (60 nM) were prepared using TE buffer (Sigma Cat# 93302) and the pH of the solutions was maintained at 7.5 for all steady-state and time-resolved fluorescence measurements. The time-resolved fluorescence measurements were carried out using a time correlated single photon counting (TCSPC) system (Horiba Jobin-Yvon). A 50 ps diode laser operating at 1 MHz repetition rate and 467 nm emission wavelength was used as the excitation source. The time-resolved data analysis with single exponential fitting model was performed with DAS6 software based on a deconvolution technique using the iterative nonlinear least-squares method [3, 17]. The steady-state fluorescence spectra were recorded using a spectrometer with a Xenon lamp as an excitation source at 357 nm.

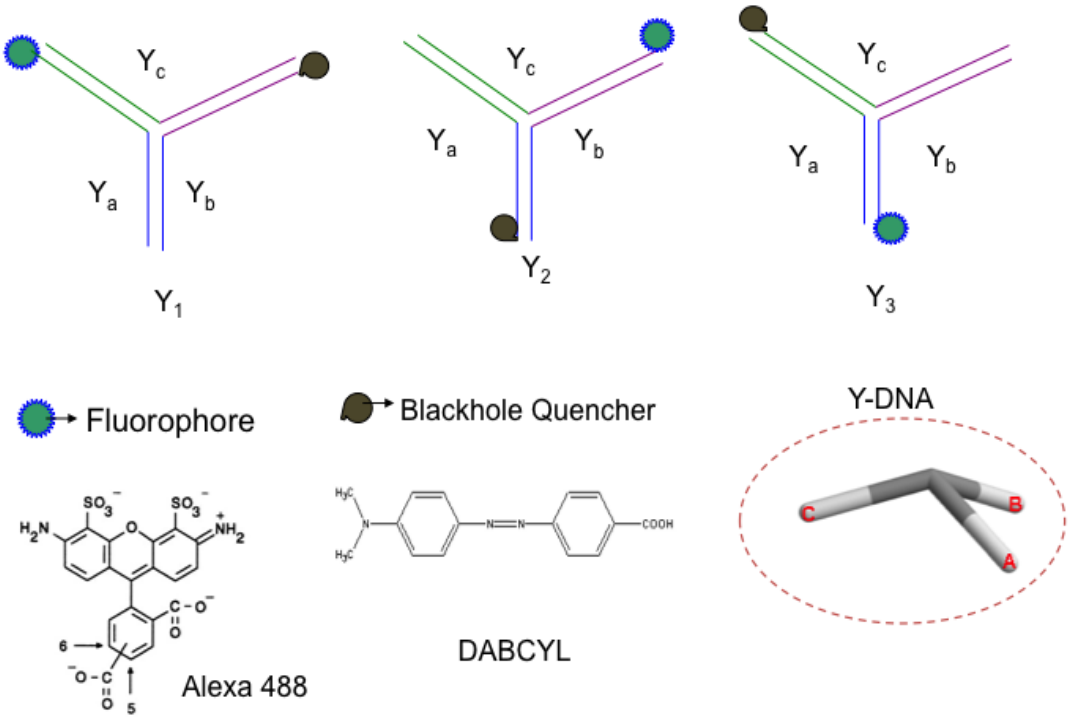

Figure 38: A schematic diagram of Y-DNA with the positions of the attached fluorophore (Alexa 488) and quencher (Dabcyl). Y_a, Y_b, and Y_c represent the distance between the donor and quencher.

2.3.2. Results and Discussion

Time-resolved measurements were performed on the DNA-conjugated fluorophore to examine any possible effect of the nucleic acid conjugation on the emission characteristics and fluorescence decay kinetics of the DNA-tagged Alexa 488. The steady-state photoluminescence study of Alexa 488 showed an emission maximum at 519 nm (**Figure 39**). The emission lifetime of Alexa 488 attached with Y-DNA was found to be 4.25 ns (± 0.02 ns) at the emission maximum (519 nm), following a single-exponential fluorescence decay model (**Figure 39**). These results confirmed that the fluorophore retained its original emission properties after conjugation with the Y-DNA.

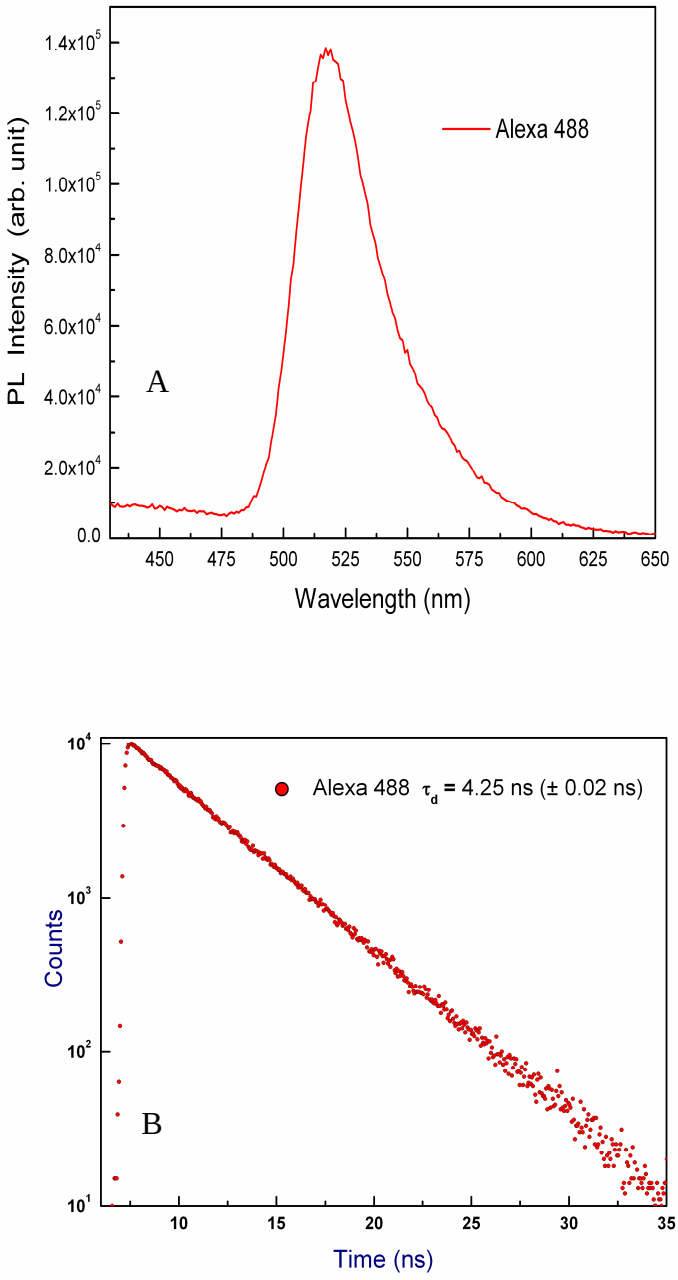

Figure 39: Steady-state photoluminescence spectrum of Alexa 488 conjugated with Y-DNA (A). Time-resolved luminescence study of Alexa 488 associated with Y-DNA (B).

Steady-state PL measurements showed differences in the emission intensity of Alexa 488 fluorophore associated with the Y-DNA systems (**Figure 40**).

The emission lifetimes of the Y-DNA conjugated fluorophore for Y_1, Y_2 and Y_3 were 3.99 ns (± 0.06 ns), 4.14 ns (± 0.04 ns), and 3.44 ns (± 0.21), respectively (**Figure 41**). The lifetime of Alexa 488 fluorophore that was placed successively at three ends of Y-DNA was reduced from the initial lifetime of the fluorophore in the absence of quencher.

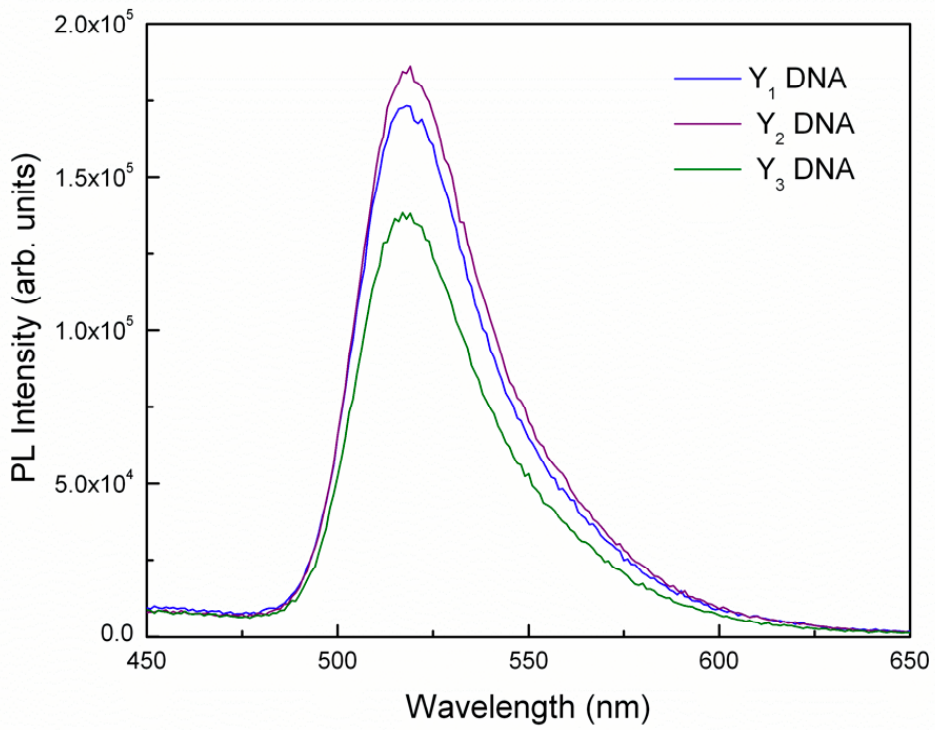

Figure 40: Steady-state emission spectra of Alexa 488 associated with Y_1, Y_2 and Y_3.

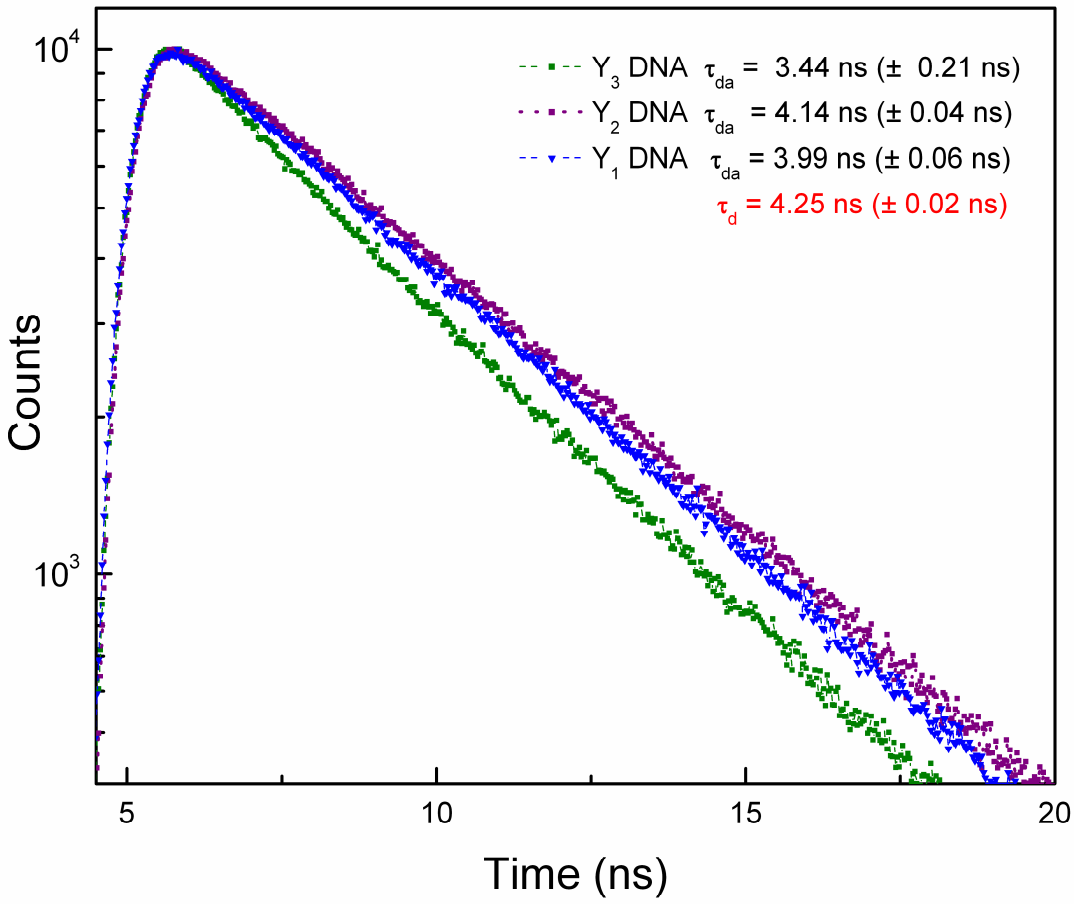

Figure 41: Time-resolved emission spectra of Alexa 488 associated with Y_1, Y_2 and Y_3 DNA systems, showing differences in lifetime of the fluorophore conjugated to the Y-DNA systems.

The distance between the donor and the quencher was computed using the following equations (19) and (20) [1, 3], where d_0 denotes the Förster radius (4.9 nm) for Alexa 488 and Dabcyl. The FRET efficiency (E) was estimated by comparing the quenched fluorophore's lifetime (τ_{da}) with the lifetime (τ_d) of fluorophore tagged with the Y-DNA in the absence of quencher (**Eq.19**).

$$E = \left(1 - \frac{\tau_{da}}{\tau_d}\right) \qquad [19]$$

$$d = d_o\left[\left(\left(\frac{1}{E}\right) - 1\right)^{\left(1/6\right)}\right] \qquad [20]$$

The differences in the lifetime reduction of the fluorophore suggested different distances between the donor and acceptor associated with particular Y-DNA arms [**Table 1**], since the lifetime reduction of the fluorophore depends on the proximity of the fluorophore to the quencher.

DNA	Lifetime (ns) of Alexa-488 (donor)	Distance between the donor and acceptor (nm)
Y_1	3.99 (± 0.06)	7.71 (± 0.11)
Y_2	4.14 (± 0. 0.04)	8.90 (± 0.08)
Y_3	3.44 (± 0.21)	6.23 (± 0.40)

Table 1: Distance between the donor and acceptor attached to Y-DNA arms.

The conformational stability of the Y-DNA system was examined by heating the Y-DNA samples to 40 ^{o}C, which is below the melting temperature of Y-DNA. After heating, the initial lifetime of the fluorophore changed and all three Y-DNA systems returned to their initial state upon lowering the temperature back to room temperature, exhibiting the respective initial lifetime of the donor (**Table 2**). After heating, Y_3 exhibited an increase in the fluorescence lifetime of the donor. Conversely, the lifetime of the fluorophore associated with Y_2 and Y_1 decreased due to heating.

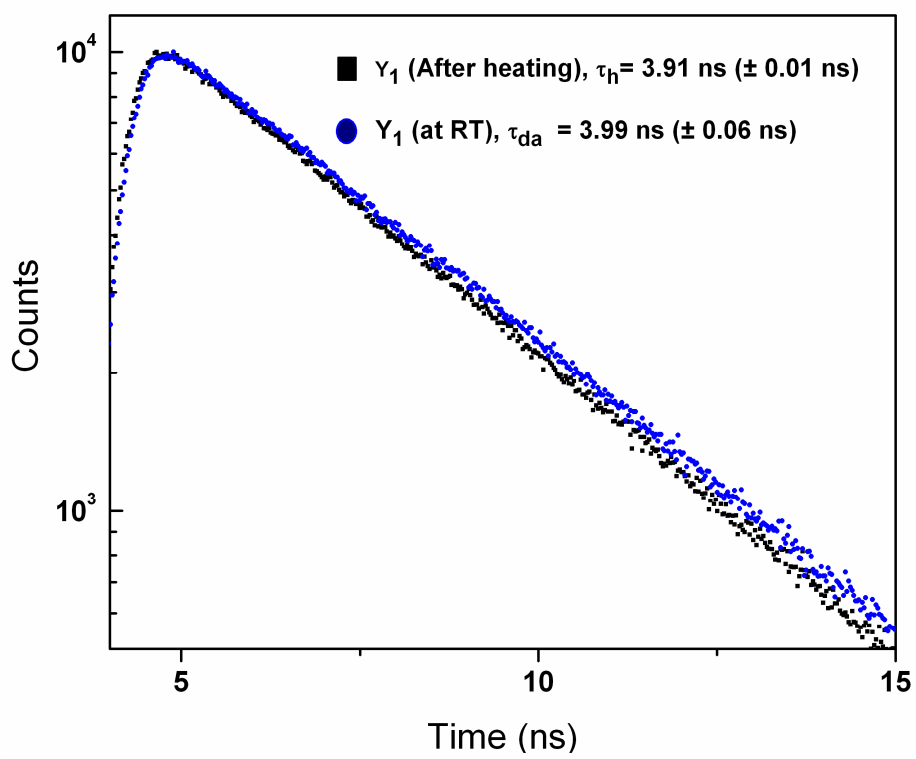

Figure 42:Time–resolved spectra of Alexa 488 showing the effect of heating on the emission dynamics of the flurophore conjugated with Y_1.

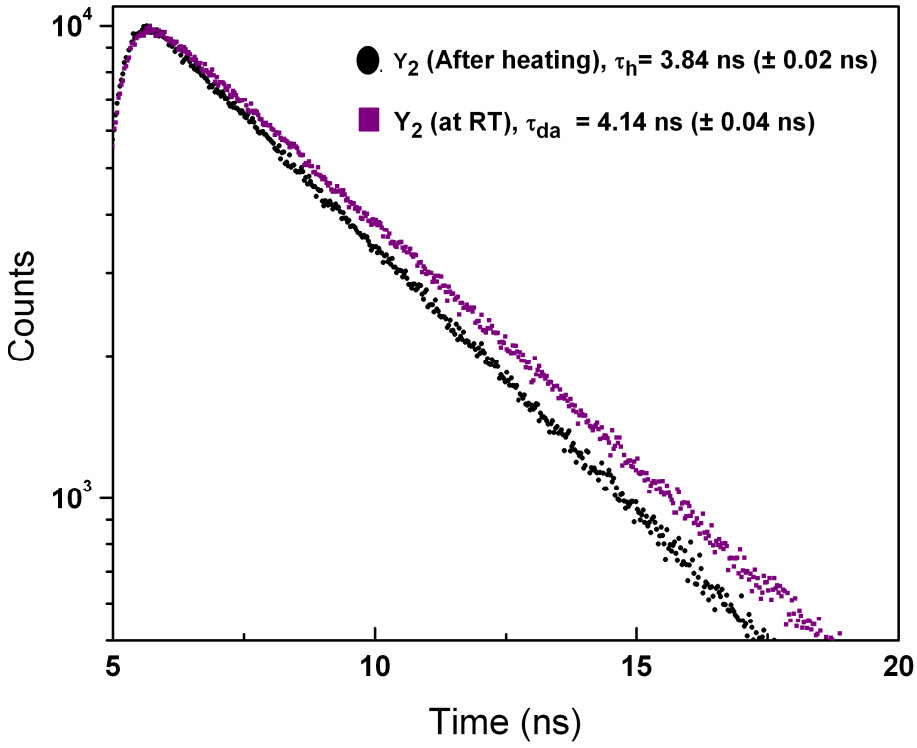

Figure 43:Time–resolved spectra of Alexa 488 showing the effect of heating on the emission dynamics of the flurophore conjugated with Y_2.

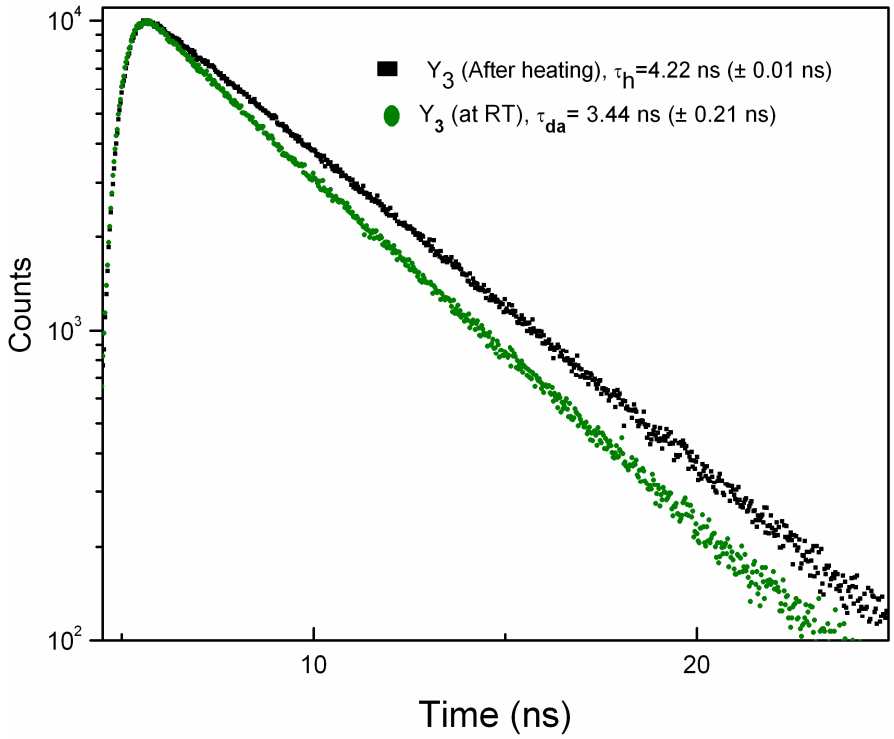

Figure 44:Time–resolved spectra of Alexa 488 showing the effect of heating on the emission dynamics of the flurophore conjugated with Y_3 .

DNA	Lifetime (ns) at room temperature	Lifetime (ns) after Heating to 40 ^{o}C
Y_1	3.99 (± 0.06)	3.91 (± 0.01)
Y_2	4.14 (± 0. 0.04)	3.84 (± 0.02)
Y_3	3.44 (± 0.21)	4.22 (± 0.01)

Table 2: Heating effect on lifetime of the Y-DNA conjugated with Alexa 488.

The response of Y-DNA to the temperature change suggested that the entangled Y-shaped nucleic acid system is rigid enough to maintain its original conformation. The conformational changes of Y-DNA due to heating brought the donor and acceptor, which were originally at a longer separation distance in Y_2 and Y_1, closer to each other (**Figure 45).** Conversely, the donor-acceptor distance in Y_3 increased because of heating (**Figure 45**). Based on these observations, it may be suggested that the arms of YDNA possibly underwent a concerted motion, in which two arms came closer to each other, keeping the third end farther from the other two ends. The TCSPC measurements provided an ensemble-averaged picture of the Y-DNA system, depicting the possible average structural behavior of the Y-DNA in the solution phase and supporting the structural rigidity of the Y-DNA system.

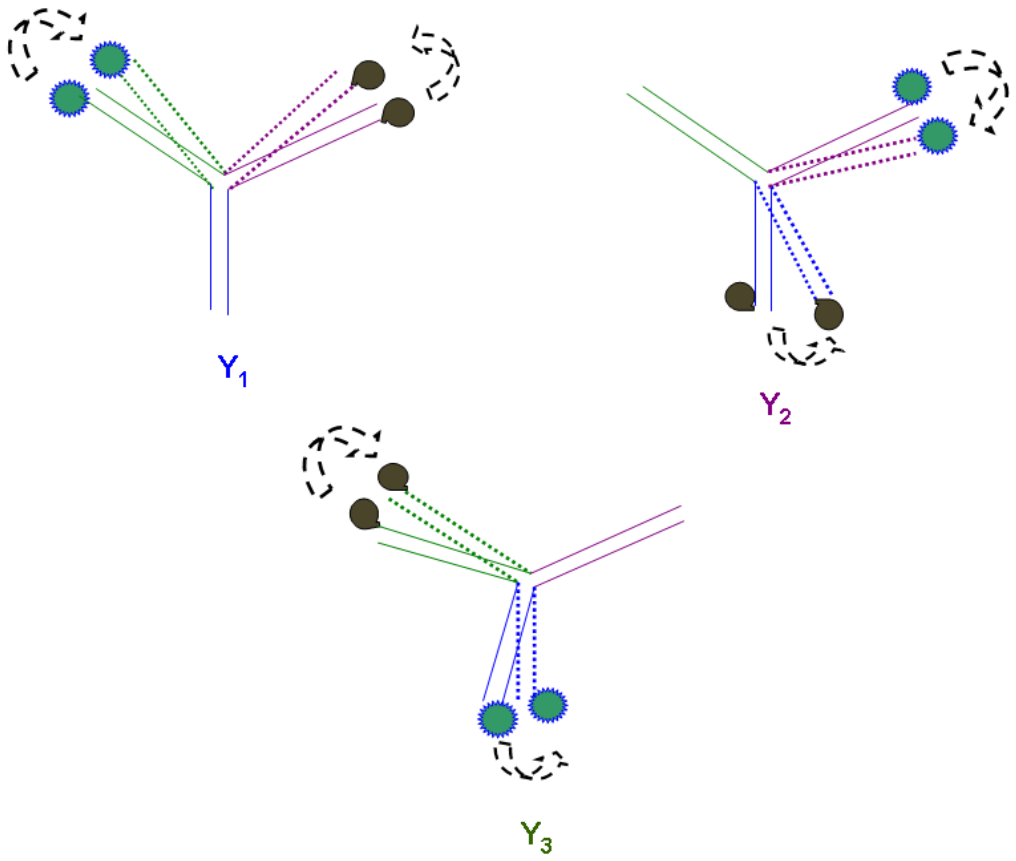

Figure 45: A schematic diagram describing the motion of Y-DNA arms upon heating. The changes in the relative position of the donor and acceptor are indicated by dashed arrows and dotted lines (---).

In summary, the time-dependent FRET analyses showed the different distances between the arms of Y-DNA and highlighted the overall structural rigidity of the Y-DNA system. These results can lead to further investigation of the structural and dynamical properties of Y-DNA systems by simultaneously studying time-dependent emission profiles of multiple fluorophores associated with the Y-DNA.

2.4. An investigation of steady-state and time-dependent luminescence properties of colloidal InGaP quantum dots

[Adapted from the published article in *Proceedings of MRS Fall Meeting* 2008, Symposium AA, 1133-AA07-18]

A quantum dot (QD), often described as an 'artificial atom', exhibits discrete energy levels with spacing that can be modulated precisely through the variation of their size [39]. Consequently, QDs act as robust light emitters with finely tunable fluorescence emission that offers a great advantage over conventional organic chromophores [40]. Nanoscopic size, stability in organic and aqueous phases, strong fluorescence, and a combination of large molar absorptivities and high quantum yields, are the unique properties that make QDs very attractive for biosensing and as fluorescent labels for biological research [40-43]. QDs show promising technological potential in the development of photonic transistors [44], photovoltaic devices [45], light-emitting diodes [46], and lasers [1]. Furthermore, QDs can serve as efficient fluorescent donors in the resonance energy transfer (RET) process [40, 47], a powerful tool for structural investigation of biological and synthetic macromolecules [1]. RET phenomena involving a pair of fluorescent donors and quenchers have been extensively utilized to investigate biomolecular conformational changes, which are imperative for understanding the structure-function characteristics of proteins [2] and nucleic acids [9, 48]. The long radiative lifetime of QDs (>10 ns) facilitates continuous and long-term tracking of slow biological processes and conformational dynamics of biomolecules with large distance changes, a challenging task with conventional organic fluorophores [40-42]. Indeed, the

applications of CdSe and CdS QDs have proven to be promising in this context [41, 42, 47, 48].

In the present study, we have investigated the steady-state and time-dependent optical properties of InGaP/ZnS core-shell QDs. These QDs can serve as an attractive, low toxicity alternative compared with the widely used semiconductor QDs, because they have no heavy metal components. Conventional cadmium- (Cd) and lead- (Pb) based semiconductor nanocrystals produce bio-hazardous wastes, specifically classified under the U.S. Restriction of Hazardous Substances Directive (RoHS). The use of II-VI and III-V semiconductor QDs (such as, CdTe, CdSe) as fluorescent labels presents a practical challenge in biological applications due to their intrinsic toxicity, owing to the presence of surface ions and the production of photo-initiated radicals [49]. Moreover, the long-term effects of toxic QDs in a biological system are not well understood. The use of InGaP QDs can provide an attractive biocompatible alternative for life science research, such as cell imaging, cell tracking, and cancer assays [40-43]. Since diverse experimental conditions can significantly affect the photo-physical properties of QDs [39, 41], a comprehensive understanding of their emission dynamics is essential [50]. Time-dependent analysis of the fluorescence emission of QDs reveals the status of their photo-excited states, which depend in turn on the confinement of electrons in a nearly defect-free three-dimensional crystal lattice as well as the surface conditions and local external environment of the QDs [50, 51]. In this study, we have investigated the time-resolved photoluminescence (PL) lifetime of InGaP/ZnS core/shell QDs, elucidating the emission dynamics that plays a key role in their application as fluorescent donors [40,42]. In addition, the change in the lifetime of InGaP/ZnS core/shell QDs was demonstrated in the

presence of an absorber molecule, validating the applicability of InGaP QDs to the RET process.

2.4.1. Experimental Methods

InGaP/ZnS core/shell QDs in toluene were obtained from Evident Technologies Inc. The size of the QD core is ~ 3.5 nm, and the diameter of the InGaP QD including its ZnS shell is approximately 6 nm [52]. The absorption spectrum of InGaP/ZnS core/shell QDs was measured using a Varian (CARY 5000) spectrometer. A continuous wave (CW) PL study of the QD solution was performed using an argon-ion laser with primary excitation wavelength of 488 nm as an excitation source, and the PL spectrum of the QDs was recorded using a fiber-coupled spectrometer (Ocean Optics HR4000).

We used a time-correlated single photon counting (TCSPC) system (Horiba Jobin-Yvon) to investigate the time-dependent optical properties of the QD emission. A 50 ps diode laser operating at 100 kHz repetition rate and 467 nm emission wavelength was used as the excitation source. To investigate the RET process between QDs and absorbers, the coordination compound Exciton ABS 642 (Exciton Inc.), was utilized as a quencher. Solutions of the QDs and the absorbers in toluene were prepared separately, maintaining an absorbance of 0.1 in their respective solutions. Subsequently, the absorber solution was added to the QDs to investigate the effect of the quencher on the fluorescence emission intensity and luminescence lifetime of the QDs. The resulting solution was found to be optically clear and homogeneous, and the final concentration of the QDs was maintained at an absorbance of ~ 0.05 for the time-dependent luminescence experiments.

2.4.2. Results and Discussion

The absorption spectrum of InGaP/ZnS core/shell QDs in toluene showed a clear excitonic absorption peak at 600 nm at room temperature (**Figure 46**), corresponding to the energy band gap (E_g) of ~ 2.06 eV. The absorption spectrum shows a second peak at ~ 500 nm due to absorption by excited states of the QD. The PL spectrum of the QDs showed a maximum at 650 nm with full width at half maximum of ~ 85 nm. The Stokes shift is found to be 50 nm (159 meV) for InGaP/ZnS core/shell QDs (**Figure 46**).

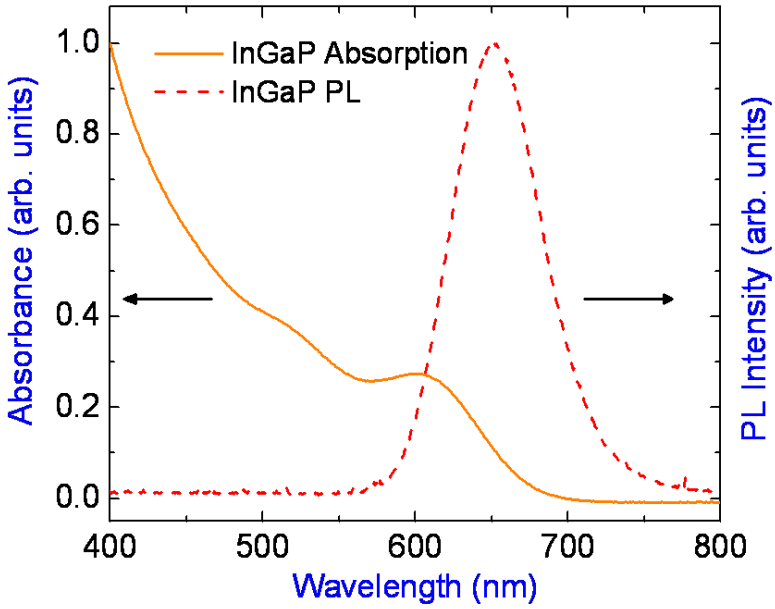

Figure 46: Optical absorption (solid line) and PL (dashed line) spectra of InGaP quantum dots.

Time-resolved PL study of QDs provides information on the kinetics of carrier relaxation [50, 53, 54, 55]. The PL decay of the QDs (**Figure 47**) at the emission maximum (650 nm) followed a bi-exponential model (τ_1= 47.1 ns (± 1.1ns), τ_2 = 142 ns (± 3.32 ns)). The steady state PL measurements (**Figure 46**) revealed a broad line-width (~ 85 nm), indicative of a large size-distribution in the QD ensemble. To verify this, we performed time-resolved PL measurements at emission wavelengths above (690 nm) and below (610 nm) the emission maximum (**Figure 47**). The emission at the shorter wavelength, 610 nm, corresponds to smaller QDs possessing greater carrier confinement, and hence a larger oscillator strength resulting in a faster radiative decay [56]. Experimentally, we observed the lifetimes at 610 nm to be τ_1= 36.5 ns (± 1.05 ns), τ_2= 111 ns (± 3.15 ns). Conversely, the emission at a longer wavelength is expected to have its major contribution from larger QDs that have smaller oscillator strength and thus a longer radiative lifetime [56]. We found the lifetimes of the QDs at 690 nm to be τ_1= 55.7 ns (± 0.26 ns), τ_2= 175 ns (± 0.82 ns).

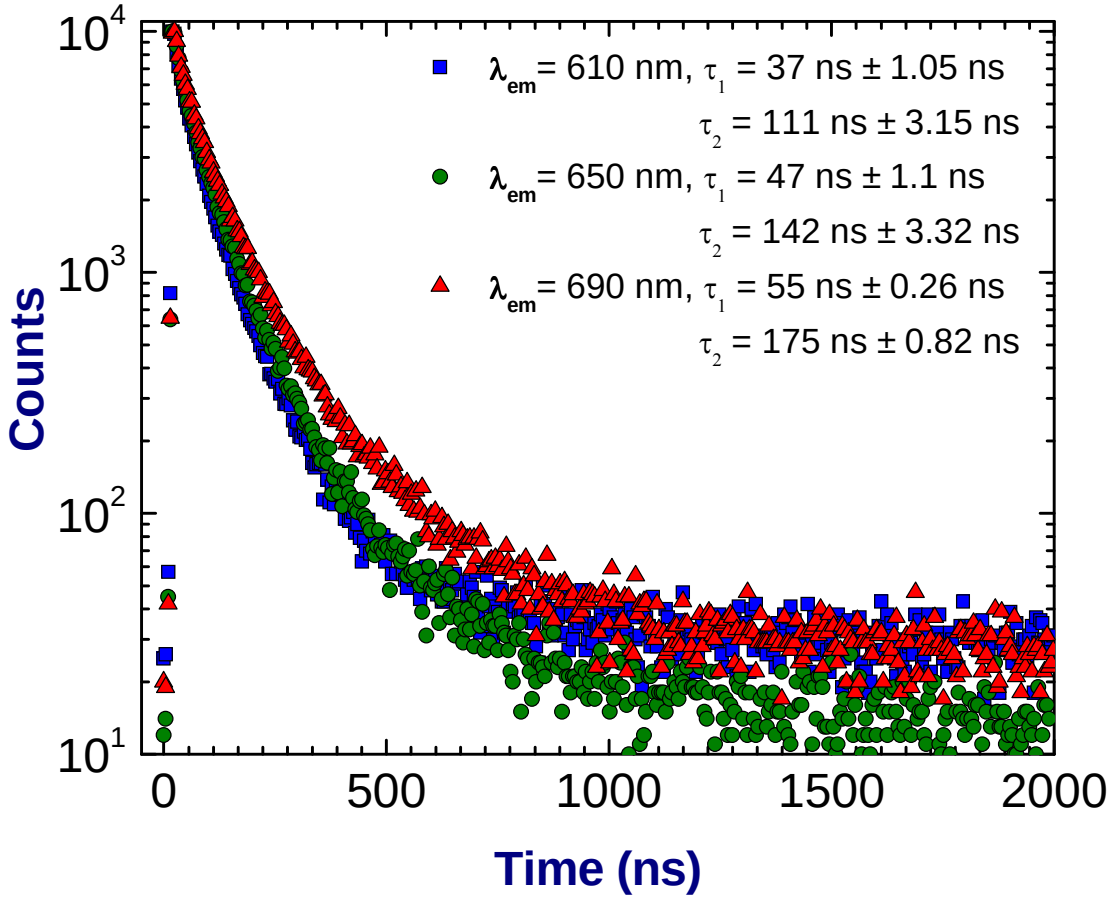

Figure 47: Time-resolved PL spectra of InGaP quantum dots at three different emission wavelengths 610 nm (blue squares),650 nm (green circles) and 690 nm (red triangle), corresponding to the wavelengths below and above the emission maximum of 650 nm.

Resonance energy transfer is an attractive optical method to probe distance-regulated and time-dependent biological events under both *in vivo* and *in vitro* conditions [1]. Real time spectroscopic ruler techniques, such as Förster resonance energy transfer (FRET), and surface energy transfer (SET), fundamentally rely on the RET principle which is based on the kinetics of the energy transfer process between a donor fluorophore and an acceptor molecule [41, 1, 9]. The efficiency of RET depends on the spectral overlap of a donor's luminescence with the absorption of a potential acceptor [1]. Considering the role of QD as a promising fluorescent donor, this study investigated the efficiency of the RET process between InGaP/ZnS core/shell QD and an absorber. Exciton ABS 642 exhibits an absorption peak at 650 nm and has considerable overlap with the fluorescence emission of InGaP QDs (**Figure 48**). Moreover, the absorber does not exhibit any fluorescence and scattering under the experimental conditions discussed here. In addition, the excitation source emits at 467 nm, which is far away from the absorption wavelength of the acceptor, minimizing the possibility of direct excitation of the acceptor molecule. Considerable quenching in the emission intensity of the InGaP/ZnS core/shell QDs was observed after mixing with Exciton ABS 642 (**Figure 49**). Additionally, no shift in the original emission wavelength of the QDs was observed, which affirmed that the absorber molecules did not perturb the native chemical environment of the InGaP/ZnS core/shell QDs. The reduction of the emission intensity of the InGaP/ZnS core/shell QDs can be attributed to the energy transfer process between the QD and the absorber. Since the spatial proximity of a quencher molecule provides a new decay channel to dissipate energy of the photo-excited QD [41, 1], the PL lifetime of the QD is expected to undergo an alteration due to the energy transfer process.

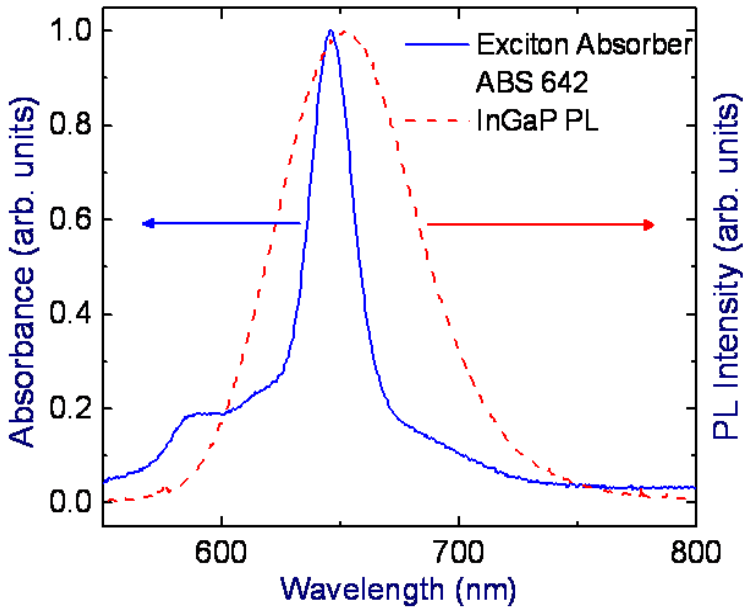

Figure 48: The absorption spectrum of the absorber ABS 642 showed a significant overlap with the photoluminescence spectrum of InGaP quantum dots at 650 nm.

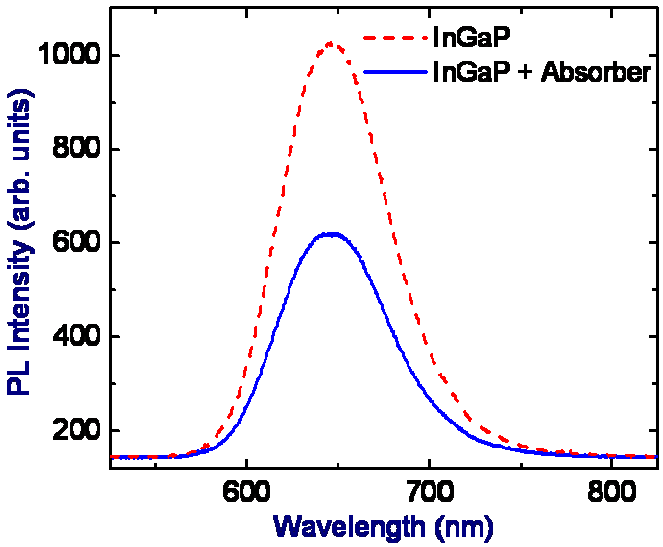

Figure 49: CW PL spectra exhibited the quenching of the InGaP QD luminescence. The emissions of the QD in the absence (dashed line) and in the presence (solid line) of the quencher (Exciton ABS 642) are shown.

The photoluminescence lifetime of InGaP/ZnS core/shell QDs was analyzed in the presence of the absorber to confirm this energy transfer process. The lifetime of the InGaP/ZnS core/shell QDs altered considerably in the presence of the absorbers (**Figure 50**) at the emission maximum of 650 nm. The reduction of the first QDs' lifetime, τ_1 (~ 36 % at 1:2 and 42 % at 1:5 QDs to absorber concentration ratio, respectively) in the presence of the absorber supports the inference that a RET process took place between the InGaP/ZnS core/shell QD and the absorber in the solution phase.

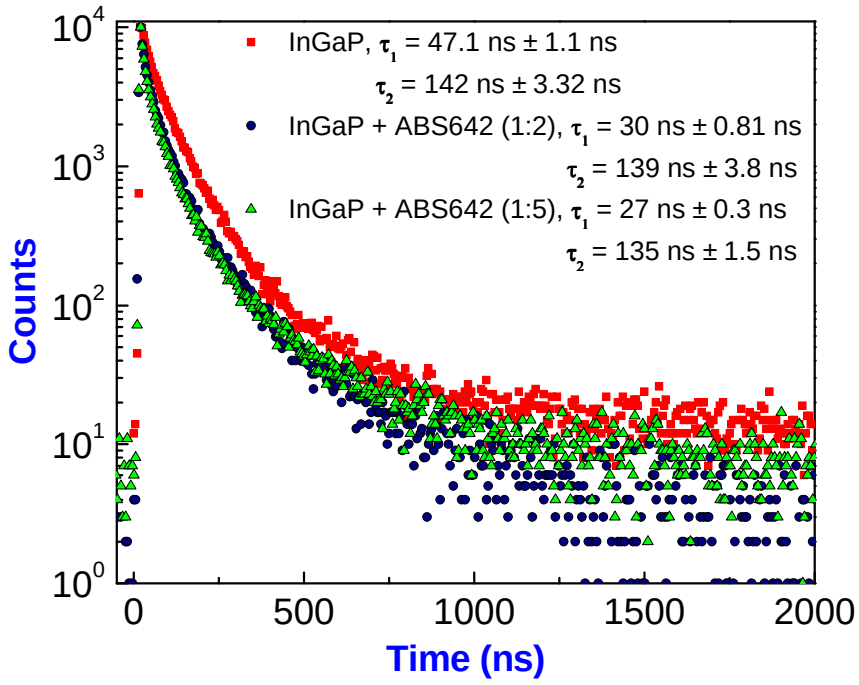

Figure 50: Time resolved photoluminescence spectra of InGaP quantum dots in the presence of the quencher, Exciton absorber ABS 642. Additionally, the decay of the InGaP quantum dots (filled squares) is presented. All spectra were recorded at 650 nm.

Although there is no covalent link between the donor QDs and the acceptor molecules in the current experiment, the evidence of RET between the InGaP QDs and the ABS 642 absorber molecules indicates spatial proximity between them. Based on the aforesaid observations, we anticipate that biocompatible InGaP QDs can be applied towards investigating biological processes entailing longer time and relatively large distance changes [9], which are currently out of reach of conventional organic fluorophores. By reducing the effects of background autofluorescence [42, 57], and enhancing the photostability of fluorescent labels, these QDs will help to elucidate relatively large (>10 nm) biomolecular conformational changes [47] such as DNA structural dynamics, protein folding, RNA folding, and oligomerization of membrane proteins [58, 59].

In summary, the absorption and PL emission studies reported here show that InGaP QDs with a moderate Stokes shift can be utilized as a promising fluorescent donor for spectroscopic ruler applications. The investigation of the PL lifetime of InGaP/ZnS core/shell QDs revealed fluorescence decay with a relatively longer lifetime compared with conventional bio-conjugating QDs (such as, CdSe, CdS). In addition, this study demonstrates the possibility of using these QDs as fluorescent donor in the RET mechanism. We anticipate the use of these less toxic InGaP colloidal QDs with longer luminescence lifetimes to further research in areas of biological imaging and biosensing.

2.5. References

1. Sapsford, K. E.; Berti, L.; Medintz, I. L., Materials for fluorescence resonance energy transfer analysis: Beyond traditional donor-acceptor combinations. *Angewandte Chemie-International Edition* **2006**, 45 (28), 4562-4588.

2. Royer, C. A., Probing protein folding and conformational transitions with fluorescence. *Chemical Reviews* **2006,***106* (5), 1769-1784.

3. Lakowicz, J. R., *Principles of Fluorescence Spectroscopy*. 3rd ed.; Plenum Publishing Corporation: **2006**.

4. Borland, L. M.; Kottegoda, S.; Phillips, K. S.; Allbritton, N. L., Chemical Analysis of Single Cells. *Annual Review of Analytical Chemistry* **2008,** *1* (1), 191-227.

5. Umezawa, Y., Optical Probes for Molecular Processes in Live Cells. *Annual Review of Analytical Chemistry* **2008,** *1*, 397-421.

6. Joo, C.; Balci, H.; Ishitsuka, Y.; Buranachai, C.; Ha, T., Advances in single-molecule fluorescence methods for molecular biology. *Annual Review of Biochemistry* **2008,** *77*, 51-76.

7. Weiss, S., Fluorescence spectroscopy of single biomolecules. *Science* **1999,***283* (5408), 1676-1683.

8. Ha,T., Single-Molecule FRET. *Single Molecules* **2001,***2* (4), 283-284.

9. Hess, S. T.; Huang, S. H.; Heikal, A. A.; Webb, W. W., Biological and chemical applications of fluorescence correlation spectroscopy: A review. *Biochemistry* **2002,** *41* (3), 697-705.

10. Xu, Q. H.; Gaylord, B. S.; Wang, S.; Bazan, G. C.; Moses, D.; Heeger, A. J., Time-resolved energy transfer in DNA sequence detection using water-soluble conjugated polymers: The role of electrostatic and hydrophobic interactions. *Proceedings of the National Academy of Sciences of the United States of America* **2004,** *101* (32), 11634-11639.

11. Szollosi, J.; Damjanovich, S.; Matyus, L., Application of fluorescence resonance energy transfer in the clinical laboratory: Routine and research. *Cytometry* **1998,** *34* (4), 159-179.

12. Patterson, G. H.; Piston, D. W.; Barisas, B. G., Forster distances between green fluorescent protein pairs. *Analytical Biochemistry* **2000,** *284* (2), 438-440.

13. Jang, S., Generalization of the Forster resonance energy transfer theory for quantum mechanical modulation of the donor-acceptor coupling. *J Chem Phys* **2007,** *127* (17), 174710.

14. Beechem, J. M.; Brand, L., Time-Resolved Fluorescence of Proteins. *Annual Review of Biochemistry* **1985,** *54*, 43-71.

15. Kapusta, P.; Wahl, M.; Benda, A.; Hof, M.; Enderlein, J., Fluorescence lifetime correlation spectroscopy. *Journal of Fluorescence* **2007,** *17* (1), 43-48.

16. Meseth, U.; Wohland, T.; Rigler, R.; Vogel, H., Resolution of fluorescence correlation measurements. *Biophysical Journal* **1999,** *76* (3), 1619-1631.

17. Enderlein, J.; Erdmann, R., Fast fitting of multi-exponential decay curves. *Optics Communications* **1997,***134* (1-6), 371-378.

18. Rosi, N. L.; Mirkin, C. A., Nanostructures in biodiagnostics. *Chemical Reviews* **2005,***105* (4), 1547-1562.

19. Yun, C. S.; Javier, A.; Jennings, T.; Fisher, M.; Hira, S.; Peterson, S.; Hopkins, B.; Reich, N. O.; Strouse, G. F., Nanometal surface energy transfer in optical rulers, breaking the FRET barrier. *Journal of the American Chemical Society* **2005,***127* (9), 3115-3119.

20. Jennings, T. L.; Singh, M. P.; Strouse, G. F., Fluorescent lifetime quenching near d=1.5 nm gold nanoparticles: Probing NSET validity. *Journal of the American Chemical Society* **2006,***128* (16), 5462-5467.

21. Kim, Y.-P.; Oh, Y.-H.; Oh, E.; Ko, S.; Han, M.-K.; Kim, H.-S., Energy Transfer-Based Multiplexed Assay of Proteases by Using Gold Nanoparticle and Quantum Dot Conjugates on a Surface. *Analytical Chemistry* **2008,***80* (12), 4634-4641.

22. Ray, P. C.; Darbha, G. K.; Ray, A.; Walker, J.; Hardy, W., Gold nanoparticle based FRET for DNA detection. *Plasmonics* **2007,** *2* (4), 173-183.

23. Bhowmick, S.; Saini, S.; Shenoy, V. B.; Bagchi, B., Resonance energy transfer from a fluorescent dye to a metal nanoparticle. *J Chem Phys* **2006,** *125* (18), 181102.

24. Saini, S.; Singh, H.; Bagchi, B., Fluorescence resonance energy transfer (FRET) in chemistry and biology: Non-Forster distance dependence of the FRET rate. *Journal of Chemical Sciences* **2006,***118* (1), 23-35.

25. Saini, S.; Srinivas, G.; Bagchi, B., Distance and Orientation Dependence of Excitation Energy Transfer: From Molecular Systems to Metal Nanoparticles. *Journal of Physical Chemistry B* **2009,***113* (7), 1817-1832.

26. Li, Y. G.; Tseng, Y. D.; Kwon, S. Y.; D'Espaux, L.; Bunch, J. S.; Mceuen, P. L.; Luo, D., Controlled assembly of dendrimer-like DNA. *Nature Materials* **2004,***3* (1), 38-42.

27. Lin, C. X.; Liu, Y.; Rinker, S.; Yan, H., DNA tile based self-assembly: Building complex nanoarchitectures. *Chemphyschem* **2006,** *7* (8), 1641-1647.

28. Swathi, R. S.; Sebastian, K. L., Resonance energy transfer from a fluorescent dye molecule to plasmon and electron-hole excitations of a metal nanoparticle. *J Chem Phys* **2007,***126* (23), 234701.

29. Persson, B. N. J.; Lang, N. D., Electron-Hole-Pair Quenching of Excited-States near a Metal. *Physical Review B* **1982,** *26* (10), 5409-5415.

30. Singh, M. P.; Jennings, T. L.; Strouse, G. F., Tracking Spatial Disorder in an Optical Ruler by Time-Resolved NSET. *Journal of Physical Chemistry B* **2009,***113* (2), 552-558.

31. Luo, D.; Saltzman, W. M., Synthetic DNA delivery systems. *Nature Biotechnology* **2000,** *18* (1), 33-37.

32. Seeman, N. C., Nucleic-Acid Junctions and Lattices. *Journal of Theoretical Biology* **1982,** *99* (2), 237-247.

33. Um, S. H.; Lee, J. B.; Park, N.; Kwon, S. Y.; Umbach, C. C.; Luo, D., Enzyme-catalysed assembly of DNA hydrogel. *Nature Materials* **2006,** *5* (10), 797-801.

34. Um, S. H.; Lee, J. B.; Kwon, S. Y.; Li, Y.; Luo, D., Dendrimer-like DNA-based fluorescence nanobarcodes. *Nature Protocols* **2006,** *1* (2), 995-1000.

35. Li, Y. G.; Cu, Y. T. H.; Luo, D., Multiplexed detection of pathogen DNA with DNA-based fluorescence nanobarcodes. *Nature Biotechnology* **2005,** *23* (7), 885-889.

36. Frechet, J. M. J., Dendrimers and supramolecular chemistry. *Proceedings of the National Academy of Sciences of the United States of America* **2002,** *99* (8), 4782-4787.

37. Lee, C. C.; MacKay, J. A.; Frechet, J. M. J.; Szoka, F. C., Designing dendrimers for biological applications. *Nature Biotechnology* **2005,** *23* (12), 1517-1526.

38. Freedman, K. O.; Lee, J.; Li, Y. G.; Luo, D.; Skobeleva, V. B.; Ke, P. C., Diffusion of single star-branched dendrimer-like DNA. *Journal of Physical Chemistry B* **2005,***109* (19), 9839-9842.

39. Klimov, V. I., Spectral and Dynamical Properties of Multiexcitons in Semiconductor Nanocrystals. *Annual Review of Physical Chemistry* **2007,***58* (1), 635-673.

40. Bailey, R. E.; Smith, A. M.; Nie, S. M., Quantum dots in biology and medicine. *Physica E-Low-Dimensional Systems & Nanostructures* **2004,** *25* (1), 1-12.

41. Parak, W. J.; Gerion, D.; Pellegrino, T.; Zanchet, D.; Micheel, C.; Williams, S. C.; Boudreau, R.; Le Gros, M. A.; Larabell, C. A.; Alivisatos, A. P., Biological applications of colloidal nanocrystals. *Nanotechnology* **2003,** *14* (7), R15-R27.

42. Michalet, X.; Pinaud, F. F.; Bentolila, L. A.; Tsay, J. M.; Doose, S.; Li, J. J.; Sundaresan, G.; Wu, A. M.; Gambhir, S. S.; Weiss, S., Quantum dots for live cells, in vivo imaging, and diagnostics. *Science* **2005,***307* (5709), 538-544.

43. Chan, W. C.; nbsp; W.; Nie, S., Quantum Dot Bioconjugates for Ultrasensitive Nonisotopic Detection. *Science* **1998,***281* (5385), 2016-2018.

44. Klein, D. L.; Roth, R.; Lim, A. K. L.; Alivisatos, A. P.; McEuen, P. L., A single-electron transistor made from a cadmium selenide nanocrystal. *Nature* **1997,***389* (6652), 699-701.

45. Greenham, N. C.; Peng, X. G.; Alivisatos, A. P., Charge separation and transport in conjugated-polymer/semiconductor-nanocrystal composites studied by photoluminescence quenching and photoconductivity. *Physical Review B* **1996,***54* (24), 17628-17637.

46. Park, N. M.; Kim, T. S.; Park, S. J., Band gap engineering of amorphous silicon quantum dots for light-emitting diodes. *Applied Physics Letters* **2001,***78* (17), 2575-2577.

47. Lu, H.; Schops, O.; Woggon, U.; Niemeyer, C. M., Self-assembled donor comprising quantum dots and fluorescent proteins for long-range fluorescence resonance energy transfer. *Journal of the American Chemical Society* **2008,***130* (14), 4815-4827.

48. Gill, R.; Willner, I.; Shweky, I.; Banin, U., Fluorescence resonance energy transfer in CdSe/ZnS-DNA conjugates: Probing hybridization and DNA cleavage. *Journal of Physical Chemistry B* **2005,***109* (49), 23715-23719.

49. Viktoriya Sokolova; Matthias Epple, Inorganic Nanoparticles as Carriers of Nucleic Acids into Cells. *Angewandte Chemie International Edition* **2008,***47* (8), 1382-1395.

50. Schlegel, G.; Bohnenberger, J.; Potapova, I.; Mews, A., Fluorescence decay time of single semiconductor nanocrystals. *Physical Review Letters* **2002,***88* (13), 137401.

51. Fisher, B. R.; Eisler, H. J.; Stott, N. E.; Bawendi, M. G., Emission intensity dependence and single-exponential behavior in single colloidal quantum dot fluorescence lifetimes. *Journal of Physical Chemistry B* **2004,***108* (1), 143-148.

52. Private communication with Evident Technology Inc.

53. Pons, T.; Medintz, I. L.; Sykora, M.; Mattoussi, H., Spectrally resolved energy transfer using quantum dot donors: Ensemble and single-molecule photoluminescence studies. *Physical Review B* **2006,***73* (24), 245302.

54. Bawendi, M. G.; Carroll, P. J.; Wilson, W. L.; Brus, L. E., Luminescence Properties of Cdse Quantum Crystallites - Resonance between Interior and Surface Localized States. *Journal of Chemical Physics* **1992,***96* (2), 946-954.

55. Crooker, S. A.; Barrick, T.; Hollingsworth, J. A.; Klimov, V. I., Multiple temperature regimes of radiative decay in CdSe nanocrystal quantum dots: Intrinsic limits to the dark-exciton lifetime. *Applied Physics Letters* **2003,***82* (17), 2793-2795.

56. Hours, J.; Senellart, P.; Peter, E.; Cavanna, A.; Bloch, J., Exciton radiative lifetime controlled by the lateral confinement energy in a single quantum dot. *Physical Review B* **2005,***71* (16), 161306(R).

57. Alivisatos, P., The use of nanocrystals in biological detection. *Nature Biotechnology* **2004,***22* (1), 47-52.

58. Lim, T. C.; Bailey, V. J.; Ho, Y. P.; Wang, T. H., Intercalating dye as an acceptor in quantum-dot-mediated FRET. *Nanotechnology* **2008,***19* (7), 075701.

59. Rasnik, I.; Mckinney, S. A.; Ha, T., Surfaces and orientations: Much to FRET about? *Accounts of Chemical Research* **2005,***38* (7), 542-548.

3.1. Introduction

Biopolymers are associated with a wide variety of functions depending on their physiochemical properties. Biological macromolecules (protein, nucleic acids) meet the same nanometer length scale of inorganic nanostructures [1]. Hence, nanostructures associated with biomaterials have a wide range of applications toward the development of integrated mechanical, optical and electronic devices, sophisticated catalysts and novel biosensing devices [1-6]. Nucleic acid is an exclusive polymer that regulates the genetic bases of living organisms. Nucleic acid can also function as a unique building block of novel supramolecular architectures. DNA plays a leading role in the development of various novel nanostructures and nanoscale devices, specifically, biosensors [1-6]. The highly specific molecular recognition property and the characteristic double helix structure of DNA originate from the selective base pairing between two complementary single strands [1, 4, 5]. The design of a DNA sensing device relies on the specific molecular recognition property and selective hybridization process of the DNA [1,4], involving the selective binding of a single strand (ss) DNA (target sequence) to its complementary strand (probe sequence) under physiological conditions [1,4,7]. ssDNA exhibits considerable differences in electrostatic properties and conformational flexibility from its double stranded (ds) form, and therefore a theoretical understanding of the structural differences in the nucleic acid system (from ssDNA to dsDNA) is essential for the development of DNA-based sensing devices. Molecular dynamics (MD) simulation is, in essence, a single molecule “in silico” experiment [9], which provides an atomistic description of a biopolymeric system. Therefore, MD simulation is a suitable way to explore the structural and dynamical properties of the ssDNA.

Globular proteins such as BSA (Bovine serum albumin) play an imperative role in synthesizing novel bio-conjugated nanoarchitectures in an aqueous medium. Steric effect, spatial orientations and noncovalent interaction of the associated biomolecules control the growth and assembly of the nanostructures [1, 6]. In addition, the conjugation of nanomaterials significantly affects the structural properties of the associated proteins or linker biomolecules [1,6,7].

Lipids are naturally occurring surfactants with a wide variety of polar head groups and non-polar organic tails, and possess a very selective self-assembly property. Therefore, lipid acts as a building unit of biological membrane protecting the cellular components. The combination of polar and non-polar components in a lipid system causes a special structural heterogeneity, which can lead to the formation of novel organic-inorganic hybrid structures upon conjugation with nanomaterials in an organic medium [1,6].

3.2. Molecular dynamics simulations of a single stranded (ss) DNA

[Adapted from the published article in *Molecular Simulation* 2007, 33(6-8), 573-576.]

In recent years, the specific and selective hybridization of nucleic acids have been utilized widely for the development of novel nanostructures, including nanoelectronics, nanomechanics and biosensing devices [1-2]. The specific molecular recognition property and hybridization phenomenon of DNA significantly control the sensitivity and selectivity of DNA based biosensors [2-4]. DNA possesses a polyanionic backbone, composed of alternating sugar and phosphate groups, and has four different bases, namely, Adenine (A), Guanine (G), Cytosine (C) and Thymine (T) [3]. The specific molecular recognition property of DNA originates from the selective base pairing: A binds to T and C binds to G [3, 4]. Apart from this distinctly characteristic base-pairing property, the polyanionic backbone controls the physiochemical properties of DNA such as flexibility, electrostatic properties, and binding capacity to cationic nanoparticulates [5, 6]. DNA based biosensors fundamentally rely on the hybridization phenomenon, in which a single strand (ss) DNA binds selectively to its complementary strand under ambient conditions [2, 7]. As a result of the exposed bases and the lack of a comparatively rigid double helix structure, ssDNA demonstrates considerable differences in electrostatic properties and flexibility compared with double strand (ds) DNA [3, 7]. Consequently, the ssDNA plays a significant role in the hybridization process, as well as in the proper functioning of these nanostructure devices [2, 3, 7].

In view of the fact that the biosensing devices primarily use short DNA strands, this study focused on the 130-145 codon (15 codon) sequence of the p53 gene, which is involved in

tumor suppression [8], and a mutation in this codon sequence of p53 can cause cancer, in particular, lung cancer. The specific objective of this study was to theoretically understand the conformational characteristics of short single strand of nucleic acids under various thermodynamic conditions. Accordingly, an understanding of the behavior of short strands of the DNA system can be employed to improve the hybridization process, associated with the characteristic role of the biosensing devices. Molecular Dynamics (MD) Simulations of the ssDNA were performed for this theoretical investigation.

3.2.1. Simulation Method

MD simulations can delineate the atomistic details of the DNA system because they compute atomic trajectories by solving equations of motion using empirical force fields that describe the actual atomic force in biomolecular systems [9]. The simulation was carried out by the NAMD molecular dynamics program [10], which uses a potential energy function that considers various bonding and nonbonding energy contributions, including bond stretching, bending, and torsional bonded interactions [10]. The force field is the mathematical description of the potential which atoms in the system experience. In this study, the AMBER force field was utilized, as it is widely applied to describe nucleic acid system [11].

AMBER force field is described below (**Eq.21**).

$$V = \frac{1}{2}\sum_{bonds}\left(K_b\left(b-b_0\right)^2\right)+\frac{1}{2}\sum_{angles}\left(K_\theta\left(\theta-\theta_0\right)^2\right)+\frac{1}{2}\sum_{dihedrals}\left(K_\phi\left(1+\cos\left[n\varphi-\gamma\right]\right)\right)$$
$$+\sum_{nonbonded}\left[\frac{A}{r^{12}}-\frac{B}{r^6}\right]+\sum_{nonbonded}\frac{q_1q_2}{\varepsilon r} \qquad [21]$$

The first, second, and third terms in the function (V) describe bond stretching, bending, and torsional energy, respectively. The fourth term depicts non-bonded interaction; the fifth term describes electrostatic energy. In the force field, chemical bonds are represented by harmonic potentials, which assume that bonds cannot be ruptured. This description of the bonds is only realistic close to the equilibrium distance. The bond force constants, estimated from spectroscopic methods or quantum mechanical calculations, determine the flexibility of a bond. Similarly, a harmonic potential describes the energy related to the alterations of bond angles, given by the second term in the AMBER force field. The rotational bond energies are depicted by the torsion angle potential functions, modeled by a periodic function and sum of cosine terms of angles. The potential functions representing nonbonded interactions are comprised of van der Waals and electrostatic forces. The long-range electrostatic interaction is a very important and challenging issue to address in obtaining a valid result in a biomolecular simulation [10, 12]. Since the Ewald method is very reliable for estimating electrostatic interactions in a spatially limited system, the particle–mesh Ewald (PME) method was

adopted for a faster numerical computation of the electrostatic interaction in this study [10].

The MD simulation was carried out in the presence of explicit solvent molecules and Na^+ counterions. The periodic boundary condition was employed to perform the simulation. A TIP3P water model in a simulation box was used for solvating the DNA system [11]. The structural parameters and coordinates necessary for the ssDNA system were obtained by taking into consideration a helix from double stranded B-DNA designed by the AMBER program with the above-mentioned p53 sequence (130 -140 codon sequence) [11]. A single DNA strand containing 12 bases was prepared for this molecular dynamics study.

Energy minimization of the ssDNA and equilibration of the system at particular thermodynamic conditions are the two initial important steps to undertake a valid molecular dynamics study [9, 12]. The potential energy of the solvated ssDNA was minimized for 2000 steps to get the energy-minimized structure of ssDNA. The energy-minimization was done by application of the conjugate gradient method in the NAMD program [10]. Thereafter, the energy-minimized structure of the ssDNA was equilibrated while maintaining proper thermodynamic conditions of the ensemble of interest. The equilibration was performed for microcanonical (NVE), canonical (NVT), and isobaric-isothermal (NPT) ensembles. The temperature was maintained at 300 K for all ensembles. The pressure was maintained at 101325 Pa (1 atm) in the NPT ensemble. The consistency of temperature was maintained by performing Langevin Dynamics [9, 10]. The constant pressure control was executed by the Langevin piston Nose-Hoover

method, available in the NAMD program [10]. VMD, a molecular viewing program, was used to visualize the dynamics of the system [13]. The achievement of the dynamic equilibrium of the system was evaluated by how well energy, pressure, and temperature (thermodynamic properties of the system) were distributed in the system over a certain amount of time [9, 12].

3.2.2. Results and Discussion

Thermodynamic observables (pressure, temperature, and volume) play an important role in setting up the proper ensemble for the simulation study [10, 14]. The distribution of energy (kinetic and potential energy) indicates the establishment of dynamic thermodynamic equilibrium. Since the force field in the MD simulations assumes that the bonded interactions (bonds, angles and dihedrals) maintain the characteristics of harmonic oscillators [9, 10], fluctuations in kinetic energy, and hence the temperature distribution can be attributed to the equilibrium of the ssDNA system. The simulation was carried out in the microcanonical ensemble (constant N (number of atoms), V (volume), and E (energy). The dynamics of system was observed for 100 ps after initial equilibration of 50 ps. The initial equilibration was performed at the constant temperature of 300 K. The fluctuation in temperature during the dynamics study maintained the Gaussian distribution with a mean temperature of 303.99 K (**Figure 51**). The fluctuations in the temperature describe the effect of the finiteness of the system.

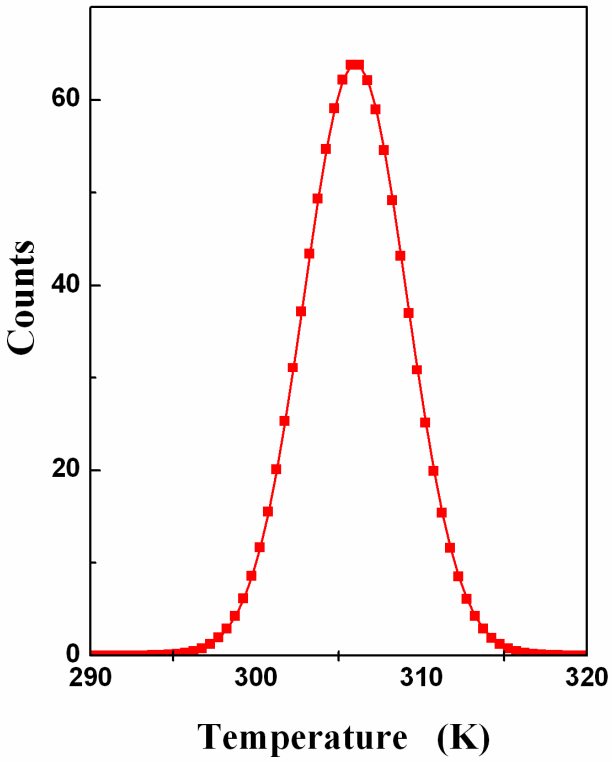

Figure 51: Temperature fluctuation observed in NVE ensemble of ssDNA.

As the system reaches dynamic equilibrium, the total energy of the system approaches a constant value. The fluctuations in the total energy of the system depend on the number of atoms or particles present in the simulating system. The average kinetic energy resulted in the temperature of the solvated ssDNA system. The distribution of the kinetic energy of the ssDNA system confirms the establishment of physiological temperature.

The kinetic energy distribution of solvated ssDNA system was computed by running the dynamics for 100 ps in the canonical (NVT) ensemble. The distribution of kinetic energy of the ssDNA system followed the Maxwell-Boltzmann distribution with the standard deviation of 0.602 Kcal/mole, which corresponded to a temperature of approximately 300 K (**Figure 52**). Thus, the desired equilibrium state was achieved by performing the proper sampling of the ssDNA configurations.

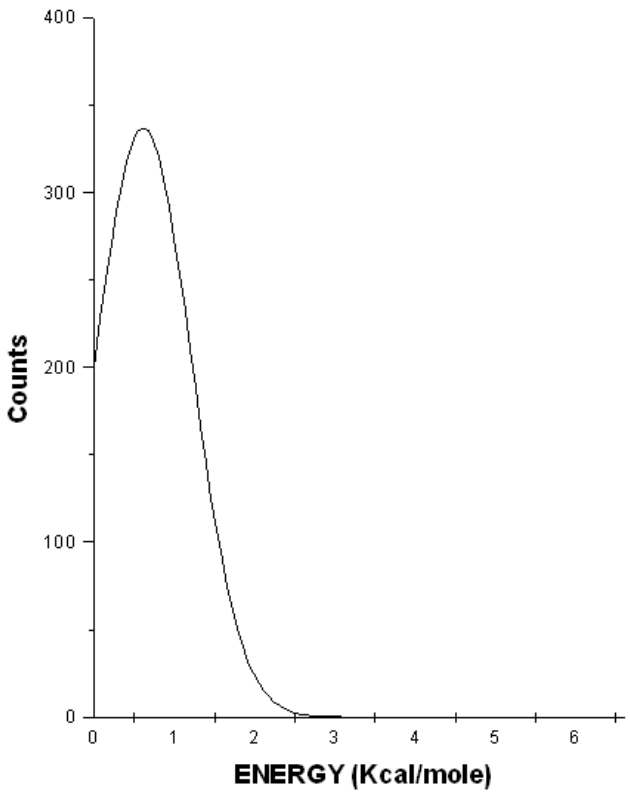

Figure 52: The distribution of kinetic energy of ss DNA system in NVT ensemble.

The Root Mean Square Deviation (RMSD) of the ssDNA backbone was computed for NVT and NPT ensembles (**Figure 53-54**). The RMSD provides the numerical measure of the difference between two structural states of the ssDNA [15, 16]. The conformational stability of the ssDNA plays a significant role in maintaining a proper equilibrium state. The RMSD of the nucleic acid backbone shows the conformational state of the ssDNA with the progress of the dynamics [15, 16]. As the RMSD of the nucleic acid strand changes over time, it provides an indication of the stability of the ssDNA at the specific state of equilibrium.

For the NVT ensemble study, at first the ssDNA system was equilibrated for 50 ps at 300 K. The achievement of the dynamic equilibrium state was evaluated by examining the consistency in the total energy, temperature and volume. Thereafter, the dynamics of the system was studied for 50 ps. The RMSD of the nucleic acid backbone was calculated during this dynamics study to investigate the conformational change of the ssDNA from its apparent equilibrium structure. The RMSD of the ssDNA exhibited an approximately flattening curve (**Figure 53**) with the deviation of approximately 1.4 to 1.6 $\mathring{A}$. This result shows a stable conformational state of the ssDNA under the prevailing thermodynamic conditions.

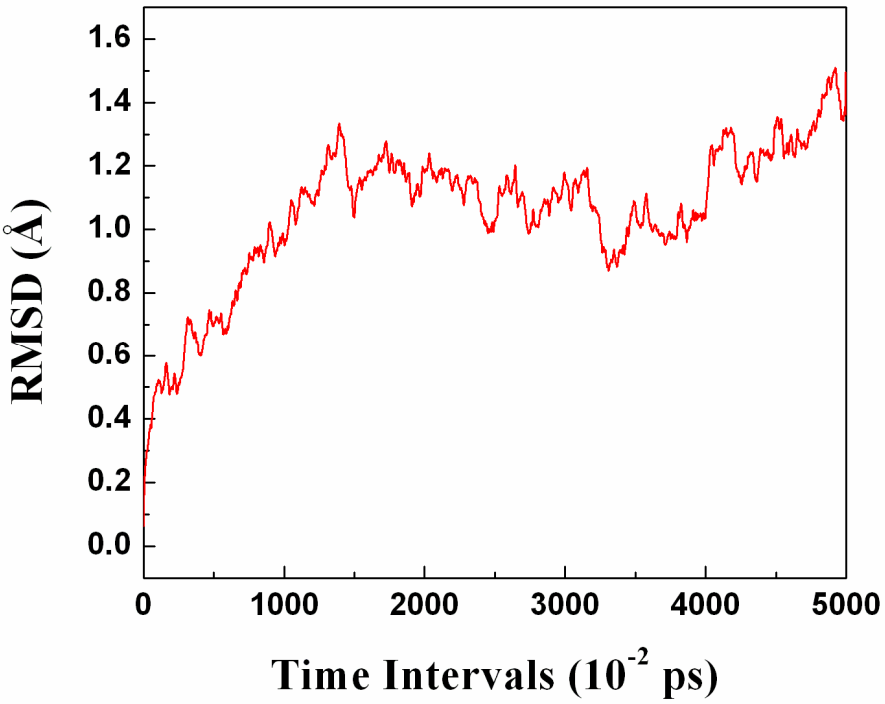

Figure 53: RMSD of ssDNA backbone in NVT ensemble.

The RMSD of the nucleic acid backbone was computed by a similar method for the NPT ensemble. The simulation was performed at 300 K temperature and 1 atm pressure. The ssDNA system was equilibrated at first for 50 ps, followed by the dynamics study of 400 ps. The RMSD showed a change of approximately $3\,\mathring{A}$ with the progress of time (**Figure 54**) during the dynamics study. These results indicated that the ssDNA might have been undergoing structural change from its previous conformation over time, in spite of the fact that the system maintained the consistency in the equilibrium thermodynamic conditions.

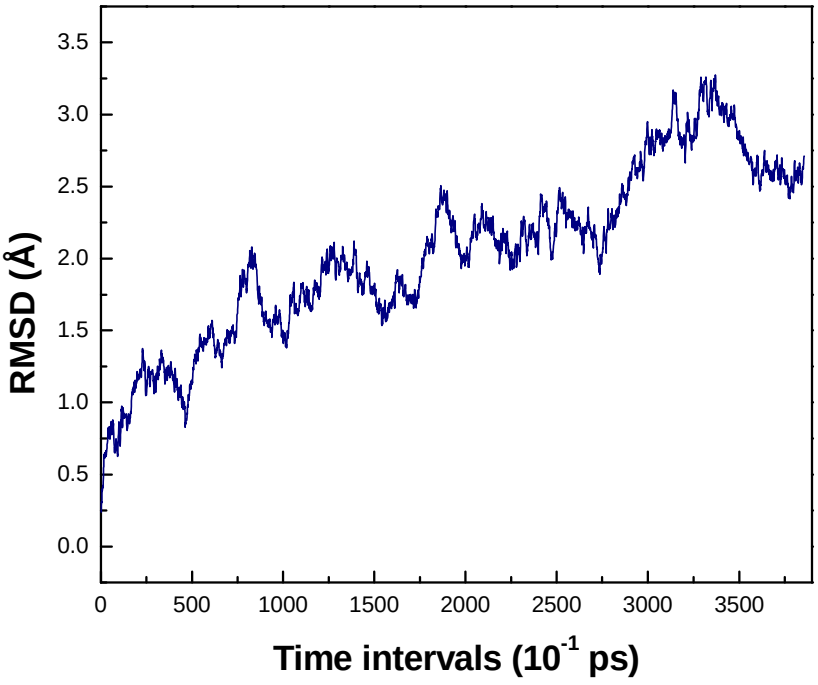

Figure 54: RMSD of ssDNA backbone in NPT ensemble

As the NPT ensemble resembles a closer description of the biological conditions, this latter study provides an idea of the conformational flexibility of the ssDNA under the ambient conditions. The proper thermodynamic conditions and the suitable conformational states of the ssDNA regulate the rate of the hybridization process. The selectivity and specificity of the hybridization of nucleic acids depend significantly on the conformational stability and flexibility of the ssDNA. Our study indicated the effect of thermodynamic conditions on the conformational state of the ssDNA, which could potentially modulate the qualitative features of DNA-based biosensing devices.

The conformational stability of ssDNA depends on the thermodynamic conditions, and the flexibility of ssDNA undergoes alteration with the change in the thermodynamic parameters of the system.

3.3. Preparing nanopore structures for biosensing: Effect of anodization conditions on the synthesis of TiO_2 nanopores

[**Adapted from the published article in *Proceedings of MRS Fall Meeting* 2006, Symposium E, 0951-E09-27**]

Nanoporous materials have drawn significant interest because of their versatile applications in fields such as optics [17], electronics [18], catalysis [19] and biosensing [20]. Various nanostructures, including nanopores and nanotubes, have been fabricated to manufacture nanoscale devices for chemical and biosensing processes [21]. Titanium dioxide (TiO_2) has emerged as an important oxide material in the development of nanopore based sensors [20]. The high refractive index (n=2.4) and semiconductive properties of TiO_2 are of great importance in photocatalytic and gas sensing processes [22, 23]. Since anodic oxidation of titanium metal can produce nano-architectured porous materials [24], the anodization process is a way to design large arrays of nanopores with variable size, shape and morphology.

Recently, various *in vitro* experiments have been conducted to describe the voltage driven transport of single stranded (ss) DNA through synthetic nanoporous structures [25, 26] and protein suspended in a lipid layer [27]. The investigation of the voltage driven translocation of polynucleic acids (e.g. DNA, RNA) through nanopore structures has given rise to the idea of developing novel nanopore based biosensing devices and DNA sequencing techniques [27]. Since inorganic nanostructures display chemical, mechanical and thermal rigidity under diverse experimental conditions, their nanoporous environment can be adjusted [28]. Accordingly, solid-state nanopores made of oxide materials have an advantage over biological nanopores in the development of biosensors and the modeling of biomolecular transport through cellular nanostructures [20, 28].

As part of a continuing endeavor to utilize TiO_2 nanopores in the development of a nucleic acid sensor, the role of anodization conditions in the formation of TiO_2 nanoporous arrays was examined. As the morphology and dimensions of the nanopores significantly influence the sensitivity and selectivity of nanoscale devices, the ability to control these parameters by modifying the anodization conditions is imperative for sensor development. In the electrochemical anodization process, titanium acts as the anode, while platinum is used as the cathode in an electrochemical cell filled with a hydrofluoric acid electrolyte solution. During the preparation process, titanium is converted to its oxide form. Previous studies have described the effect of anodizing voltage and pH on TiO_2 nanopore dimensions and morphology [29, 30]. This study investigated the role of anodization time and electrolyte concentration in the synthesis of a large array of titanium oxide nanopores, at constant voltage. TiO_2 nanopores anodized in solutions of various HF concentrations or for various amounts of time were compared, to determine the effect of these anodization parameters on the nanopores.

3.3.1. Experimental Procedure

Titania nanopores were prepared by anodizing titanium foil in electrolyte solutions containing hydrofluoric acid (HF). Titanium foils with a thickness of 0.25 mm and 99.7 % purity were purchased from Sigma-Aldrich. The foil was cleaned by sonication in a solution of methanol, acetone, and isopropanol for 20 minutes. A Teflon electrochemical cell, which maintained single-sided contact between the electrodes and the electrolyte solution and held the electrodes at a distance of 2 mm, was used for the experiment. The metal foil was placed as the anode in the electrochemical cell, with a platinum cathode. HF solutions of different concentrations (0.5%, 1%, 5%, and 10%) were prepared in ultrapure water. Approximately 2 mL of electrolyte solution was used for each anodization process, and 2.27 cm^2 of the titanium surface was exposed to the electrolyte solution. Using a power supply (VWR AccuPower), a constant potential of 20 V was applied to run the process with varying anodization times (5, 10, 20, and 30 minutes). To protect the oxide layer from dissolution, the TiO_2 sample was rapidly removed from the cell after anodization. Afterwards, the sample was rinsed with deionized water and dried with nitrogen gas. A scanning electron microscope (SEM, Hitachi S-2600) was used to characterize the nanopore structures.

3.3.2. Results and Discussion

Titanium oxide nanopores were successfully grown by anodic oxidation. Two principal anodization parameters, anodization time and concentration of HF electrolyte solutions, were regulated during the synthesis.

The SEM images (**Figure 55**) show the TiO_2 nanopore structures that were developed by the application of constant potential for 5 minutes. Keeping the anodizing time constant, the concentration of HF was altered to obtain the nanostructures. With a progressive increase in HF concentration (from 0.5% to 10%), the diameter of the nanopores gradually decreased, from approximately 100 nm diameter to 50 nm. The morphology of the nanostructures underwent a detectable transformation with the change in HF concentration. At low concentrations of HF (**Figure 55A &B**), the nanopores exhibited a distinct tube structure. The nanostructures formed at higher HF concentrations (**Figure 55 C &D**) displayed pores with interconnected walls. The results show that the nanopore dimensions can be modified by controlling HF concentration.

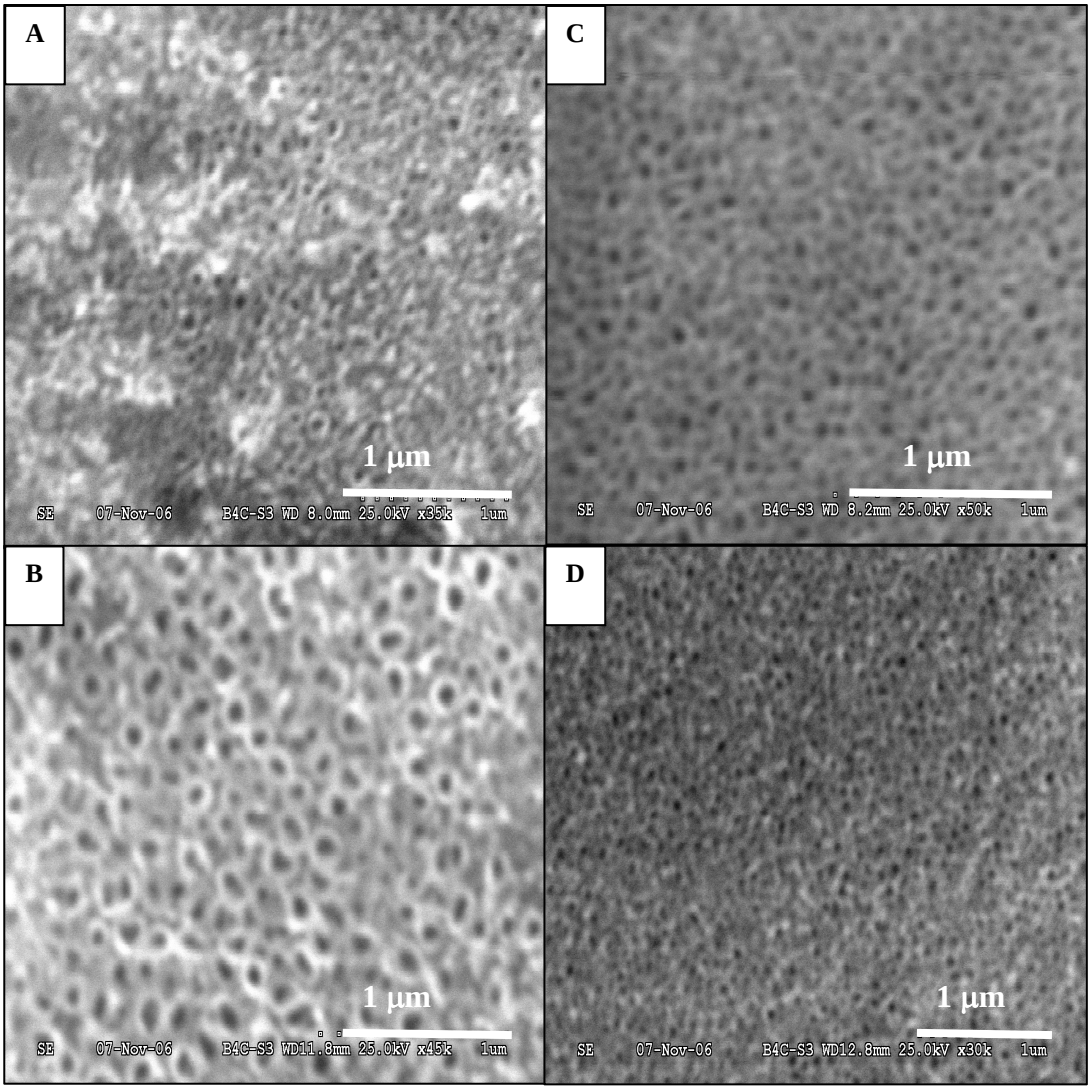

Figure 55: SEM images of TiO_2 nanopores prepared by anodization for 5 minutes in (A) 0.5 %, (B) 1%, (C) 5%, and (D) 10% HF solutions.

To examine the effect of the length of anodization time on the formation of nanopores, the anodic oxidation of titanium was carried out at 0.5 % HF concentration with reaction times from 5 min to 30 minutes (**Figure 56**).

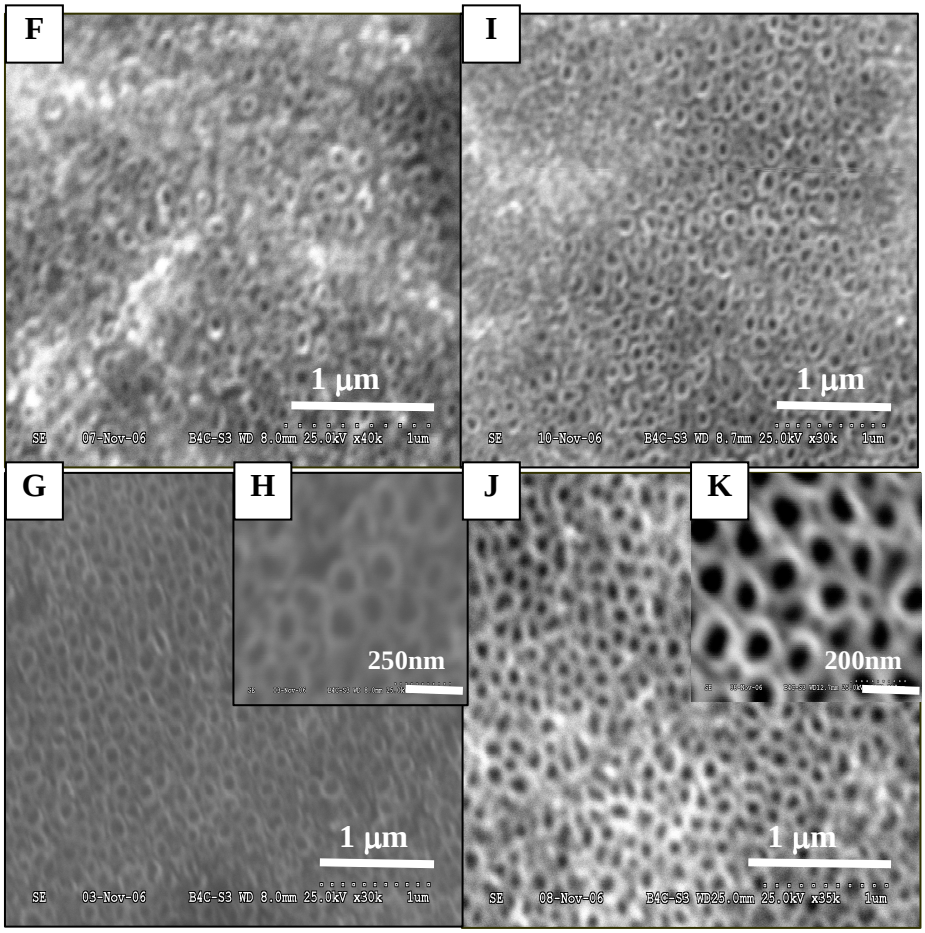

Figure 56: TiO_2 nanopores prepared by anodization in 0.5%HF for (F) 5 mins, (G) 10 mins, (I) 20 mins, and (J) 30 minutes. Inserts H and K show the structures formed at 10 and 30 minutes.

The pore size remained largely unaffected with the increase of anodization time. As anodization time increased, the nanopores showed a noticeable transformation from tube like structures to pore networks (**Figure 56**). An enhancement of the uniformity of the pore distribution was observed at longer anodization times (**Figure 56**, **I and J**).

A similar investigation was carried out at a higher concentration of HF (**Figure 57**). Titanium was anodized in 5% HF solution with varying reaction times from 5 minutes to 20 minutes.

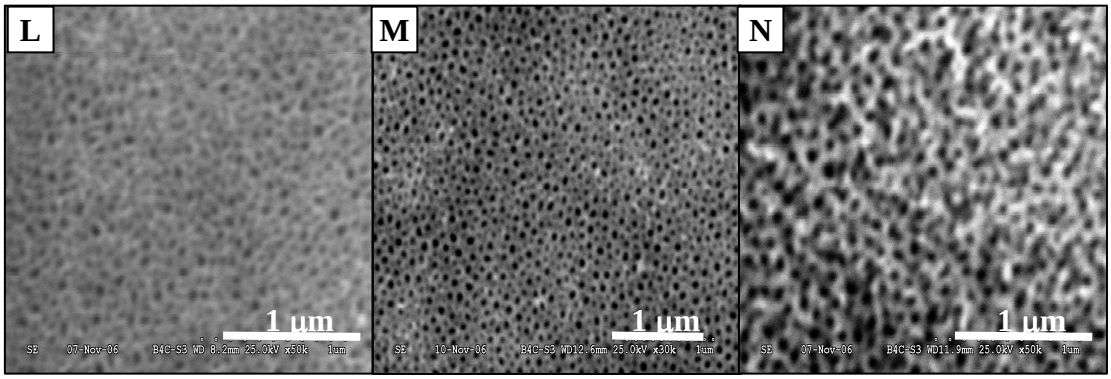

Figure 57: TiO_2 nanopores prepared by anodization in 5% HF for (L) 5 mins, (M) 10 mins, and (N) 20 mins.

Once again, varying the anodization time effected morphological changes in the nanopores. Long anodization times resulted in merging nanopore structures (**Figure 57N**), whereas, at shorter anodization times, distinct nanopores were obtained (**Figure 57, L & M**).

The formation of a titanium oxide nanoporous layer on the metal foil is controlled by three processes, field-enhanced oxidation of titanium foil, field–assisted oxide dissolution, and chemical oxide dissolution [29]. During field–enhanced oxidation, titanium metal is converted to its oxide form, as oxygen-containing ions in the solution move towards the interface of the metal and its oxide. During field-assisted oxide dissolution, titanium ions migrate from the metal-oxide interface through the oxide layer and dissolve into the solution. HF accelerates the rate of dissolution by consuming titanium ions in solution [30]. Since this mechanism includes no restriction of pore widening, the extensive dissolution which occurs over long anodization times leads to pore merging and the eventual loss of the nanopore structures.

This study qualitatively describes the dependence of the structure and morphology of TiO_2 nanopores on the two primary parameters of the anodic oxidation process at constant voltage. The pore size of TiO_2 nanostructures is affected by the electrolyte concentration during anodization, whereas the morphology and distribution of the nanopores is affected by both electrolyte concentration and anodization time. The study found that TiO_2 nanostructures show a unique tube-to-pore transition with an increase in anodization time and electrolyte concentration at constant voltage. The findings of this

study can be applied to modulate the growth of nanostructured oxide materials for use in nanopore based sensing devices.

3.4. Synthesis and Self-assembly of Lipid (DMPC)–capped Gold Nanoparticles

[***Adapted from the published article in Proceedings of MRS Fall Meeting 2007*, Symposium MM, 1061-MM09-08**]

The assembly of bio-conjugated colloidal nanomaterials has attracted extensive interest due to their tunable physiochemical properties that can be controlled as a function of their size, shape, aggregation state and local environment [31, 6]. Bio-conjugated nanomaterials play a promising role in the development of novel supramolecular architectures [31]. Hybrid organic-inorganic nanostructures have versatile technological potential for the development of integrated circuits [6], molecular machines [32], and biosensors [2]. Vigorous attempts have been made to obtain assembled structures of metallic [33] and semiconductor [34, 35] nanostructures (nanoparticles, nanorods) [36, 37] using various molecular systems such as polyelectrolytes [31, 33], surfactants [2], and long-chain hydrocarbons [38]. The ability to precisely control the overall size of an assembled structure and the separation distance between nanoparticulates remains a significant technical challenge [1,2,6,31,32,], yet the uniformity in an ordered structure controls the physical properties of the entire architecture [6, 31,32]. Additionally, the stability of nanoparticles in their assembled forms is imperative for the development of an integrated structure [2,6,31,33]. The interaction among capping reagents helps to maintain the stability of nanoparticles and the uniformity of their size [1]. Thus, the capping molecules play a crucial role in the formation of a stable assembly of nanoparticles as well as limiting the overall dimension of the assembled architecture [2, 31]. Moreover, it is crucial to retain the native properties of biomolecular capping

reagents after conjugating with nanomaterials, which play a critical role in establishing an ordered structure [1, 31, 32].

Phospholipids, integral components of cell membranes, are composed of polar head groups and nonpolar hydrocarbon tails [39]. Because of the amphiphilic nature of lipids, it is possible to modulate biomolecular interactions by altering the hydrophobic and hydrophilic components of their molecular framework. Hence, the use of phospholipids as capping reagents can facilitate the synthesis of a wide variety of biocompatible nanomaterials [40]. Many variations in the size and shape of the assembled nanostructures can be achieved by controlling the separation distance between nanoparticulates with atomic precision using selective molecular interactions of lipids [41, 42]. In addition, lipids can affect the dielectric properties of metallic nanoparticles, providing a way to modulate the optical properties of an integrated architecture and serve as optical sensors [2]. Through altering the nature of the polar head groups, the interaction between the lipid and nanoparticle can be adjusted [40]. The size and number of hydrocarbon tails can control dimensions and kinetics to form an assembly of lipid-capped nanomaterials. Additionally, various types of lipids can be mixed [42] to alter the separation distance between nanoparticles. Owing to the lipid's amphiphilic characteristics, lipid-capped nanoparticles can be fabricated on substrates of various surface polarities [39]. Accordingly, a specific directionality in the growth of an assembled structure can be achieved to develop novel supramolecular architectures. Since the study of phospholipid assembly is used to model biological membranes [43], an investigation of the hybrid structures of metallic nanoparticles and phospholipids has

potential for the development of new biosensing devices and drug delivery methods across cellular membranes.

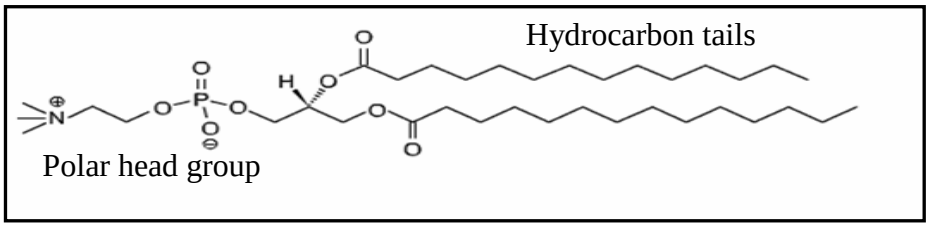

Figure 58: DMPC (1, 2-dimyristoyl-*sn*-glycero-3-phosphocholine)

In this study, lipid-capped gold nanoparticles were synthesized and allowed to form a self-assembled monolayer structure. The nanoparticles were prepared by a phase transfer method, which involved the reduction of potassium tetrachloroaurate(III) by sodium citrate in an aqueous solution and the simultaneous transfer of the reduced species to an organic medium containing DMPC (1,2-dimyristoyl-*sn*-glycero-3-phosphocholine), a phospholipid with two hydrophobic tails of 14 carbons each (**Figure 58**). The size and shape of the gold nanoparticles directly conjugated to DMPC were estimated in a solution phase and on a solid support using dynamic light scattering (DLS) and transmission electron microscopy (TEM), respectively. The Langmuir-Blodgett (LB) method, commonly applied to assemble long-chain amphiphilies on a liquid subphase or a solid substrate forming lamellar structures of lipids [43, 44], was utilized to form an assembled monolayer of lipid-capped nanoparticles. The measurement of the compression isotherm was used to signal the assemblage of lipid capped gold nanoparticles. Comparative analyses between assemblies of the DMPC capped gold nanoparticles and unmodified DMPC molecules were performed to understand the effect of the direct conjugation of

the gold nanoparticle on the lipid. By extending this method, the fabrication of nanoparticles films on a substrate can be achieved to develop solid-state devices [39].

3.4.1. Experimental Procedure

Materials

DMPC (1, 2-Dimyristoyl-sn-glycero-3-phosphocholine, Avanti Polar Lipids), toluene (HPLC grade, Sigma-Aldrich), potassium tetrachloroaurate (III) ($KAuCl_4$) (98%, Sigma-Aldrich), sodium citrate ($Na_3C_6H_5O_7$ X $2H_2O$) (99.0%, VWR) were purchased and Millipore water was used to prepare aqueous solutions.

3.4.2. Synthesis of DMPC-capped gold nanoparticles

The principle of phase transfer synthesis, generally applied to synthesize surfactants and amphiphile-capped nanostructures [1, 6, 40], was used to prepare the DMPC-capped gold nanoparticles in toluene. A solution of DMPC (0.25 mg/ml) in toluene was prepared in a 30 ml glass vial and stirred for 15 mins to ensure complete dissolution of the lipid in toluene. An aqueous solution of potassium tetrachloroaurate (III) (1.0 mg/ml) was prepared; 2 ml of the solution was added to 5 ml of the lipid solution and the mixture was stirred for 15 mins. While the mixture was being stirred, 1 ml of an aqueous solution of sodium citrate (10 mg/ml) was added dropwise. The reaction mixture was stirred for 8 hrs. Towards the end of the stirring, the organic phase turned into a clear deep red solution and the aqueous phase beneath it took on an opaque gray milky color. The organic layer was removed with a glass syringe.

3.4.3. Characterization of the gold nanoparticles

An Ocean Optics HR2000 spectrometer was used to study the UV-Vis absorption of gold nanoparticles in toluene that were placed into a 3.5 ml quartz cuvette of 1 cm pathlength. The hydrodynamic diameter and polydispersity of the gold nanoparticles in toluene were obtained at room temperature using a BIC 90plus DLS particle-size analyzer. The size and shape of the lipid-capped gold nanoparticles were investigated using a JEOL EX-1200 TEM after the nanoparticles were drop coated on a carbon coated copper TEM grid (300 mesh with formvar coating on one side, SPI Supplies, Structure Probe, Inc).

3.4.4. Assembly of DMPC-capped gold nanoparticles using Langmuir-Blodgett Apparatus

A Kibron Inc. (KBN315) Microtrough X was utilized to allow the self-assembly of the DMPC-capped gold nanoparticles onto a water subphase at room temperature.20 μl of the nanoparticle solution (DMPC concentration 0.25 mg/ml) was deposited onto a water surface using a Hamilton manual gas-tight microsyringe. After allowing 20 min to evaporate the organic solvent, the nanoparticles were compressed at the rate of 4.68 $Å^2$/ (molecule)/min. The compression isotherm was measured to monitor the self-assembly of the DMPC-capped gold nanoparticles. The same method was followed to assemble unmodified DMPC.

3.4.5. Results and Discussion

The optical absorption spectrum of the gold nanoparticles exhibited a peak at 525.73 nm, supporting the formation of stable nanoparticles in toluene (**Figure 59**) [2,40].

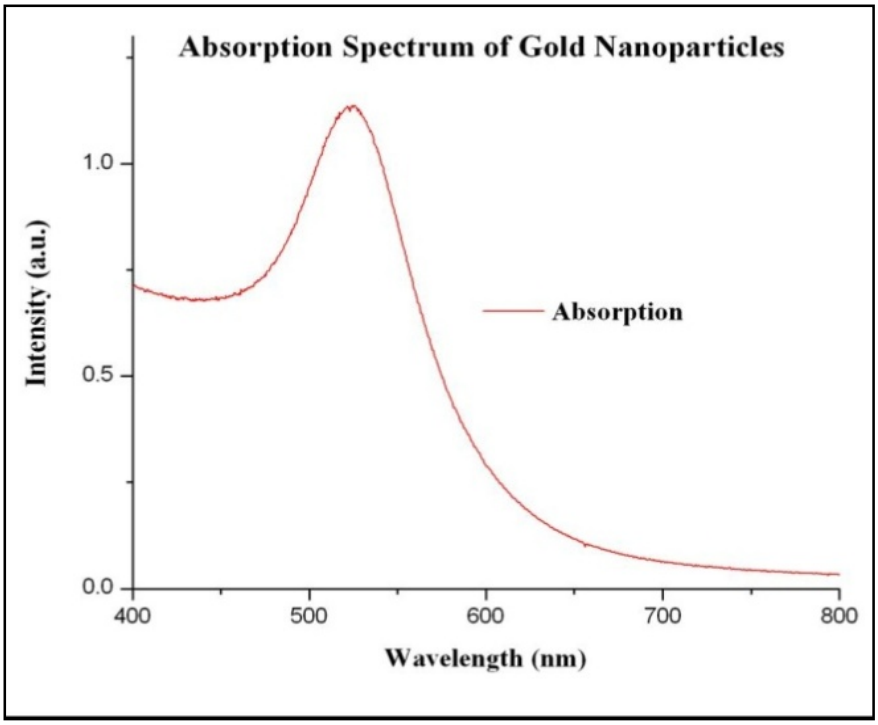

Figure 59: UV-Vis absorption spectrum of gold nanoparticles in toluene.

DLS utilizes temporal variations of fluctuations of the scattered light to measure an average hydrodynamic diameter of particles suspended in a liquid medium [45].

The results of dynamic light scattering showed the size of the lipid coated gold nanoparticles to be 31.5 nm with a polydispersity of 0.205 (**Figure 60**).

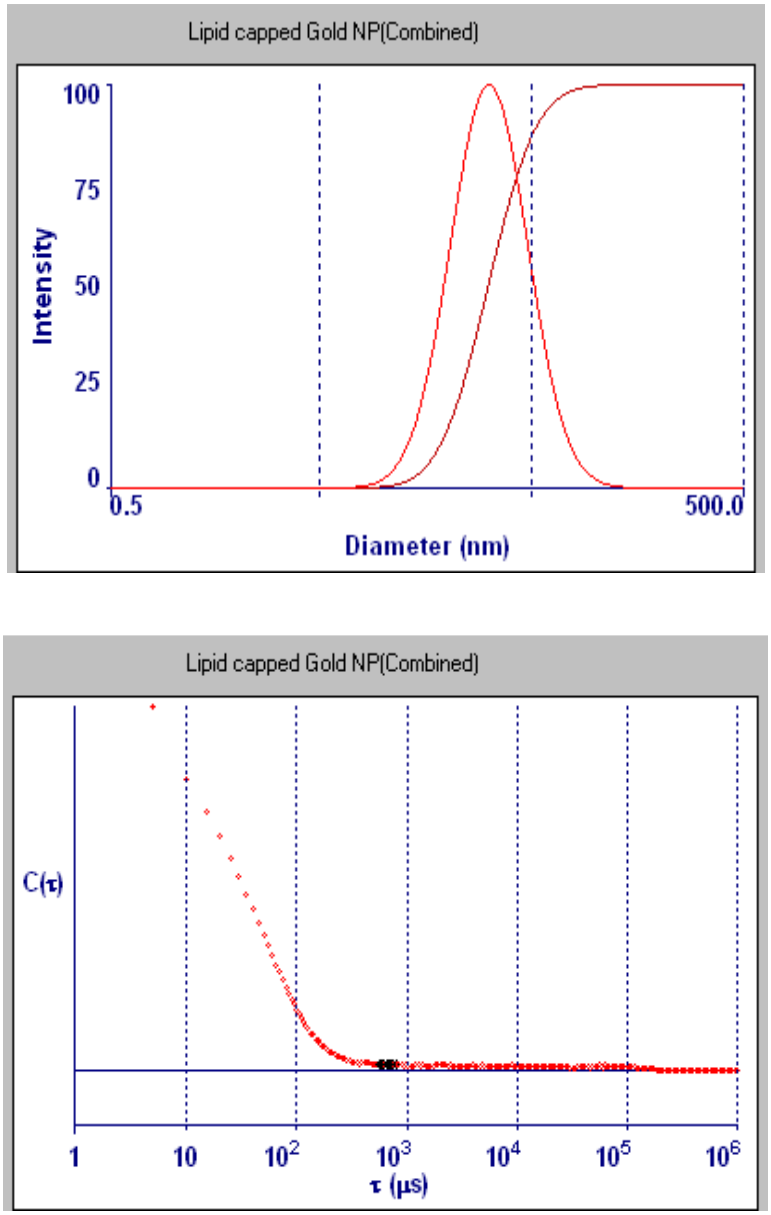

Figure 60: DLS analysis of gold nanoparticles from a lognormal plot of intensity vs. diameter of the nanoparticles. Fluctuations in the time intensity of the scattered light were processed by computing the autocorrelation function, C(τ), τ = decay time.

TEM showed the lipid capped gold nanoparticles maintained a spherical shape, with diameters ranging from 15 to 25 nm (**Figure 61**).

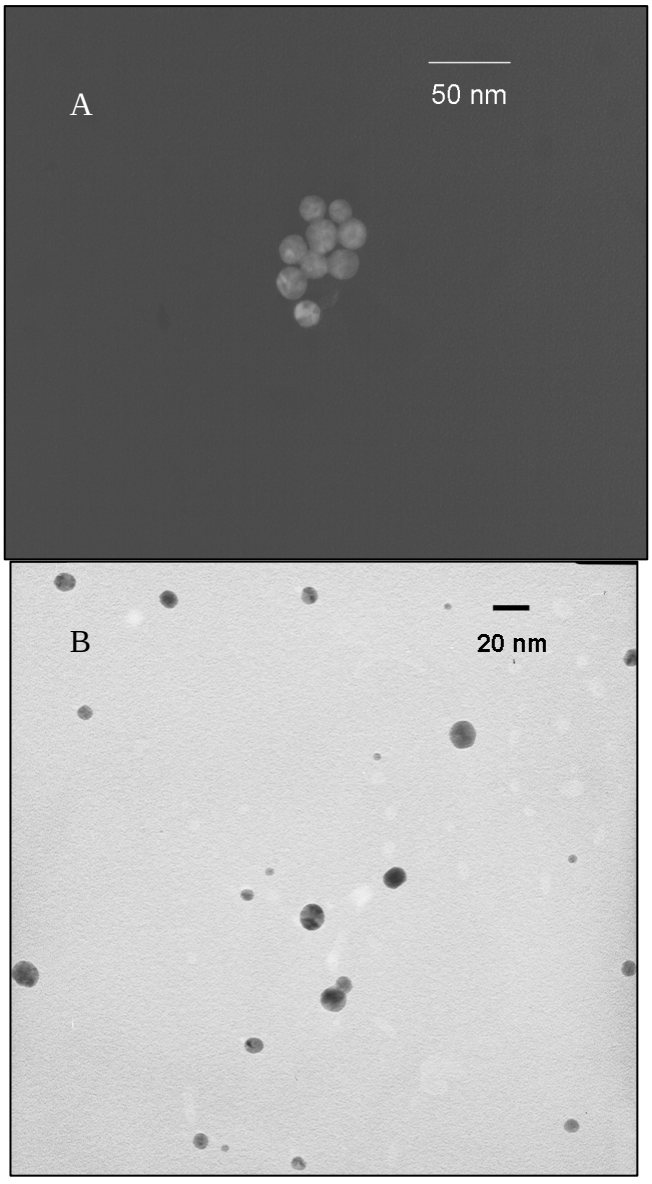

Figure 61: TEM images of gold nanoparticles at a magnification of 120k (A) and 200k (B).

The average hydrodynamic diameter of the gold nanoparticles obtained from DLS relies on intensity-weighting of the scattered light, which is expected to be biased towards larger particles due to their dominant effect on the light scattering. Although TEM imaging directly elucidates the geometric size and shape of the gold nanoparticle, it probes the colloidal nanoparticle outside of the solution phase and native environment.

The characteristic surface plasmon absorption (**Figure 59**) confirms the formation of the nanoscopic gold particulates in the solution phase [2, 6]. The spherical shape of the nanoparticles and their well-separated disposition in the TEM images (**Figure 61**) can conceivably be ascribed to the lipid capping molecules of the gold nanoparticles. Considering the structural similarities between lipids and surfactants [39, 40] and the proposed nature of the interaction of surfactants with metallic nanoparticles [1,6], it may be suggested that the polar head group of DMPC stabilizes thenanoparticles by forming non-covalent bonds. The hydrocarbon tails of the attached lipids extend beyond the surface of the nanoparticle, assist in maintaining a stable solution in nonpolar toluene by providing a hydrophobic shield preventing nanoparticle aggregation.

The compression isotherms (**Figure 62A &B**) indicate the formation of a monolayer for both unmodified DMPC and the lipid-capped gold nanoparticles onto a water surface as described before.

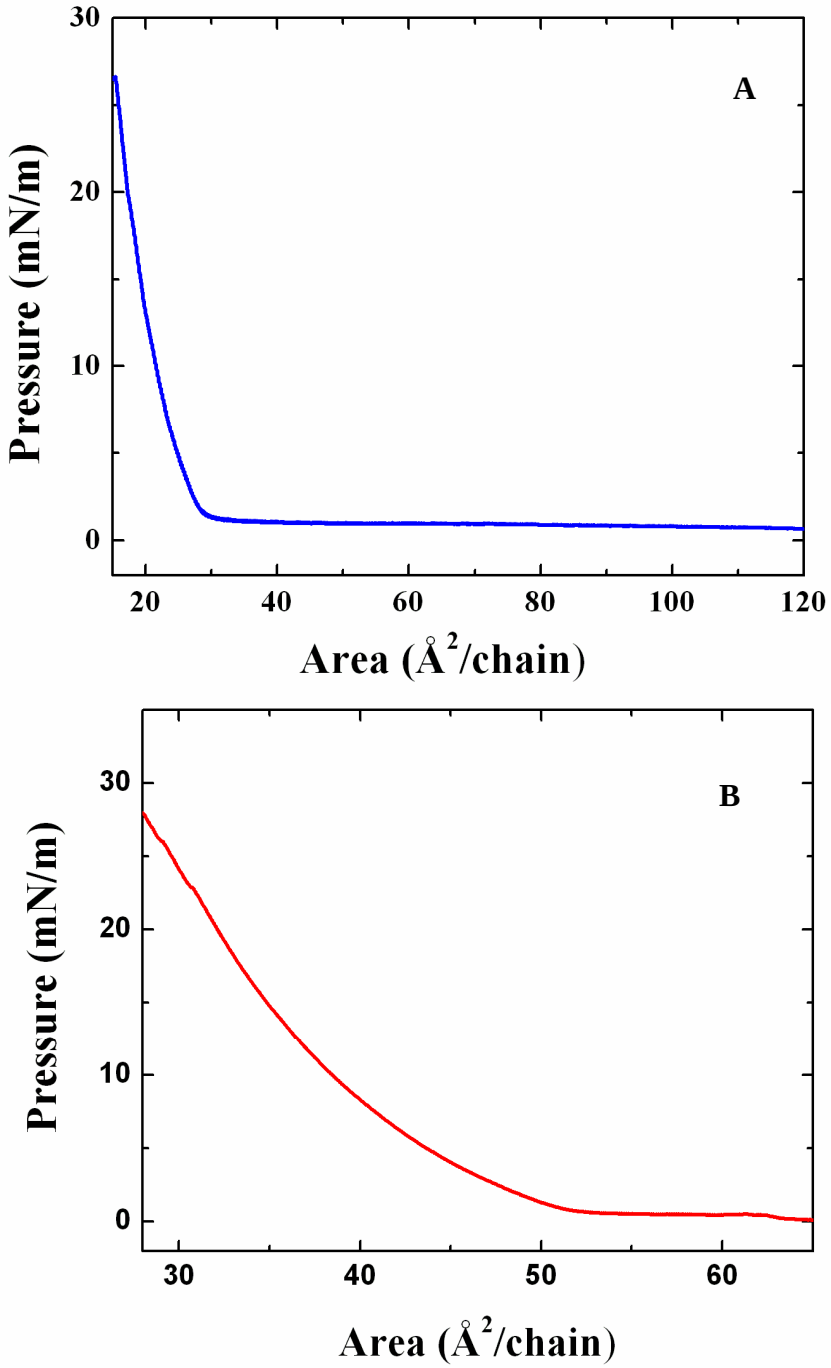

Figure 62: Compression isotherm (π –A) curves of DMPC (A) and DMPC capped gold nanoparticles (B).

In general, theoretical modeling of the formation of a monolayer of lipids onto a water surface using the LB method shows a first-order phase transition [43] and a pressure-change in the compression isotherm indicative of formation of a new phase (**Figure 62**). Initially, lipids form as a "gas-like" dispersed phase on a water subphase, keeping their hydrophobic tails away from the aqueous phase [43, 46]. With the application of a directed force by movement of the LB barriers, the lipids form an ordered assembly on top of the polar aqueous phase because of the strong hydrophobic interaction of the lipid's hydrocarbon tails [43, 44, 46]. The lipids conjugated to the nanoparticles exhibited a similar behavior, which supports the inference that the associated lipids retained their ability to form an assembled structure. Due to the association with the gold nanoparticles, the modified DMPC experienced a localized ordering, causing a shift of the rising point of the pressure (kink at 51.008 $Å^2$/ chain) at the compression isotherm curve (**Figure 62B**).

In this study, the ability to synthesize DMPC-capped gold nanoparticles and to form an assembly of the phospholipid-conjugated gold nanoparticles onto an aqueous subphase was tested. It was found that the direct conjugation of DMPC stabilized the nanoparticles, and conversely that bonding to nanoparticles controlled the organization of the lipids. Thus, lipid molecules conjugated with nanoparticles exhibited a relatively different compression isotherm compared to the original lipid molecules assembled alone. The change in the pressure of the compression isotherm signals the assembly of the lipid molecules. Accordingly, it should be possible to develop nanoparticles capped directly with lipids as self-assembled and controllable structures.

3.5. Investigating bio-molecular functionalization of gold nanoparticles

[**Adapted from the published article in *Technical Proceedings of the NSTI Nanotechnology Conference and Trade Show 2006*, 2, 436-439**]

There has been a growing interest in the use of metallic nanoparticles to develop novel bio-conjugated nanostructures and biosensing devices [1,7,47-51], in particular the size-dependent optical properties of nanomaterials such as surface plasmon resonance (SPR) play an important role in elucidating the specific molecular recognition event of biomolecules (protein, DNA) conjugated with nanomaterials [1,7,51]. For example, gold nanoparticles have been used to detect the hybridization process of nucleic acids and specific antigen-antibody interactions, which can be applied to develop bio-sensing devices [2,7]. The hybridization process of the gold nanoparticle-conjugated DNA has been used to develop a colorimetric detection technique to identify single-base mismatches in a DNA sequence [52]. Metallic nanoparticles have been applied to develop ultra sensitive quartz crystal microbalance and scanometric DNA array detector [52,53].

To develop bio-conjugated nanostructures and devices, nanoparticles are functionalized with linker molecules that establish the connectivity between nanoparticles and biomolecules of interest (e.g. nucleic acids) [1]. The linker molecules possess specific functional groups, which make bonds between the nanoparticles and DNA strands (or the modified end of nucleic acid strands or proteins) [1,2,7]. For instance, avidin, streptavidin, and biotin have been employed as linker molecules to establish a covalent connection between biomolecules and nanostructures, since the avidin-biotin complex remains highly stable in a wide temperature and pH range [49, 54]. Biotin, a water-

soluble B-complex vitamin, binds to streptavidin and avidin, two naturally occurring proteins [55]. Avidin is a basic glycoprotein (MW 68 kDa). The strong affinity of biotin to avidin was documented by the estimation of the dissociation constant, ($K_d = 4 \times 10^{-14}$ M for streptavidin, and 6×10^{-16} M for avidin) [55,56].

The attachment of functional linker molecules to nanoparticles can impart variable effects on their physiochemical properties of the nanoparticles [1,2,7]. Due to the surface modification of the nanoparticles by the attachment of biomolecules, the optical properties and stability of nanoparticles can undergo considerable change [2]. Conversely, the attachment of nanoparticles to biomolecules can lead to a modification in the natural binding property of the linker biomolecules [2,48].

In this study, we discuss the synthesis and optical properties of gold nanoparticles functionalized with two linker biomolecules, namely, biotin and BSA-biotin, as biotin can function as an effective linker molecule to connect other target biomolecules with nanoparticles [49, 54]. This study uses the physical phenomena of size dependent surface plasmon resonance, which has been used to signal the change in the nanoparticle's dimension as its absorption maximum shifts to greater wavelengths due to aggregation of the nanoparticles [47,57]. To investigate the effect of the linker functional biomolecules on the nanoparticles, we synthesized the functionalized gold nanoparticles in an aqueous phase maintaining similar experimental conditions.

3.5.1. Experimental Procedures

Materials

Potassium tetrachloroaurate (III) [$KAuCl_4$] (99.99% (metals basis), gold [Au] (49% min, packed under argon), sodium borohydride [$NaBH_4$] (99%), biotin (d-Biotin, 99%), and Bovin Serum Albumin (BSA)-Biotin were purchased from Sigma Aldrich.

Synthesis of the gold nanoparticles

The gold nanoparticles were prepared by reduction of $KAuCl_4$ with $NaBH_4$ in the presence of biotin. Biotin was attached to the gold nanoparticle during the synthesis process ('one pot' method). 1mL of $KAuCl_4$ solution (10^{-4} M) was added to 89 mL of deionized water. Then, 1 mL biotin solution (3.6 X 10^{-6} M) was added with constant stirring. Thereafter, 10 mL $NaBH_4$ solution (10^{-4} M) was added dropwise and the solution was allowed to stir for ~ 3 hours, maintaining the temperature within 0-5 ^{o}C to obtain the final product. Correspondingly, the BSA-biotin functionalized gold nanoparticles were prepared by the reaction of $KAuCl_4$ and $NaBH_4$ in aqueous solution containing BSA-biotin. 1 mL of BSA-biotin solution (3.4 mg/ml) was added to 89 mL of $KAuCl_4$ solution with constant stirring at room temperature. Then, 10 mL of $NaBH_4$ solution was added dropwise, and the solution was stirred for ~ 4 hours maintaining the abovementioned temperature range.

Characterization of the gold nanoparticles

Dynamic light scattering (DLS, 90Plus/BI-MS-Particle Size Analyzer, Brookhaven Instrument Corporation) was used to measure the effective diameter the functionalized gold nanoparticles in the aqueous solution at room temperature (25^{o}C). A fiber coupled Ocean Optics spectrophotometer (HR2000) was used to obtain the absorption spectra of the gold nanoparticle solution.

3.5.2. Results and Discussion

A characteristic absorption spectrum depicts the size-dependent optical behavior of the nanoparticles [47]. Additionally, the UV-Vis spectrum of bioconjugated nanoparticles provides qualitative information of the stability of the nanomaterial system.

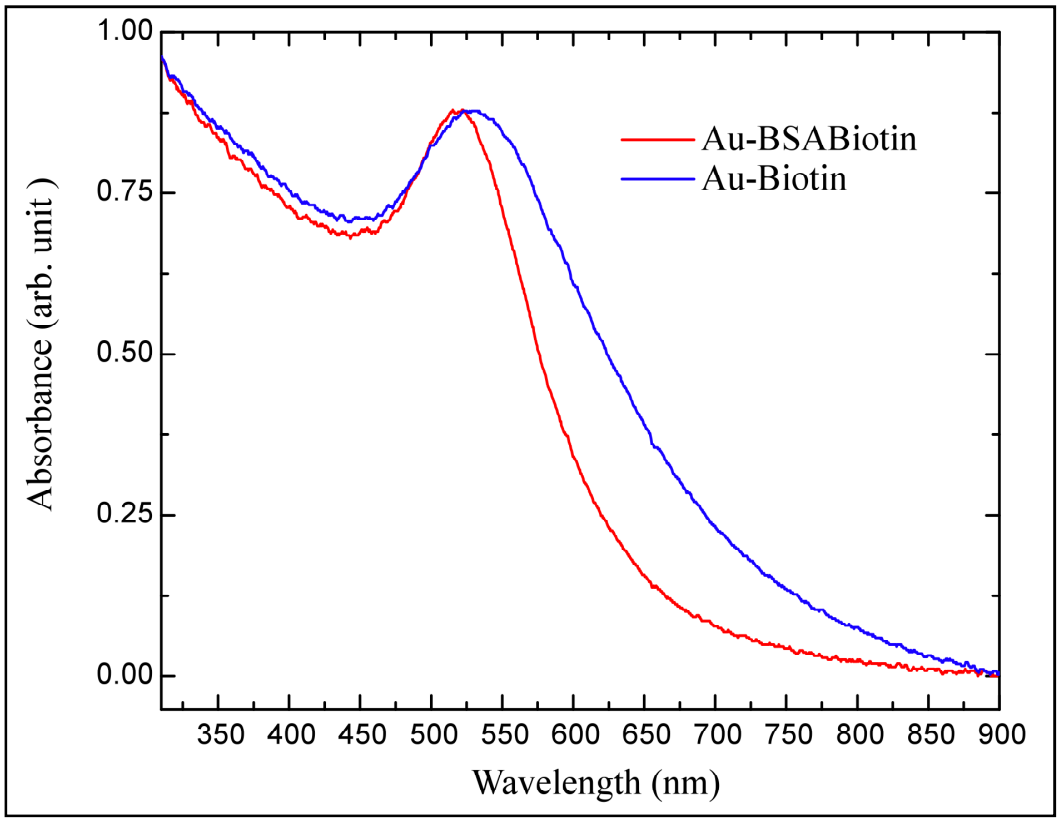

Figure 63: UV-Vis absorption spectra of the biotinylated gold and BSA-biotinylated gold nanoparticles.

UV-Vis spectral analyses of the dispersed colloidal gold nanoparticles resulted in a characteristic absorption maximum of the nanoparticle. The biotinylated gold nanoparticles exhibited a maximum at 528 nm (**Figure 63**), whereas BSA-biotinylated gold nanoparticles showed an absorption maximum at 521 nm (**Figure 63**). Neither BSA-biotin nor biotin alone exhibited any absorption maxima in that wavelength range. This wavelength shift of the nanoparticles indicates that the nature of the capping biomolecules affected the overall size of the nanoparticles.

DLS employs temporal variations of the scattered light to measure the size of the particles suspended in a liquid medium (**Figure 64**). The effective diameter of the nanoparticles represents an average size of the particles in the sample.

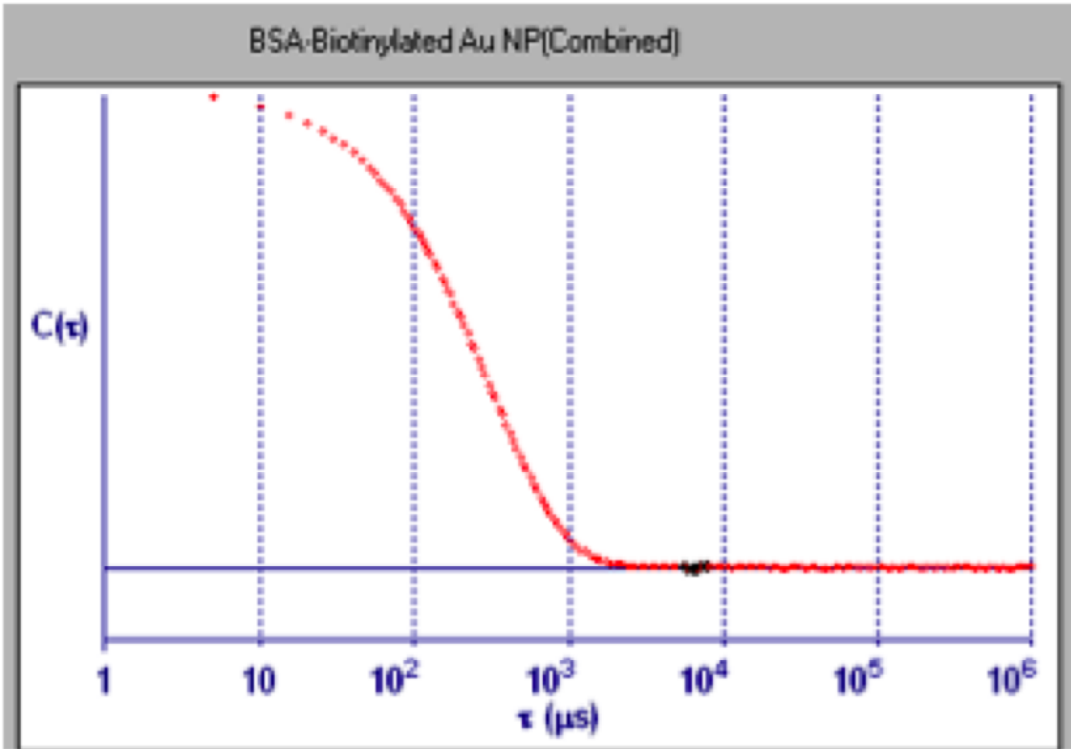

Figure 64: An autocorrelation of the scattered light intensity trace recorded during DLS experiment

Table 3 shows sizes of the gold nanoparticles attached to different biotin molecules.

Nanoparticle	Effective diameter (nm)	Standard deviation
Biotin-gold	58.5	1.9
BSA-biotin- gold	96.9	0.4

Table 3: Diameters of the gold nanoparticles measured by DLS

The attachment of linker molecules causes a change in the hydrodynamic diameter of the nanoparticles as indicated by the trends in the diameter of the nanoparticles (**Table 3**). Accordingly, the coupling process of nanoparticles with biomolecules is expected to play an important role in bio-template reactions and nanoparticles assembly, as the physical properties of the nanostructures depend on the attached biomolecules.

This study showed a qualitative picture of the effect of biomolecular functionalization on gold nanoparticles. The process of bio-functionalization can influence the optical properties and physical dimension of nanostructures synthesized at the similar experimental conditions.

3.6. References

1. Niemeyer, C.M., Nanoparticles, Proteins, and Nucleic Acids: Biotechnology Meets Materials Science. *Angewandte Chemie International Edition* **2001,***40* (22), 4128-4158.

2. Rosi, N. L.; Mirkin, C. A., Nanostructures in biodiagnostics. *Chem Rev* **2005,***105* (4), 1547-62.

3. Demidov, V. V.; Frank-Kamenetskii, M. D., Two sides of the coin: affinity and specificity of nucleic acid interactions. *Trends Biochem Sci* **2004,***29* (2), 62-71.

4. Samori, B.; Zuccheri, G., DNA codes for nanoscience. *Angew Chem Int Ed Engl* **2005,***44* (8), 1166-81.

5. Michael C. Pirrung, How to Make a DNA Chip. *Angewandte Chemie International Edition* **2002,***41* (8), 1276-1289.

6. Katz, E.; Willner, I., Integrated nanoparticle-biomolecule hybrid systems: synthesis, properties, and applications. *Angew Chem Int Ed Engl* **2004,***43* (45), 6042-108.

7. West, J. L.; Halas, N. J., Applications of nanotechnology to biotechnology commentary. *Curr Opin Biotechnol* **2000,***11* (2), 215-7.

8. Cho, Y.; Gorina, S.; Jeffrey, P. D.; Pavletich, N. P., Crystal structure of a p53 tumor suppressor-DNA complex: understanding tumorigenic mutations. *Science* **1994,***265* (5170), 346-55.

9. Karplus, M.; Kuriyan, J., Molecular dynamics and protein function. *Proc Natl Acad Sci U S A* **2005,***102* (19), 6679-85.

10. Phillips, J. C.; Braun, R.; Wang, W.; Gumbart, J.; Tajkhorshid, E.; Villa, E.; Chipot, C.; Skeel, R. D.; Kale, L.; Schulten, K., Scalable molecular dynamics with NAMD. *J Comput Chem* **2005,***26* (16), 1781-802.

11. Case, D. A.; Cheatham, T. E., 3rd; Darden, T.; Gohlke, H.; Luo, R.; Merz, K. M., Jr.; Onufriev, A.; Simmerling, C.; Wang, B.; Woods, R. J., The Amber biomolecular simulation programs. *J Comput Chem* **2005,***26* (16), 1668-88.

12. Cheatham, T. E.; Young, M. A., Molecular dynamics simulation of nucleic acids: successes, limitations, and promise. *Biopolymers* **2000,***56* (4), 232-56.

13. Humphrey, W.; Dalke, A.; Schulten, K., VMD: visual molecular dynamics. *J Mol Graph* **1996,***14* (1), 33-8, 27-8.

14. Tuckerman, M. E.; Martyna, G. J., Understanding Modern Molecular Dynamics: Techniques and Applications. *The Journal of Physical Chemistry B* **2001,***105* (31), 7598-7598.

15. Leger, J. F.; Robert, J.; Bourdieu, L.; Chatenay, D.; Marko, J. F., RecA binding to a single double-stranded DNA molecule: a possible role of DNA conformational fluctuations. *Proc Natl Acad Sci U S A* **1998,***95* (21), 12295-9.

16. Zhao, X.; Striolo, A.; Cummings, P. T., C_{60} binds to and deforms nucleotides. *Biophys J* **2005,***89* (6), 3856-62.

17. Tian, L.; Ram, K. B.; Ahmad, I.; Menon, L.; Holtz, M., Optical properties of a nanoporous array in silicon. *Journal of Applied Physics* **2005,***97* (2), -.

18. Hu, Y. S.; Guo, Y. G.; Sigle, W.; Hore, S.; Balaya, P.; Maier, J., Electrochemical lithiation synthesis of nanoporous materials with superior catalytic and capacitive activity. *Nat Mater* **2006,***5* (9), 713-7.

19. Hepel, M.; Kumarihamy, I.; Zhong, C. J., Nanoporous TiO2-supported bimetallic catalysts for methanol oxidation in acidic media. *Electrochemistry Communications* **2006,***8* (9), 1439-1444.

20. Nakane, J. J.; Akeson, M.; Marziali, A., Nanopore sensors for nucleic acid analysis. *Journal of Physics-Condensed Matter* **2003,***15* (32), R1365-R1393.

21. Baker, L. A.; Choi, Y. S.; Martin, C. R., Nanopore membranes for biomaterials synthesis, biosensing and bioseparations. *Current Nanoscience* **2006,***2* (3), 243-255.

22. Mor, G. K.; Shankar, K.; Paulose, M.; Varghese, O. K.; Grimes, C. A., Enhanced Photocleavage of Water Using Titania Nanotube Arrays. *Nano Letters* **2004,***5* (1), 191-195.

23. Paulose, M.; Varghese, O. K.; Mor, G. K.; Grimes, C. A.; Ong, K. G., Unprecedented ultra-high hydrogen gas sensitivity in undoped titania nanotubes. *Nanotechnology* **2006,***17* (2), 398-402.

24. Choi, J. S.; Wehrspohn, R. B.; Lee, J.; Gosele, U., Anodization of nanoimprinted titanium: a comparison with formation of porous alumina. *Electrochimica Acta* **2004,***49* (16), 2645-2652.

25. Pan, S. L.; Rothberg, L. J., Interferometric sensing of biomolecular binding using nanoporous aluminum oxide templates. *Nano Letters* **2003,***3* (6), 811-814.

26. Storm, A. J.; Storm, C.; Chen, J. H.; Zandbergen, H.; Joanny, J. F.; Dekker, C., Fast DNA translocation through a solid-state nanopore. *Nano Letters* **2005,***5* (7), 1193-1197.

27. Aksimentiev, A.; Schulten, K., Imaging alpha-hemolysin with molecular dynamics: Ionic conductance, osmotic permeability, and the electrostatic potential map. *Biophysical Journal* **2005,***88* (6), 3745-3761.

28. Heng, J. B.; Ho, C.; Kim, T.; Timp, R.; Aksimentiev, A.; Grinkova, Y. V.; Sligar, S.; Schulten, K.; Timp, G., Sizing DNA using a nanometer-diameter pore. *Biophysical Journal* **2004,***87* (4), 2905-2911.

29. Quan, X.; Yang, S. G.; Ruan, X. L.; Zhao, H. M., Preparation of titania nanotubes and their environmental applications as electrode. *Environmental Science & Technology* **2005,***39* (10), 3770-3775.

30. Gong, D.; Grimes, C. A.; Varghese, O. K.; Hu, W. C.; Singh, R. S.; Chen, Z.; Dickey, E. C., Titanium oxide nanotube arrays prepared by anodic oxidation. *Journal of Materials Research* **2001,***16* (12), 3331-3334.

31. Hamley, I. W., Nanotechnology with Soft Materials. *Angewandte Chemie International Edition* **2003,***42* (15), 1692-1712.

32. Wouters,D.; Schubert, U. S., Nanolithography and Nanochemistry: Probe-Related Patterning Techniques and Chemical Modification for Nanometer-Sized Devices. *Angewandte Chemie International Edition* **2004,***43* (19), 2480-2495.

33. Huang, S.; Tsutsui, G.; Sakaue, H.; Shingubara, S.; Takahagi, T., Formation of a large-scale Langmuir--Blodgett monolayer of alkanethiol-encapsulated gold particles. *Journal of Vacuum Science & Technology B: Microelectronics and Nanometer Structures* **2001,***19* (1), 115-120.

34. Shen, Y.-J.; Lee, Y.-L.; Yang, Y.-M., Monolayer Behavior and Langmuir-Blodgett Manipulation of CdS Quantum Dots. *The Journal of Physical Chemistry B* **2006,***110* (19), 9556-9564.

35. Colvin, V. L.; Goldstein, A. N.; Alivisatos, A. P., Semiconductor nanocrystals covalently bound to metal surfaces with self-assembled monolayers. *Journal of the American Chemical Society* **1992,***114* (13), 5221-5230.

36. Takahashi, M.; Natori, H.; Tajima, K.; Kobayashi, K., Particulate assemblies of CdS and TiO2 prepared by Langmuir-Blodgett technique with octadecylamine/methylstearate mixed films. *Thin Solid Films* **2005,***489* (1-2), 205-214.

37. Yang, Y.; Xiong, L.; Shi, J.; Nogami, M., Aligned Silver Nnanorod Arrays for Surface-Enhanced Raman Scattering*Nanotechnology***2006**17,2670-2674.

38. Diem, T.; Fabianowski, W.; Jaccodine, R.; Rodowski, R., Self-assembly formed oxime monolayers on a copper surface. *Thin Solid Films* **1995,***265* (1-2), 71-73.

39. Lee, Y.-L.; Lin, J.-Y.; Chang, C.-H., Thermodynamic characteristics and Langmuir-Blodgett deposition behavior of mixed DPPA/DPPC monolayers at air/liquid interfaces. *Journal of Colloid and Interface Science* **2006,***296* (2), 647-654.

40. Zhu, H.; Tao, C.; Zheng, S.; Li, J., One step synthesis and phase transition of phospholipid-modified Au particles into toluene. *Colloids and Surfaces A: Physicochemical and Engineering Aspects* **2005,***257-258*, 411-414.

41. Nieh, M.-P.; Raghunathan, V. A.; Glinka, C. J.; Harroun, T. A.; Pabst, G.; Katsaras, J., Magnetically Alignable Phase of Phospholipid &BicelleMixtures is a Chiral Nematic Made Up of Wormlike Micelles. *Langmuir* **2004,***20* (19), 7893-7897.

42. Ma, G.; Allen, H. C., Condensing Effect of Palmitic Acid on DPPC in Mixed Langmuir Monolayers. *Langmuir* **2007,***23* (2), 589-597.

43. Kaganer, V. M.; Möhwald, H.; Dutta, P., Structure and phase transitions in Langmuir monolayers. *Reviews of Modern Physics* **1999,***71* (3), 779-819.

44. Basu, J. K.; Sanyal, M. K., Ordering and growth of Langmuir-Blodgett films: X-ray scattering studies. *Physics Reports* **2002,***363* (1), 1-84.

45. Berne, B. J., Pecora, R**.,** *Dynamic Light Scattering : With Applications to Chemistry, Biology, and Physics*,Unabridged edition; Dover Publications2000.

46. Meyer, E. E.; Lin, Q.; Hassenkam, T.; Oroudjev, E.; Israelachvili, J. N., Origin of the long-range attraction between surfactant-coated surfaces. *Proceedings of the National Academy of Sciences of the United States of America* **2005,***102* (19), 6839-6842.

47. Elghanian, R.; Storhoff, J. J.; Mucic, R. C.; Letsinger, R. L.; Mirkin, C. A., Selective Colorimetric Detection of Polynucleotides Based on the Distance-Dependent Optical Properties of Gold Nanoparticles. *Science* **1997,***277* (5329), 1078-1081.

48. Beaucage, S. L., Strategies in the Preparation of DNA Oligonucleotide Arrays for Diagnostic Applications. *Current Medicinal Chemistry* **2001,***8*, 1213-1244.

49. Caswell, K. K.; Wilson, J. N.; Bunz, U. H. F.; Murphy, C. J., Preferential End-to-End Assembly of Gold Nanorods by Biotin−Streptavidin Connectors. *Journal of the American Chemical Society* **2003,***125* (46), 13914-13915.

50. Aslan, K.; Holley, P.; Davies, L.; Lakowicz, J. R.; Geddes, C. D., Angular-Ratiometric Plasmon-Resonance Based Light Scattering for Bioaffinity Sensing. *Journal of the American Chemical Society* **2005,***127* (34), 12115-12121.

51. Alivisatos, P., The use of nanocrystals in biological detection. *Nat Biotech* **2004,***22* (1), 47-52.

52. Taton, T. A.; Mirkin, C. A.; Letsinger, R. L., Scanometric DNA Array Detection with Nanoparticle Probes. *Science* **2000,***289* (5485), 1757-1760.

53. Xu, J.; Craig, S. L., Thermodynamics of DNA Hybridization on Gold Nanoparticles. *Journal of the American Chemical Society* **2005,***127* (38), 13227-13231.

54. Roll, D.; Malicka, J.; Gryczynski, I.; Gryczynski, Z.; Lakowicz, J. R., Metallic Colloid Wavelength-Ratiometric Scattering Sensors. *Analytical Chemistry* **2003,***75* (14), 3440-3445.

55. Qureshi, M. H.; Yeung, J. C.; Wu, S.-C.; Wong, S.-L., Development and Characterization of a Series of Soluble Tetrameric and Monomeric Streptavidin Muteins with Differential Biotin Binding Affinities. *J. Biol. Chem.* **2001,***276* (49), 46422-46428.

56. Holmberg,A.; Blomstergren,A. ; Nord,O.; Lukacs,M.; Lundeberg,J.; Uhlén,M., The biotin-streptavidin interaction can be reversibly broken using water at elevated temperatures. *Electrophoresis* **2005,***26* (3), 501-510.

57. Lytton-Jean, A. K. R.; Mirkin, C. A., A thermodynamic investigation into the binding properties of DNA functionalized gold nanoparticle probes and molecular fluorophore probes. *Journal of the American Chemical Society* **2005,***127* (37), 12754-12755.

4. Bibliography

4.1. Chapter1:

1. Hill, H. Z., The Function of Melanin or 6 Blind People Examine an Elephant. *Bioessays***1992**, 14 (1), 49-56.

2. Bell, A. A.; Wheeler, M. H., Biosynthesis and Functions of Fungal Melanins. *Annual Review of Phytopathology***1986**, 24, 411-451.

3. Garcia-Rivera, J.; Eisenman, H. C.; Nosanchuk, J. D.; Aisen, P.; Zaragoza, O.; Moadel, T.; Dadachova, E.; Casadevall, A., Comparative analysis of *Cryptococcus neoformans* acid-resistant particles generated from pigmented cells grown in different laccase substrates. *Fungal Genetics and Biology***2005**, 42 (12), 989-998.

4. Langfelder, K.; Streibel, M.; Jahn, B.; Haase, G.; Brakhage, A. A., Biosynthesis of fungal melanins and their importance for human pathogenic fungi. *Fungal Genetics and Biology* **2003**, 38 (2), 143-158.

5. Tian, S. Y.; Garcia-Rivera, J.; Yan, B.; Casadevall, A.; Stark, R. E., Unlocking the molecular structure of fungal melanin using C-13 biosynthetic labeling and solid-state NMR. *Biochemistry***2003**, 42 (27), 8105-8109.

6. Zhong, J. Y.; Frases, S.; Wang, H.; Casadevall, A.; Stark, R. E., Following fungal melanin biosynthesis with solid-state NMR: Biopolyrner molecular structures and possible connections to cell-wall polysaccharides. *Biochemistry***2008**, 47 (16), 4701-4710.

7. Nosanchuk, J. D.; Valadon, P.; Feldmesser, M.; Casadevall, A., Melanization of Cryptococcus neoformans in murine infection. *Molecular and Cellular Biology***1999**, 19 (1), 745-750.

8. Rosas, A. L.; Nosanchuk, J. D.; Feldmesser, M.; Cox, G. M.; McDade, H. C.; Casadevall, A., Synthesis of polymerized melanin by *Cryptococcus neoformans* in infected rodents. *Infection and Immunity***2000**, 68 (5), 2845-2853.

9. Duff, G. A.; Roberts, J. E.; Foster, N., Analysis of the structure of synthetic and natural melanins by solid-phase NMR. *Biochemistry***2002**, 27 (18), 7112.

10. Bhavin B. Adhyaru; Novruz G. Akhmedov; Alan R. Katritzky; Clifford R. Bowers, Solid-state cross-polarization magic angle spinning 13C and 15N NMR characterization of Sepia melanin, Sepia melanin free acid and Human hair melanin in comparison with several model compounds. *Magnetic Resonance in Chemistry***2003**, 41 (6), 466-474.

11. Casadevall, A., Evolution of Intracellular Pathogens. *Annual Review of Microbiology***2008**, 62, 19-33.

12. Dadachova, E.; Nosanchuk, J. D.; Shi, L.; Schweitzer, A. D.; Frenkel, A.; Nosanchuk, J. S.; Casadevall, A., Dead cells in melanoma tumors provide abundant antigen for targeted delivery of ionizing radiation by a mAb to melanin. *Proceedings of the National Academy of Sciences of the United States of America***2004**, 101 (41), 14865-14870.

13. Wang, Y. L.; Aisen, P.; Casadevall, A., Melanin, melanin "ghosts," and melanin composition in Cryptococcus neoformans. *Infection and Immunity***1996**, 64 (7), 2420-2424.

14. Kayser, H.; Palivan, C. G., Stable free radicals in insect cuticles: Electron spin resonance spectroscopy reveals differences between melanization and sclerotization. *Archives of Biochemistry and Biophysics***2006**, 453 (2), 179-187.

15. Sealy, R.; Hyde, J.; Felix, C.; Menon, I.; Prota, G., Eumelanins and pheomelanins: characterization by electron spin resonance spectroscopy. *Science***1982**, 217 (4559), 545-547.

16. Reszka, K. J.; Matuszak, Z.; Chignell, C. F., Lactoperoxidase-Catalyzed Oxidation of Melanin by Reactive Nitrogen Species Derived From Nitrite (NO_2^-): An EPR Study. *Free Radical Biology and Medicine***1998**, 25 (2), 208-216.

17. Kalyanaraman, B.; Felix, C. C.; Sealy, R. C., Photoionization and photohomolysis of melanins: an electron spin resonance-spin trapping study. *Journal of the American Chemical Society***2002**, 106 (24), 7327.

18. Wielgus, A. R.; Sarna, T., Melanin in human irides of different color and age of donors. *Pigment Cell Research***2005**, 18 (6), 454-464.

19. Hong, L.; Simon, J. D., Current understanding of the binding sites, capacity, affinity, and biological significance of metals in melanin. *Journal of Physical Chemistry B***2007**, 111 (28), 7938-7947.

20. Nighswander-Rempel, S. P.; Riesz, J.; Gilmore, J.; Bothma, J. P.; Meredith, P., Quantitative Fluorescence Excitation Spectra of Synthetic Eumelanin. *The Journal of Physical Chemistry B***2005**, 109 (43), 20629.

21. Stark, K. B.; Gallas, J. M.; Zajac, G. W.; Golab, J. T.; Gidanian, S.; McIntire, T.; Farmer, P. J., Effect of stacking and redox state on optical absorption spectra of melanins-comparison of theoretical and experimental results. *Journal of Physical Chemistry B***2005**, 109 (5), 1970-1977.

22. Galvao, D. S.; Caldas, M. J., Polymerization of 5,6-Indolequinone - a View into the Band-Structure of Melanins. *Journal of Chemical Physics***1988**, 88 (6), 4088-4091.

23. Cheng, J.; Moss, S. C.; Eisner, M.; Zschack, P., X-Ray Characterization of Melanins .1. *Pigment Cell Research***1994**, 7 (4), 255-262.

24. Cheng, J.; Moss, S. C.; Eisner, M., X-Ray Characterization of Melanins .2. *Pigment Cell Research***1994**, 7 (4), 263-273.

25. Geis, P. A.; Wheeler, M. H.; Szaniszlo, P. J., Pentaketide Metabolites of Melanin Synthesis in the Dematiaceous Fungus Wangiella-Dermatitidis. *Archives of Microbiology***1984**, 137 (4), 324-328.

26. Brakhage A. A.; Langfelder, K.; Wanner, G.; Schmidt, A; Jahn, B., Pigment biosynthesis and virulence. *Contributions to microbiology***1999**, 2, 205-15.

27. Missall, T. A.; Moran J. M.; Corbett, J. A.; Lodge, J. K., Distinct stress responses of two functional laccases in *Cryptococcus neoformans* are revealed in the absence of the thiol-specific antioxidant Tsa1. *Eukaryot. Cell***2005**, 4,202.

28. Williamson, P. R., Biochemical and Molecular Characterization of the Diphenol Oxidase of Cryptococcus-Neoformans - Identification as a Laccase. *Journal of Bacteriology***1994**, 176 (3), 656-664.

29. Williamson, P. R., Laccase and melanin in the pathogenesis of Cryptococcus neoformans. *Front Biosci***1997**, 2, e99-e107.

30. Polacheck, I.; Kwonchung, K. J., Melanogenesis in *Cryptococcus-Neoformans*. *Journal of General Microbiology***1988**, 134, 1037-1041.

31. Folch,J., Lees,M. and Stanley,G.H.S., A simple method for the isolation and purification of total lipides from animal tissues *J. Biol. Chem*., 226, 497-509 (1957).

32. Duer, M. J., Solid State NMR Spectroscopy: Principles and Applications. Wiley-Blackwell: 2002.

33. Laws, D. D.; Bitter, H. M. L.; Jerschow, A., Solid-state NMR spectroscopic methods in chemistry. *Angewandte Chemie-International Edition***2002**, 41 (17), 3096-3129.

34. McDermott, A., Structure and Dynamics of Membrane Proteins by Magic Angle Spinning Solid-State NMR. *Annual Review of Biophysics***2009**, 38 (1), 385-403.

35. Tycko, R., Biomolecular solid state NMR: Advances in structural methodology and applications to peptide and protein fibrils. *Annual Review of Physical Chemistry***2001**, 52, 575-606.

36. Luca, S.; Heise, H.; Baldus, M., High-resolution solid-state NMR applied to polypeptides and membrane proteins. *Accounts of Chemical Research***2003**, 36 (11), 858-865.

37. Baldus, M., Solid-state NMR spectroscopy: Molecular structure and organization at the atomic level. *Angewandte Chemie-International Edition***2006**, 45 (8), 1186-1188.

38. Schwalbe, H.; Bielecki,A., Recent Advances in High-Resolution Solid-State NMR Spectroscopy13. *Angewandte Chemie International Edition***2001**, 40 (11), 2045-2050.

39. Peersen, O. B.; Wu, X. L.; Smith, S. O., Enhancement of CP-MAS Signals by Variable-Amplitude Cross Polarization. Compensation for Inhomogeneous B_1 Fields. *Journal of Magnetic Resonance, Series A***1994**, 106 (1), 127-131.

40. Metz, G.; Wu, X. L.; Smith, S. O., Ramped-Amplitude Cross-Polarization in Magic-Angle-Spinning NMR. *Journal of Magnetic Resonance Series A***1994**, 110 (2), 219-227.

41. Opella, S. J.; Frey, M. H., Selection of nonprotonated carbon resonances in solid-state nuclear magnetic resonance. *Journal of the American Chemical Society***2002**, 101 (19), 5854.

42. Takegoshi, K.; Nakamura, S.; Terao, T., ^{13}C-^{1}H dipolar-assisted rotational resonance in magic-angle spinning NMR. *Chemical Physics Letters***2001**, 344 (5-6), 631-637.

43. Takegoshi, K.; Nakamura, S.; Terao, T., ^{13}C-^{1}H dipolar-driven ^{13}C-^{13}C recoupling without ^{13}C rf irradiation in nuclear magnetic resonance of rotating solids. *The Journal of Chemical Physics***2003**, 118 (5), 2325-2341.

44. Takegoshi, K.; Terao, T., 13C nuclear Overhauser polarization nuclear magnetic resonance in rotating solids: Replacement of cross polarization in uniformly ^{13}C labeled molecules with methyl groups. *The Journal of Chemical Physics***2002**, 117 (4), 1700-1707.

45. Crocker, E.; Patel, A. B.; Eilers, M.; Jayaraman, S.; Getmanova, E.; Reeves, P. J.; Ziliox, M.; Khorana, H. G.; Sheves, M.; Smith, S. O., Dipolar assisted rotational resonance NMR of tryptophan and tyrosine in rhodopsin. *Journal of Biomolecular Nmr***2004**, 29 (1), 11-20.

46. Yang, J.; Paramasivan, S.; Marulanda, D.; Cataidi, M.; Tasayco, M. L.; Polenova, T., Magic angle spinning NMR spectroscopy of thioredoxin reassemblies. *Magnetic Resonance in Chemistry***2007**, 45, S73-S83.

47. Carvalho, G. M. J.; Alves, T. L. M.; Freire, D. M. G., L-DOPA production by immobilized tyrosinase. *Applied Biochemistry and Biotechnology***2000**, 84-6, 791-800.

48. Ho, P. Y.; Chiou, M. S.; Chao, A. C., Production of L-DOPA by tyrosinase immobilized on modified polystyrene. *Applied Biochemistry and Biotechnology***2003**, 111 (3), 139-152.

4.2 Chapter 2:

1. Sapsford, K. E.; Berti, L.; Medintz, I. L., Materials for fluorescence resonance energy transfer analysis: Beyond traditional donor-acceptor combinations. *Angewandte Chemie-International Edition***2006**, 45 (28), 4562-4588.

2. Royer, C. A., Probing protein folding and conformational transitions with fluorescence. *Chemical Reviews* **2006,***106* (5), 1769-1784.

3. Lakowicz, J. R., *Principles of Fluorescence Spectroscopy*. 3rd ed.; Plenum Publishing Corporation: 2006.

4. Borland, L. M.; Kottegoda, S.; Phillips, K. S.; Allbritton, N. L., Chemical Analysis of Single Cells. *Annual Review of Analytical Chemistry* **2008,***1* (1), 191-227.

5. Umezawa, Y., Optical Probes for Molecular Processes in Live Cells. *Annual Review of Analytical Chemistry* **2008,***1*, 397-421.

6. Joo, C.; Balci, H.; Ishitsuka, Y.; Buranachai, C.; Ha, T., Advances in single-molecule fluorescence methods for molecular biology. *Annual Review of Biochemistry* **2008,***77*, 51-76.

7. Weiss, S., Fluorescence spectroscopy of single biomolecules. *Science* **1999,***283* (5408), 1676-1683.

8. Ha,T., Single-Molecule FRET. *Single Molecules* **2001,***2* (4), 283-284.

9. Hess, S. T.; Huang, S. H.; Heikal, A. A.; Webb, W. W., Biological and chemical applications of fluorescence correlation spectroscopy: A review. *Biochemistry* **2002,***41* (3), 697-705.

10. Xu, Q. H.; Gaylord, B. S.; Wang, S.; Bazan, G. C.; Moses, D.; Heeger, A. J., Time-resolved energy transfer in DNA sequence detection using water-soluble conjugated polymers: The role of electrostatic and hydrophobic interactions. *Proceedings of the National Academy of Sciences of the United States of America* **2004,***101* (32), 11634-11639.

11. Szollosi, J.; Damjanovich, S.; Matyus, L., Application of fluorescence resonance energy transfer in the clinical laboratory: Routine and research. *Cytometry* **1998,***34* (4), 159-179.

12. Patterson, G. H.; Piston, D. W.; Barisas, B. G., Forster distances between green fluorescent protein pairs. *Analytical Biochemistry* **2000,***284* (2), 438-440.

13. Jang, S., Generalization of the Forster resonance energy transfer theory for quantum mechanical modulation of the donor-acceptor coupling. *J Chem Phys* **2007,***127* (17), 174710.

14. Beechem, J. M.; Brand, L., Time-Resolved Fluorescence of Proteins. *Annual Review of Biochemistry* **1985,***54*, 43-71.

15. Kapusta, P.; Wahl, M.; Benda, A.; Hof, M.; Enderlein, J., Fluorescence lifetime correlation spectroscopy. *Journal of Fluorescence* **2007,***17* (1), 43-48.

16. Meseth, U.; Wohland, T.; Rigler, R.; Vogel, H., Resolution of fluorescence correlation measurements. *Biophysical Journal* **1999,***76* (3), 1619-1631.

17. Enderlein, J.; Erdmann, R., Fast fitting of multi-exponential decay curves. *Optics Communications* **1997,***134* (1-6), 371-378.

18. Rosi, N. L.; Mirkin, C. A., Nanostructures in biodiagnostics. *Chemical Reviews* **2005,***105* (4), 1547-1562.

19. Yun, C. S.; Javier, A.; Jennings, T.; Fisher, M.; Hira, S.; Peterson, S.; Hopkins, B.; Reich, N. O.; Strouse, G. F., Nanometal surface energy transfer in optical rulers, breaking the FRET barrier. *Journal of the American Chemical Society* **2005,***127* (9), 3115-3119.

20. Jennings, T. L.; Singh, M. P.; Strouse, G. F., Fluorescent lifetime quenching near d=1.5 nm gold nanoparticles: Probing NSET validity. *Journal of the American Chemical Society* **2006,***128* (16), 5462-5467.

21. Kim, Y.-P.; Oh, Y.-H.; Oh, E.; Ko, S.; Han, M.-K.; Kim, H.-S., Energy Transfer-Based Multiplexed Assay of Proteases by Using Gold Nanoparticle and Quantum Dot Conjugates on a Surface. *Analytical Chemistry* **2008,***80* (12), 4634-4641.

22. Ray, P. C.; Darbha, G. K.; Ray, A.; Walker, J.; Hardy, W., Gold nanoparticle based FRET for DNA detection. *Plasmonics* **2007,***2* (4), 173-183.

23. Bhowmick, S.; Saini, S.; Shenoy, V. B.; Bagchi, B., Resonance energy transfer from a fluorescent dye to a metal nanoparticle. *J Chem Phys* **2006,***125* (18), 181102.

24. Saini, S.; Singh, H.; Bagchi, B., Fluorescence resonance energy transfer (FRET) in chemistry and biology: Non-Forster distance dependence of the FRET rate. *Journal of Chemical Sciences* **2006,***118* (1), 23-35.

25. Saini, S.; Srinivas, G.; Bagchi, B., Distance and Orientation Dependence of Excitation Energy Transfer: From Molecular Systems to Metal Nanoparticles. *Journal of Physical Chemistry B* **2009,***113* (7), 1817-1832.

26. Li, Y. G.; Tseng, Y. D.; Kwon, S. Y.; D'Espaux, L.; Bunch, J. S.; Mceuen, P. L.; Luo, D., Controlled assembly of dendrimer-like DNA. *Nature Materials* **2004,***3* (1), 38-42.

27. Lin, C. X.; Liu, Y.; Rinker, S.; Yan, H., DNA tile based self-assembly: Building complex nanoarchitectures. *Chemphyschem* **2006,***7* (8), 1641-1647.

28. Swathi, R. S.; Sebastian, K. L., Resonance energy transfer from a fluorescent dye molecule to plasmon and electron-hole excitations of a metal nanoparticle. *J Chem Phys* **2007,***126* (23), 234701.

29. Persson, B. N. J.; Lang, N. D., Electron-Hole-Pair Quenching of Excited-States near a Metal. *Physical Review B* **1982,***26* (10), 5409-5415.

30. Singh, M. P.; Jennings, T. L.; Strouse, G. F., Tracking Spatial Disorder in an Optical Ruler by Time-Resolved NSET. *Journal of Physical Chemistry B* **2009,***113* (2), 552-558.

31. Luo, D.; Saltzman, W. M., Synthetic DNA delivery systems. *Nature Biotechnology* **2000,***18* (1), 33-37.

32. Seeman, N. C., Nucleic-Acid Junctions and Lattices. *Journal of Theoretical Biology* **1982,***99* (2), 237-247.

33. Um, S. H.; Lee, J. B.; Park, N.; Kwon, S. Y.; Umbach, C. C.; Luo, D., Enzyme-catalysed assembly of DNA hydrogel. *Nature Materials* **2006,***5* (10), 797-801.

34. Um, S. H.; Lee, J. B.; Kwon, S. Y.; Li, Y.; Luo, D., Dendrimer-like DNA-based fluorescence nanobarcodes. *Nature Protocols* **2006,***1* (2), 995-1000.

35. Li, Y. G.; Cu, Y. T. H.; Luo, D., Multiplexed detection of pathogen DNA with DNA-based fluorescence nanobarcodes. *Nature Biotechnology* **2005,***23* (7), 885-889.

36. Frechet, J. M. J., Dendrimers and supramolecular chemistry. *Proceedings of the National Academy of Sciences of the United States of America* **2002,***99* (8), 4782-4787.

37. Lee, C. C.; MacKay, J. A.; Frechet, J. M. J.; Szoka, F. C., Designing dendrimers for biological applications. *Nature Biotechnology* **2005,***23* (12), 1517-1526.

38. Freedman, K. O.; Lee, J.; Li, Y. G.; Luo, D.; Skobeleva, V. B.; Ke, P. C., Diffusion of single star-branched dendrimer-like DNA. *Journal of Physical Chemistry B* **2005,***109* (19), 9839-9842.

39. Klimov, V. I., Spectral and Dynamical Properties of Multiexcitons in Semiconductor Nanocrystals. *Annual Review of Physical Chemistry* **2007,***58* (1), 635-673.

40. Bailey, R. E.; Smith, A. M.; Nie, S. M., Quantum dots in biology and medicine. *Physica E-Low-Dimensional Systems & Nanostructures* **2004,***25* (1), 1-12.

41. Parak, W. J.; Gerion, D.; Pellegrino, T.; Zanchet, D.; Micheel, C.; Williams, S. C.; Boudreau, R.; Le Gros, M. A.; Larabell, C. A.; Alivisatos, A. P., Biological applications of colloidal nanocrystals. *Nanotechnology* **2003,***14* (7), R15-R27.

42. Michalet, X.; Pinaud, F. F.; Bentolila, L. A.; Tsay, J. M.; Doose, S.; Li, J. J.; Sundaresan, G.; Wu, A. M.; Gambhir, S. S.; Weiss, S., Quantum dots for live cells, in vivo imaging, and diagnostics. *Science* **2005,***307* (5709), 538-544.

43. Chan, W. C.; nbsp; W.; Nie, S., Quantum Dot Bioconjugates for Ultrasensitive Nonisotopic Detection. *Science* **1998,***281* (5385), 2016-2018.

44. Klein, D. L.; Roth, R.; Lim, A. K. L.; Alivisatos, A. P.; McEuen, P. L., A single-electron transistor made from a cadmium selenide nanocrystal. *Nature* **1997,***389* (6652), 699-701.

45. Greenham, N. C.; Peng, X. G.; Alivisatos, A. P., Charge separation and transport in conjugated-polymer/semiconductor-nanocrystal composites studied by photoluminescence quenching and photoconductivity. *Physical Review B* **1996,***54* (24), 17628-17637.

46. Park, N. M.; Kim, T. S.; Park, S. J., Band gap engineering of amorphous silicon quantum dots for light-emitting diodes. *Applied Physics Letters* **2001,***78* (17), 2575-2577.

47. Lu, H.; Schops, O.; Woggon, U.; Niemeyer, C. M., Self-assembled donor comprising quantum dots and fluorescent proteins for long-range fluorescence resonance energy transfer. *Journal of the American Chemical Society* **2008,***130* (14), 4815-4827.

48. Gill, R.; Willner, I.; Shweky, I.; Banin, U., Fluorescence resonance energy transfer in CdSe/ZnS-DNA conjugates: Probing hybridization and DNA cleavage. *Journal of Physical Chemistry B* **2005,***109* (49), 23715-23719.

49. Viktoriya Sokolova; Matthias Epple, Inorganic Nanoparticles as Carriers of Nucleic Acids into Cells. *Angewandte Chemie International Edition* **2008,***47* (8), 1382-1395.

50. Schlegel, G.; Bohnenberger, J.; Potapova, I.; Mews, A., Fluorescence decay time of single semiconductor nanocrystals. *Physical Review Letters* **2002,***88* (13), 137401.

51. Fisher, B. R.; Eisler, H. J.; Stott, N. E.; Bawendi, M. G., Emission intensity dependence and single-exponential behavior in single colloidal quantum dot fluorescence lifetimes. *Journal of Physical Chemistry B* **2004,***108* (1), 143-148.

52. Private communication with Evident Technology Inc.

53. Pons, T.; Medintz, I. L.; Sykora, M.; Mattoussi, H., Spectrally resolved energy transfer using quantum dot donors: Ensemble and single-molecule photoluminescence studies. *Physical Review B* **2006,***73* (24), 245302.

54. Bawendi, M. G.; Carroll, P. J.; Wilson, W. L.; Brus, L. E., Luminescence Properties of Cdse Quantum Crystallites - Resonance between Interior and Surface Localized States. *Journal of Chemical Physics* **1992,***96* (2), 946-954.

55. Crooker, S. A.; Barrick, T.; Hollingsworth, J. A.; Klimov, V. I., Multiple temperature regimes of radiative decay in CdSe nanocrystal quantum dots: Intrinsic limits to the dark-exciton lifetime. *Applied Physics Letters* **2003,***82* (17), 2793-2795.

56. Hours, J.; Senellart, P.; Peter, E.; Cavanna, A.; Bloch, J., Exciton radiative lifetime controlled by the lateral confinement energy in a single quantum dot. *Physical Review B* **2005,***71* (16), 161306(R).

57. Alivisatos, P., The use of nanocrystals in biological detection. *Nature Biotechnology* **2004,***22* (1), 47-52.

58. Lim, T. C.; Bailey, V. J.; Ho, Y. P.; Wang, T. H., Intercalating dye as an acceptor in quantum-dot-mediated FRET. *Nanotechnology* **2008,***19* (7), 075701.

59. Rasnik, I.; Mckinney, S. A.; Ha, T., Surfaces and orientations: Much to FRET about? *Accounts of Chemical Research* **2005,***38* (7), 542-548.

4.3. Chapter 3:

1. Niemeyer, C.M., Nanoparticles, Proteins, and Nucleic Acids: Biotechnology Meets Materials Science. *Angewandte Chemie International Edition* **2001,***40* (22), 4128-4158.

2. Rosi, N. L.; Mirkin, C. A., Nanostructures in biodiagnostics. *Chem Rev* **2005,***105* (4), 1547-62.

3. Demidov, V. V.; Frank-Kamenetskii, M. D., Two sides of the coin: affinity and specificity of nucleic acid interactions. *Trends Biochem Sci* **2004,***29* (2), 62-71.

4. Samori, B.; Zuccheri, G., DNA codes for nanoscience. *Angew Chem Int Ed Engl* **2005,***44* (8), 1166-81.

5. Michael C. Pirrung, How to Make a DNA Chip. *Angewandte Chemie International Edition* **2002,***41* (8), 1276-1289.

6. Katz, E.; Willner, I., Integrated nanoparticle-biomolecule hybrid systems: synthesis, properties, and applications. *Angew Chem Int Ed Engl* **2004,***43* (45), 6042-108.

7. West, J. L.; Halas, N. J., Applications of nanotechnology to biotechnology commentary. *Curr Opin Biotechnol* **2000,***11* (2), 215-7.

8. Cho, Y.; Gorina, S.; Jeffrey, P. D.; Pavletich, N. P., Crystal structure of a p53 tumor suppressor-DNA complex: understanding tumorigenic mutations. *Science* **1994,***265* (5170), 346-55.

9. Karplus, M.; Kuriyan, J., Molecular dynamics and protein function. *Proc Natl Acad Sci U S A* **2005,***102* (19), 6679-85.

10. Phillips, J. C.; Braun, R.; Wang, W.; Gumbart, J.; Tajkhorshid, E.; Villa, E.; Chipot, C.; Skeel, R. D.; Kale, L.; Schulten, K., Scalable molecular dynamics with NAMD. *J Comput Chem* **2005,***26* (16), 1781-802.

11. Case, D. A.; Cheatham, T. E., 3rd; Darden, T.; Gohlke, H.; Luo, R.; Merz, K. M., Jr.; Onufriev, A.; Simmerling, C.; Wang, B.; Woods, R. J., The Amber biomolecular simulation programs. *J Comput Chem* **2005,***26* (16), 1668-88.

12. Cheatham, T. E.; Young, M. A., Molecular dynamics simulation of nucleic acids: successes, limitations, and promise. *Biopolymers* **2000,***56* (4), 232-56.

13. Humphrey, W.; Dalke, A.; Schulten, K., VMD: visual molecular dynamics. *J Mol Graph* **1996,***14* (1), 33-8, 27-8.

14. Tuckerman, M. E.; Martyna, G. J., Understanding Modern Molecular Dynamics: Techniques and Applications. *The Journal of Physical Chemistry B* **2001,***105* (31), 7598-7598.

15. Leger, J. F.; Robert, J.; Bourdieu, L.; Chatenay, D.; Marko, J. F., RecA binding to a single double-stranded DNA molecule: a possible role of DNA conformational fluctuations. *Proc Natl Acad Sci U S A* **1998,***95* (21), 12295-9.

16. Zhao, X.; Striolo, A.; Cummings, P. T., C_{60} binds to and deforms nucleotides. *Biophys J* **2005,***89* (6), 3856-62.

17. Tian, L.; Ram, K. B.; Ahmad, I.; Menon, L.; Holtz, M., Optical properties of a nanoporous array in silicon. *Journal of Applied Physics* **2005,***97* (2), -.

18. Hu, Y. S.; Guo, Y. G.; Sigle, W.; Hore, S.; Balaya, P.; Maier, J., Electrochemical lithiation synthesis of nanoporous materials with superior catalytic and capacitive activity. *Nat Mater* **2006,***5* (9), 713-7.

19. Hepel, M.; Kumarihamy, I.; Zhong, C. J., Nanoporous TiO2-supported bimetallic catalysts for methanol oxidation in acidic media. *Electrochemistry Communications* **2006,***8* (9), 1439-1444.

20. Nakane, J. J.; Akeson, M.; Marziali, A., Nanopore sensors for nucleic acid analysis. *Journal of Physics-Condensed Matter* **2003,***15* (32), R1365-R1393.

21. Baker, L. A.; Choi, Y. S.; Martin, C. R., Nanopore membranes for biomaterials synthesis, biosensing and bioseparations. *Current Nanoscience* **2006,***2* (3), 243-255.

22. Mor, G. K.; Shankar, K.; Paulose, M.; Varghese, O. K.; Grimes, C. A., Enhanced Photocleavage of Water Using Titania Nanotube Arrays. *Nano Letters* **2004,***5* (1), 191-195.

23. Paulose, M.; Varghese, O. K.; Mor, G. K.; Grimes, C. A.; Ong, K. G., Unprecedented ultra-high hydrogen gas sensitivity in undoped titania nanotubes. *Nanotechnology* **2006,***17* (2), 398-402.

24. Choi, J. S.; Wehrspohn, R. B.; Lee, J.; Gosele, U., Anodization of nanoimprinted titanium: a comparison with formation of porous alumina. *Electrochimica Acta* **2004,***49* (16), 2645-2652.

25. Pan, S. L.; Rothberg, L. J., Interferometric sensing of biomolecular binding using nanoporous aluminum oxide templates. *Nano Letters* **2003,***3* (6), 811-814.

26. Storm, A. J.; Storm, C.; Chen, J. H.; Zandbergen, H.; Joanny, J. F.; Dekker, C., Fast DNA translocation through a solid-state nanopore. *Nano Letters* **2005,***5* (7), 1193-1197.

27. Aksimentiev, A.; Schulten, K., Imaging alpha-hemolysin with molecular dynamics: Ionic conductance, osmotic permeability, and the electrostatic potential map. *Biophysical Journal* **2005,***88* (6), 3745-3761.

28. Heng, J. B.; Ho, C.; Kim, T.; Timp, R.; Aksimentiev, A.; Grinkova, Y. V.; Sligar, S.; Schulten, K.; Timp, G., Sizing DNA using a nanometer-diameter pore. *Biophysical Journal* **2004,***87* (4), 2905-2911.

29. Quan, X.; Yang, S. G.; Ruan, X. L.; Zhao, H. M., Preparation of titania nanotubes and their environmental applications as electrode. *Environmental Science & Technology* **2005,***39* (10), 3770-3775.

30. Gong, D.; Grimes, C. A.; Varghese, O. K.; Hu, W. C.; Singh, R. S.; Chen, Z.; Dickey, E. C., Titanium oxide nanotube arrays prepared by anodic oxidation. *Journal of Materials Research* **2001,***16* (12), 3331-3334.

31. Hamley, I. W., Nanotechnology with Soft Materials. *Angewandte Chemie International Edition* **2003,***42* (15), 1692-1712.

32. Wouters,D.; Schubert, U. S., Nanolithography and Nanochemistry: Probe-Related Patterning Techniques and Chemical Modification for Nanometer-Sized Devices. *Angewandte Chemie International Edition* **2004,***43* (19), 2480-2495.

33. Huang, S.; Tsutsui, G.; Sakaue, H.; Shingubara, S.; Takahagi, T., Formation of a large-scale Langmuir--Blodgett monolayer of alkanethiol-encapsulated gold particles. *Journal of Vacuum Science & Technology B: Microelectronics and Nanometer Structures* **2001,***19* (1), 115-120.

34. Shen, Y.-J.; Lee, Y.-L.; Yang, Y.-M., Monolayer Behavior and Langmuir−Blodgett Manipulation of CdS Quantum Dots. *The Journal of Physical Chemistry B* **2006,***110* (19), 9556-9564.

35. Colvin, V. L.; Goldstein, A. N.; Alivisatos, A. P., Semiconductor nanocrystals covalently bound to metal surfaces with self-assembled monolayers. *Journal of the American Chemical Society* **1992,***114* (13), 5221-5230.

36. Takahashi, M.; Natori, H.; Tajima, K.; Kobayashi, K., Particulate assemblies of CdS and TiO2 prepared by Langmuir-Blodgett technique with octadecylamine/methylstearate mixed films. *Thin Solid Films* **2005,***489* (1-2), 205-214.

37. Yang, Y.; Xiong, L.; Shi, J.; Nogami, M., Aligned Silver Nnanorod Arrays for Surface-Enhanced Raman Scattering*Nanotechnology***2006**17,2670-2674.

38. Diem, T.; Fabianowski, W.; Jaccodine, R.; Rodowski, R., Self-assembly formed oxime monolayers on a copper surface. *Thin Solid Films* **1995,***265* (1-2), 71-73.

39. Lee, Y.-L.; Lin, J.-Y.; Chang, C.-H., Thermodynamic characteristics and Langmuir-Blodgett deposition behavior of mixed DPPA/DPPC monolayers at air/liquid interfaces. *Journal of Colloid and Interface Science* **2006,***296* (2), 647-654.

40. Zhu, H.; Tao, C.; Zheng, S.; Li, J., One step synthesis and phase transition of phospholipid-modified Au particles into toluene. *Colloids and Surfaces A: Physicochemical and Engineering Aspects* **2005,***257-258*, 411-414.

41. Nieh, M.-P.; Raghunathan, V. A.; Glinka, C. J.; Harroun, T. A.; Pabst, G.; Katsaras, J., Magnetically Alignable Phase of Phospholipid &BicelleMixtures is a Chiral Nematic Made Up of Wormlike Micelles. *Langmuir* **2004,***20* (19), 7893-7897.

42. Ma, G.; Allen, H. C., Condensing Effect of Palmitic Acid on DPPC in Mixed Langmuir Monolayers. *Langmuir* **2007,***23* (2), 589-597.

43. Kaganer, V. M.; Möhwald, H.; Dutta, P., Structure and phase transitions in Langmuir monolayers. *Reviews of Modern Physics* **1999,***71* (3), 779-819.

44. Basu, J. K.; Sanyal, M. K., Ordering and growth of Langmuir-Blodgett films: X-ray scattering studies. *Physics Reports* **2002,***363* (1), 1-84.

45. Berne, B. J., Pecora, R**.**, *Dynamic Light Scattering : With Applications to Chemistry, Biology, and Physics,*Unabridged edition; Dover Publications2000.

46. Meyer, E. E.; Lin, Q.; Hassenkam, T.; Oroudjev, E.; Israelachvili, J. N., Origin of the long-range attraction between surfactant-coated surfaces. *Proceedings of the National Academy of Sciences of the United States of America* **2005,***102* (19), 6839-6842.

47. Elghanian, R.; Storhoff, J. J.; Mucic, R. C.; Letsinger, R. L.; Mirkin, C. A., Selective Colorimetric Detection of Polynucleotides Based on the Distance-Dependent Optical Properties of Gold Nanoparticles. *Science* **1997,***277* (5329), 1078-1081.

48. Beaucage, S. L., Strategies in the Preparation of DNA Oligonucleotide Arrays for Diagnostic Applications. *Current Medicinal Chemistry* **2001,***8*, 1213-1244.

49. Caswell, K. K.; Wilson, J. N.; Bunz, U. H. F.; Murphy, C. J., Preferential End-to-End Assembly of Gold Nanorods by Biotin−Streptavidin Connectors. *Journal of the American Chemical Society* **2003,***125* (46), 13914-13915.

50. Aslan, K.; Holley, P.; Davies, L.; Lakowicz, J. R.; Geddes, C. D., Angular-Ratiometric Plasmon-Resonance Based Light Scattering for Bioaffinity Sensing. *Journal of the American Chemical Society* **2005,***127* (34), 12115-12121.

51. Alivisatos, P., The use of nanocrystals in biological detection. *Nat Biotech* **2004,***22* (1), 47-52.

52. Taton, T. A.; Mirkin, C. A.; Letsinger, R. L., Scanometric DNA Array Detection with Nanoparticle Probes. *Science* **2000,***289* (5485), 1757-1760.

53. Xu, J.; Craig, S. L., Thermodynamics of DNA Hybridization on Gold Nanoparticles. *Journal of the American Chemical Society* **2005,***127* (38), 13227-13231.

54. Roll, D.; Malicka, J.; Gryczynski, I.; Gryczynski, Z.; Lakowicz, J. R., Metallic Colloid Wavelength-Ratiometric Scattering Sensors. *Analytical Chemistry* **2003,***75* (14), 3440-3445.

55. Qureshi, M. H.; Yeung, J. C.; Wu, S.-C.; Wong, S.-L., Development and Characterization of a Series of Soluble Tetrameric and Monomeric Streptavidin Muteins with Differential Biotin Binding Affinities. *J. Biol. Chem.* **2001,***276* (49), 46422-46428.

56. Holmberg,A.; Blomstergren,A. ; Nord,O.; Lukacs,M.; Lundeberg,J.; Uhlén,M., The biotin-streptavidin interaction can be reversibly broken using water at elevated temperatures. *Electrophoresis* **2005,***26* (3), 501-510.

57. Lytton-Jean, A. K. R.; Mirkin, C. A., A thermodynamic investigation into the binding properties of DNA functionalized gold nanoparticle probes and molecular fluorophore probes. *Journal of the American Chemical Society* **2005,***127* (37), 12754-12755.